12-1997

Reactive Quantum Scattering in Two Dimensions

Roy S. Calfas

DEPARTMENT OF THE AIR FORCE

AIR UNIVERSITY

AIR FORCE INSTITUTE OF TECHNOLOGY

Wright-Patterson Air Force Base, Ohio

AFIT/DSP/ENP/97-02

REACTIVE QUANTUM SCATTERING IN TWO DIMENSIONS

DISSERTATION

Roy S. Calfas
Captain, USAF

AFIT/DSP/ENP/97-02

The views expressed in this dissertation are those of the author and do not reflect the official policy or position of the Department of Defense or the U. S. Government.

AFIT/DSP/ENP/97-02

REACTIVE QUANTUM SCATTERING IN TWO DIMENSIONS

DISSERTATION

Presented to the Faculty of the Graduate School of Engineering
of the Air Force Institute of Technology
Air University
In Partial Fulfillment of the
Requirements for the Degree of
Doctor of Philosophy

Roy S. Calfas, B.S., M.S.
Captain, USAF

January 1997

AFIT/DS/ENP/97-02

Reactive Quantum Scattering in Two Dimensions

Roy S. Calfas, B.S., M.S.
Captain, USAF

Approved:

[redacted]
Dr. David E. Weeks, Chairman — 1 Dec 97 Date

[redacted]
Dr. William F. Bailey, Committee Member — 1 Dec 97 Date

[redacted]
Dr. Kirk A. Mathews, Committee Member — 1 Dec 1997 Date

[redacted]
Lt. Col. David J. Couliette, Committee Member — 1 Dec 97 Date

[redacted]
Dr. Jerry A. Boatz, Committee Member — 16 Jan 97 Date

[redacted]
Dr. Peter S. Maybeck, Dean's Representative — 1 Dec 1997 Date

Accepted:

[redacted]
Robert A. Calico, Jr.
Dean, Graduate School of Engineering

Preface

Current numeric calculations of state-to-state resolved quantum reactive scattering matrix elements are computationally limited to systems of three degrees of freedom or less. The large grids or a large number of grids used in the computation are inefficient. In an effort to improve the computation times in two– dimensional calculations, the combination of the channel packet method together with absorbing boundary conditions is explored for the collinear $H + H_2$ reaction and a simple model of two collinear coupled Morse oscillators. For collinear $H + H_2$, results are obtained which are in good agreement with previous calculations while simultaneously providing a reduction in computation time. For the simple model of two coupled collinear Morse oscillators, scattering matrix elements for some mass configurations contain non-trivial errors introduced by absorbing boundary condition reflection. For these mass configurations, the effects of absorbing boundary condition reflection are explored and scattering matrix elements are presented for absorbing boundary condition reflection for a simplified Morse potential. Good scattering matrix elements are presented for the light-heavy-light mass configuration of the two coupled collinear Morse oscillators. The effects of kinetic coupling and potential well depth on scattering matrix elements are also presented for this mass configuration.

A project like this is not done without the assistance and encouragement of many others. I'd like to thank my advisor, Dr. David E. Weeks, for his tireless encouragement and assistance during my stay. Dr. Weeks certainly deserves saint-hood for tolerating my many questions and frustrations with the lack of adequate computer support. I'd also like to thank Dr. Kirk Mathews for his many insightful questions and providing me with a Sun SPARC2 workstation in an effort to alleviate the lack of adequate computer support. Thanks to Dr. William Bailey, Lt Col David Coulliette and Dr. Jerry Boatz for their many insightful questions, comments and encouragement.

This project would certainly not have met success without the support and encouragement of my friends. Thanks to Capt. Rob Johnson and Ms. Bethany Kolb for hosting me on my many visits to Albuquerque, NM. Likewise, thanks to Capt. and Mrs. Greg Williams for visits, support and encouragement. Thanks to Maj. Greg Vansuch and family for the many good lunches, dinners and conversation. I'd be at a loss with out Maj. Jack McCrae and Capt. Kim McCrae. Thanks for the satellite dish, and the many hours spent getting Babylon 5 a week ahead of time, the superb beers we brewed and all the many adventures. A very special thanks to Capt. and Mrs. Rob Franklin without whom I'd be missing the major part of my life, my horse HPS Bad Boy and my cat Robert.

There's also a great number of people outside AFIT without whom I'd probably gone crazy. Thanks to Bill and Lora Rumsey whom I've known all my life. Without you, I wouldn't be alive to do this. Thanks to Drs. Deb Bickford and Peter Ward and their children Nick and Suzie for all the meals and just general good times. For everything, many thanks go to Ms. Gera Dingemans. A very big thank you to BA in Columbus, live long and prosper! Finally, but not least, to that special Texan, there are no words.

Many students have close family that help them through an endeavor like this. I have two very special creatures in mine. Thanks to my horse Q, aka HPS Bad Boy, and my cat Robert for constantly reminding me what is important in this life.

This Dissertation is dedicated in part to my aunt, Mrs. [redacted], who passed away during the writing. I'll miss you.

This document was typeset using the LaTeX document preparation system. The system used was emTeXgi for the Windows family of GUIs.

Roy S. Calfas

Table of Contents

List of Figures

List of Tables

Abstract

In an effort to develop a more efficient time dependent approach for calculating scattering matrix elements, absorbing boundary conditions are combined together with the channel packet method. The channel packet method relies on calculating two Møller states: one representing reactants and one representing products. The time dependent correlation function between the two Møller states is efficiently computed by individually propagating the Møller states using absorbing boundary conditions as they exit the interaction region of the potential. As a Møller state evolves in time, it will be attenuated by the absorbing boundary conditions without reflecting off the edge of the grid thereby permitting the use of a much smaller grid. The Fourier transform of the correlation function is then used to compute scattering matrix elements.

The efficiency of the combination of the channel packet method with absorbing boundary conditions is demonstrated in one dimension through application to the one dimensional square well. The one dimensional square well has an analytic solution which provides a benchmark for testing both the efficiency and accuracy of this approach. Scattering matrix elements obtained using the channel packet method with absorbing boundary conditions are in excellent agreement with the analytic solution. The new approach converges to the correct, analytic solution as well as provides a dramatic reduction in grid size. The reduced grid size results in a faster, more efficient computation. The effects of absorbing boundary conditions in one dimension are investigated using a one dimensional potential consisting of a Gaussian well with symmetric Gaussian barriers.

Similar to the one dimensional square well, the collinear $H + H_2$ reaction provides a benchmark for testing the efficiency and convergence of the channel packet method with absorbing boundary conditions as applied to scattering matrix elements

in two dimensional scattering. Again, the new method is more efficient than previous methods while converging on the accepted solution. The combination of the channel packet method with absorbing boundary conditions results in an order of magnitude savings in the time necessary to compute the correlation function.

With the channel packet method with absorbing boundary conditions established as an efficient, accurate method for computing quantum reactive scattering matrix elements, a model system consisting of two coupled collinear Morse oscillators is used to investigate the effects of kinetic energy coupling and potential well depth on scattering. However, for light-light-light, medium-light-medium and heavy-light-heavy mass configurations, absorbing boundary condition reflection introduces significant error into the scattering matrix elements. In an effort to understand the errors introduced by absorbing boundary condition reflection, scattering matrix elements are presented for reflection from absorbing boundary conditions using a simplified Morse oscillator potential. Unlike the previous three mass configurations, scattering matrix elements for the light-heavy-light mass configuration do not suffer from significant absorbing boundary condition reflection error. For this mass configuration, the effects of kinetic energy coupling and well depth on scattering matrix elements are presented for a variety of two collinear coupled Morse oscillator potentials.

REACTIVE QUANTUM SCATTERING IN TWO DIMENSIONS

I. Introduction

Molecular reaction dynamics plays a central role in many research efforts of interest to the United States Air Force. For example, the High Energy Density Materials[1,2] project at Edwards AFB, CA seeks to identify new rocket fuels that will improve the current spacelift capabilities of the Air Force. This effort is supported and guided by a variety of computational models that primarily focus on determining the molecular structure and energies of high energy density material candidates. Both classical and quantum mechanical models of the dynamical properties will play an essential role in determining the suitability of a new high energy density material for use as a rocket fuel. Another research effort of interest to the Air Force is the development of more powerful and compact chemical lasers at the Air Force Institute of Technology and Phillips Lab, Kirtland AFB, NM.[3,4] Chemical lasers will be useful in a variety of Air Force applications including the Airborne Laser project and the Infrared Countermeasures project.[5–7] The continued development of chemical lasers will benefit from a more detailed view of the collisional transfer of energy afforded by molecular dynamics simulations. In addition, several Air Force research projects at the Geophysics Directorate, Phillips Lab, Hanscom AFB, MA are investigating the dynamics of upper atmosphere pollution.[8–10] The research into upper atmosphere pollution is concerned with both the sources of pollution as well as the many chemical reactions between pollutants and the natural constituents of the upper atmosphere. For example, what is the impact of high altitude flights by supersonic aircraft, military or commercial, on the ozone layer? The answer to this question and many others will benefit from the ability to efficiently model reaction dynamics involved in upper atmosphere pollution.

The quantum dynamics of a molecular reaction can be understood through the calculation of quantum scattering matrix (S–matrix) elements. The absolute value squared of an S–matrix element is the state-to-state resolved probability of reaction. Current methods for computing S–matrix elements are limited to very simple reactions where the number of dimensions is two or three. The research presented here is part of an effort to develop computational methods which are more efficient than current methods and thereby extend the range of reactions for which S–matrix elements may be calculated.

1.1 Background

It is only in the last two decades that time dependent methods have become practical for computing S–matrix elements. Historically, the first practical methods for computing S–matrix elements were analytical solutions to very simple problems. In 1929, London first presented his method for analytically modeling potential energy surfaces.[11] London's method only took into account three, collinear theoretical atoms A, B and C and yields an analytic solution for the S–matrix elements. In 1931, Eyring and Polanyi extended London's methods to produce an analytical surface and S–matrix elements for the two dimensional, collinear $H + H_2$ reaction.[12] The LEP surface, as it was named, correctly matched several features of the true surface; though, the surface incorrectly predicts a potential well for the intersection of $H_2 + H$ and $H + H_2$. It wasn't until 1955 when Sato[13] corrected the LEP surface (to the LEPS surface) to show a barrier in the interaction region of $H + H_2 \rightarrow H_2 + H$. The analytical methods of London, Eyring, Polanyi and Sato remained state of the art for computing S–matrix elements well into the 1970s.

In the 1950's, new methods that relied on the numeric solution of time independent classical and quasi-classical equations became possible with the advent of the digital computer.[14–20] The disadvantage to these methods is that they rely upon the diagonalization of large matrices whose elements are the coefficients of the

equations of motion of the reacting particles. The disadvantages of large grids and matrices with the high financial cost of computer time continued to limit their use to simple one and two dimensional problems. In the early 1980s faster, less expensive computers became available and quantum S–matrix calculations became computationally feasible.[21-36] However, these calculations are limited in scope to either two dimensional geometries for a variety of reactions or three-dimensional calculations for very simple reactions like $D + H_2 \rightarrow DH + H$. While some quantum methods allow the computation of a single state-to-state[a] resolved S–matrix element, the computational overhead associated with the large grids necessary to perform these calculations remains the limiting factor. A reduction in grid size while maintaining the accuracy of the result will lead to faster computations and the ability to compute S–matrix elements for a wider variety of reactions.

1.2 Problem and scope

The goal of this research is to develop the combination of the time dependent channel packet method (usually referred to as the channel packet method)[25,37,38] with absorbing boundary conditions[39,40] as a valid, accurate and efficient approach to calculating quantum scattering matrix elements in one and two dimensions. The new method will be tested for validity through the application of several convergence tests. The first tests convergence towards the correct solution. A method which converges to a wrong answer has no use. In one dimension, the square well potential has an analytic solution a provides an excellent test for convergence to the correct solution. In two dimensions, the collinear $H + H_2$ reaction is well established[17,25,31-35,39] as a benchmark for computational quantum chemistry and will be used to test the new method for convergence towards the correct solution. The test for convergence to the correct solution also demonstrates the accuracy of the new method. The second test for convergence is concerned with efficiency, or order. A

[a] Where the states involved are limited to those described in the Hamiltonian.

method can be valid while also being cumbersome and computationally expensive. The application of the channel packet method with absorbing boundary conditions will be tested for efficient convergence for the square well potential in one dimension and the collinear $H + H_2$ potential in two dimensions. The efficiency of the new method, gained by reducing the size of the grids used in the computation, can be judged by the time a computation using the channel packet method takes with and without absorbing boundary conditions. Finally, the influence of absorbing boundary conditions on the computational results will be investigated using a Gaussian potential in one dimension and two coupled Morse oscillators in two dimensions.

The computer resources used for this study include the MIPS-R3000-based Silicon Graphics workstations at the Air Force Institute of Technology, the MIPS-R10000-based Silicon Graphics Power Challenge Array at the Major Shared Resource Center at Wright–Patterson AFB and the MIPS-R5000-based Silicon Graphics workstations at the Air Force Research Lab, Hanscom AFB. The FORTRAN77 computer language was used for all code development.

1.3 Outline

Chapter II provides a basic overview of quantum reactive scattering, absorbing boundary conditions, the channel packet method and the underlying use of Møller operators, and the numeric implementation of the channel packet method with absorbing boundary conditions. Chapter III presents the results of scattering in one dimension for a square well potential and a Gaussian barrier-well-barrier potential. Chapter IV researches the application of the combination of the channel packet method with absorbing boundary conditions to two dimensional quantum scattering by computing S–matrix elements for the collinear $H + H_2$ reaction.[41] The problem of reflection from problems of absorbing boundary conditions is researched in Chapter V for a model two dimensional system of two coupled Morse oscillators. Absorbing boundary condition reflection introduces error into the S–

matrix elements for certain mass configurations. As an initial analysis of reflection from absorbing boundary conditions, S–matrix elements are presented for reflection from absorbing boundary conditions for the light-light-light, medium-light-medium and heavy-light-heavy mass configurations. Chapter VI presents S–matrix elements using the model two dimensional system of two coupled Morse oscillators for a light-heavy-light mass configuration. S–matrix elements for this mass configuration do not exhibit errors attributed to reflection from absorbing boundary conditions. An analysis of the effect of the depth of the well in the interaction region is presented for the light-heavy-light mass configuration as well as the effects of kinetically decoupling the two Morse oscillators. Conclusions and recommendations are contained in Chapter VII. Appendix A contains the derivation of the channel packet method formulation of S–matrix elements for two dimensional scattering. Appendix B gives the derivation of the momentum transformation between Jacobi and bond representations. Appendix C briefly overviews the one dimensional and two dimensional codes implementing the channel packet method with absorbing boundary conditions. Appendix D contains the complete set of graphs for the research presented in Chapter VI.

1.4 Conventions and units

Throughout this document, the term *channel* is used to denote a given arrangement of atoms, for example, $A + BC$ and $AC + B$. The term channel is synonymous with arrangement and arrangement channel. Within a given channel, the fragments involved in reactive scattering may have internal degrees of freedom. In quantum mechanics, these internal degrees of freedom are described by eigenstates and associated quantum numbers. The term *subchannel* is used to denote the combination of a channel with a particular set of eigenstates of the internal degrees of freedom in that channel.

The units used in the actual computations are *atomic units* denoted by *au*. Table 1.1 contains conversions between au and other commonly used units.

Table 1.1 Atomic units

unit	1 au equals
mass	9.11×10^{-31} kg
angular momentum ($\hbar$)	1.05×10^{-34} J·sec
length	5.29×10^{-11} m
time	2.42×10^{-17} sec
energy	27.21 eV

II. Quantum scattering theory

The central goal of quantum scattering theory is to determine the probability of reaction. In this chapter, the theories of coordinate systems, Hamiltonians and asymptotic limits, absorbing boundary conditions, and the channel packet method and the application of Møller Operators are developed.

2.1 Background

Quantum scattering begins with the time dependent Schrödinger equation,

$$i\hbar\frac{d}{dt}|\Psi(t)\rangle = \hat{H}|\Psi(t)\rangle, \tag{2.1}$$

where $\hat{H}$ is the Hamiltonian and the state of the system is given by $|\Psi(t)\rangle$. For time independent Hamiltonians, the formal solution to Equation 2.1 is

$$|\Psi(t)\rangle = \hat{U}(t)\,|\Psi(t=0)\rangle = \exp\left(-i\frac{\hat{H}t}{\hbar}\right)|\Psi(t=0)\rangle, \tag{2.2}$$

where $\hat{U}(t)$ is the time evolution operator. The Hamiltonian $\hat{H}$ is usually defined as the sum of two operators,

$$\hat{H} = \hat{T} + \hat{V}, \tag{2.3}$$

where $\hat{T}$ is the kinetic energy operator and $\hat{V}$ is the potential energy operator. For a wide variety of reactions, $\hat{T}$ is the same and the dynamics are governed primarily by $\hat{V}$.

2.2 Coordinate systems

Equation 2.1 must be expressed in some representation in order to be solved and two coordinate systems used to provide a representation are of interest: Bond coordinates and Jacobi coordinates.[42] In Section 2.3, we will explore the need for two

coordinate systems as they relate to the Hamiltonian and asymptotic limits. Bond coordinates, illustrated in Figure 2.1, treat each channel on an equivalent basis. Two sets of Jacobi coordinates, (r_α, R_α) and (r_β, R_β), illustrated in Figure 2.2, are used to provide a separable representation of $\hat{H}$ in the asymptotic limit in each of the two possible channels $A + BC$ and $AB + C$.

In the $A + BC$ channel, the transformation between Jacobi coordinates and bond coordinates in two dimensions is given by

$$\begin{pmatrix} r_\alpha \\ R_\alpha \end{pmatrix} = \begin{pmatrix} 1 & \frac{m_c}{m_b+m_c} \\ 0 & 1 \end{pmatrix} \begin{pmatrix} X \\ Y \end{pmatrix}, \tag{2.4}$$

where m_j is the mass of the atom j. From Equation 2.4, Figure 2.1 and Figure 2.2, it is clear that the Jacobi coordinate R_α is equal to the bond coordinate Y and r_α is equal to the sum of X and distance from atom B to the center-of-mass of the BC diatom.

2.3 Hamiltonians and asymptotic limits

The issue of which coordinate system to use is closely linked to the issue of asymptotic limits. In quantum scattering, we must assume that at some point in space the fragments, either products or reactants, are widely separated such that the interaction potential between them is zero. Under this assumption, the Hamiltonian is written as

$$\hat{H} = \hat{H}_0 + \hat{V}, \tag{2.5}$$

where $\hat{H}$ is the full scattering Hamiltonian, $\hat{H}_0$ is the asymptotic Hamiltonian and $\hat{V}$ is the interaction potential that vanishes in the asymptotic limit,

$$\lim_{r_\gamma \to \infty} \hat{V} = 0, \quad \gamma = \alpha, \beta, \tag{2.6}$$

where $\gamma = \alpha, \beta$ labels the channel.

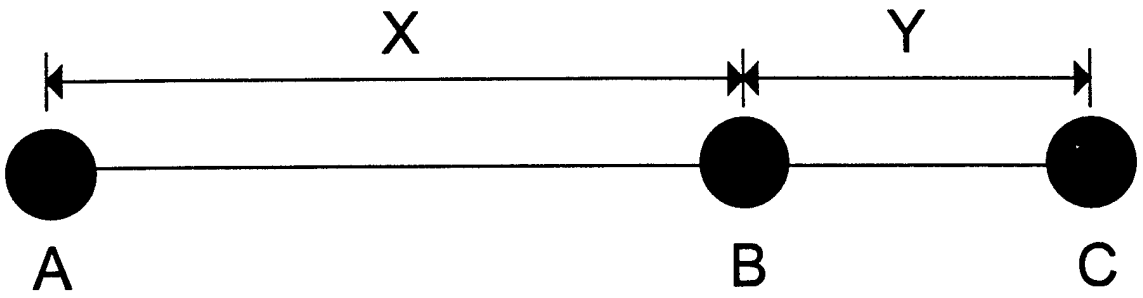

Figure 2.1 Bond coordinates.

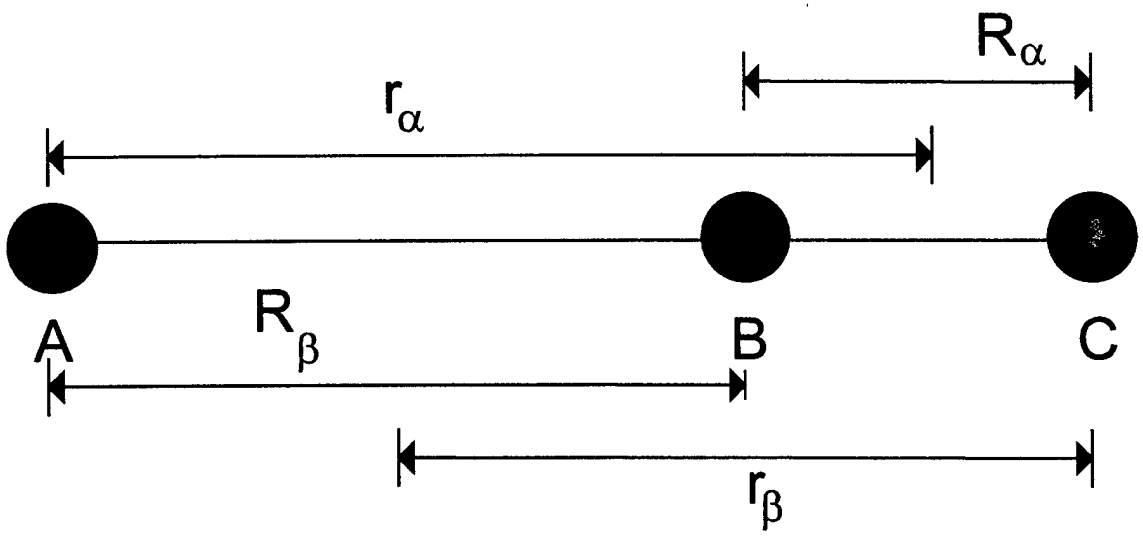

Figure 2.2 Jacobi coordinates.

Using Jacobi coordinates, the asymptotic Hamiltonian can be separated into parts according to

$$\hat{H}_0 = \hat{H}_{rel} + \hat{H}_{int}, \tag{2.7}$$

where $\hat{H}_{rel}$ is Hamiltonian governing the relative motion between reactants or products and $\hat{H}_{int}$ is the Hamiltonian governing the internal dynamics of reactants or products. It is important to note that Jacobi coordinates suitable for one channel will not separate $\hat{H}_0$ in another channel. An appropriate choice of Jacobi coordinates is used to construct the initial reactant and product wave packet in each channel. Jacobi coordinates are used since the Hamiltonian is separable in Jacobi coordinates as shown in Equation 2.7. The wave packets are then transformed to bond coordinates to facilitate the computation of a correlation function used to calculate S–matrix elements.

2.4 Absorbing boundary conditions

One problem with time dependent methods is reflection of the wave function at the edges of the grid used in numerical calculations. These reflections can lead to spurious results and are usually handled by choosing a grid large enough that, by the time the wave function reaches the edge, it has completely left the interaction region and the computation may be terminated. The increased grid size translates into increased computational overhead. Absorbing boundary conditions have been used previously in a variety of calculations[14–17,21,22,36,39,40,43–51] to prevent evolving wave packets from reflecting from the edge of the grid before the computation has finished. It should be noted, however, that reflection can only be minimized and not eliminated. In the channel packet method, it is in the calculation of the correlation function that the application of absorbing boundary conditions proves useful. This application is discussed in Section 2.6.2.

Negative, imaginary potentials are well known as the only absorbing potentials. These potentials, whose mathematical form is arbitrary, absorb by exponentially

attenuating the wave function as it evolves in time. In the application of absorbing boundary conditions to the channel packet method performed for this study, a simple exponential of the form

$$V_a = \pm A i \exp\left\{\frac{(x - x_0)^2}{B}\right\}, \tag{2.8}$$

was selected where A and B were chosen to minimize reflection. This form for the absorbing boundary condition was chosen because it is a smooth function which can reach a large, positive value in a relatively short distance. These two characteristics permit the use of the smallest grid possible with a subsequent improvement in computational efficiency.

2.5 Channel packet method

The time dependent channel packet method, referred to as the channel packet method, was developed by Weeks and Tannor[25,37,38] and is based on the use of Møller operators.[52] In this section, Møller operators are discussed and then applied in the derivation of the channel packet method.

2.5.1 Møller operators. The development of Møller operators begins with the Hamiltonian and asymptotic limits discussed in Section 2.3. Utilizing these ideas, the Hamiltonian can be written as

$$\hat{H} = \hat{H}_0^\gamma + \hat{V}^\gamma \tag{2.9}$$

where $\hat{H}$ is the full Hamiltonian, $\hat{H}_0^\gamma$ is the asymptotic Hamiltonian in channel γ and $\hat{V}^\gamma$ is the interaction potential that vanishes in the asymptotic limit. The label γ now includes the channel label as well as the labels of the internal eigenstates, thereby labeling both the channel and subchannel.

Møller operators are defined by

$$\hat{\Omega}_{\pm}^{\gamma} = \lim_{t \to \mp\infty} \exp\left(i\frac{\hat{H}t}{\hbar}\right) \exp\left(-i\frac{\hat{H}_0^{\gamma}t}{\hbar}\right), \tag{2.10}$$

where $\hat{U}(t) = \exp\left(-i\frac{\hat{H}t}{\hbar}\right)$ is the time evolution operator. Møller operators are isometric

$$\hat{\Omega}_{\pm}^{\dagger}\hat{\Omega}_{\pm} = 1, \tag{2.11}$$

and if bound states are not present, they are unitary[52]

$$\hat{\Omega}_{\pm}^{\dagger} = \hat{\Omega}_{\pm}^{-1}. \tag{2.12}$$

The result of propagating a state under a Møller operator is denoted by

$$\hat{\Omega}_{\pm}|\Psi_{in(out)}\rangle = |\Psi\pm\rangle, \tag{2.13}$$

where $|\Psi\pm\rangle$ is referred to as a Møller state. The effect of the Møller operator $\hat{\Omega}_{\pm}$ is to propagate the state $|\Psi\rangle$ backward (forward) to time $t = -\infty$ ($t = +\infty$) under the influence of $\hat{H}_0$, then propagate the result forward (backward) to time $t = 0$ under the influence of $\hat{H}$. By definition, the Møller operator $\hat{\Omega}_-$ operates only on asymptotic product states $|\Psi_{out}\rangle$ and the Møller operator $\hat{\Omega}_+$ operates only on asymptotic reactant states $|\Psi_{in}\rangle$. Møller operators are used to define the scattering operator through

$$\hat{S} = \hat{\Omega}_{-}^{\dagger}\hat{\Omega}_{+}, \tag{2.14}$$

where the probability of scattering from an initial state $|\Psi_{in}\rangle$ to a final state $|\Psi_{out}\rangle$ is given by

$$P = |\langle\Psi_{out}|\hat{S}|\Psi_{in}\rangle|^2 = |\langle\Psi_{out}|\hat{\Omega}_{-}^{\dagger}\hat{\Omega}_{+}|\Psi_{in}\rangle|^2 = |\langle\Psi-|\Psi+\rangle|^2. \tag{2.15}$$

Equation 2.15 yields S-matrix elements in the $\langle\Psi_{in}|\Psi_{out}\rangle$ representation. While this is an acceptable result, it is more useful to express S-matrix elements in the energy or momentum representation. In the channel packet method, expressing S-matrix elements in the momentum representation leads to the calculation of a time dependent correlation function.

2.5.2 The channel packet method. The core of the channel packet method is the use of two wave packets to compute state-to-state S-matrix elements. One wave packet represents the asymptotic reactant subchannel, labeled γ, and the second wave packet represents the asymptotic product subchannel, labeled γ'. The choice of the two subchannels, reactant and product, determines which S-matrix elements are calculated. The technique is to propagate each wave packet using the appropriate Møller operator.

The γ subchannel asymptotic Hilbert space is spanned by the direct product of eigenstates of the relative Hamiltonian, $\hat{H}^{\gamma}_{rel}$, represented by the ket $|k_\gamma\rangle$, and eigenstates of the internal Hamiltonian, $\hat{H}^{\gamma}_{int}$, represented by the ket $|\gamma\rangle$. The basis vectors spanning the Hilbert space are given by,

$$|k_\gamma, \gamma\rangle. \tag{2.16}$$

These basis vectors are eigenstates of the asymptotic Hamiltonian with eigenvalues given by

$$\hat{H}^{\gamma}_0|k_\gamma,\gamma\rangle = \left(\hat{H}^{\gamma}_{rel} + \hat{H}^{\gamma}_{int}\right)|k_\gamma,\gamma\rangle = \left(\frac{\hbar^2}{2\mu_\gamma}k^2_\gamma + E_\gamma\right)|k_\gamma,\gamma\rangle = E|k_\gamma,\gamma\rangle, \tag{2.17}$$

where $\hbar^2 k^2_\gamma/2\mu_\gamma$ is the relative kinetic energy, μ_γ is the reduced mass of the system, E_γ is the energy associated with the internal eigenstate and E is the total energy. A new set of states is generated by operating on the basis $|k_\gamma,\gamma\rangle$ with the Møller

operators

$$|k_\gamma, \gamma\pm\rangle = \hat{\Omega}^\gamma_\pm |k_\gamma, \gamma\rangle, \tag{2.18}$$

where the $\pm$ in $|k_\gamma, \gamma\pm\rangle$ labels both the state $|k_\gamma\rangle$ and the state $|\gamma\rangle$.

It is easy to show that the $|k_\gamma, \gamma\pm\rangle$ are eigenstates of the full Hamiltonian. Using the intertwining relationship,[52]

$$\hat{H}\hat{\Omega}_\pm = \hat{\Omega}_\pm \hat{H}_0, \tag{2.19}$$

and from Equations 2.17 and 2.18, it follows that

$$\begin{aligned}
\hat{H}|k_\gamma,\gamma\pm\rangle &= \hat{H}\hat{\Omega}^\gamma_\pm |k_\gamma, \gamma\rangle \\
&= \hat{\Omega}^\gamma_\pm \hat{H}^\gamma_0 |k_\gamma, \gamma\rangle \\
&= \hat{\Omega}^\gamma_\pm \left(\frac{\hbar^2}{2\mu_\gamma} k_\gamma^2 + E_\gamma\right) |k_\gamma, \gamma\rangle \\
&= \left(\frac{\hbar^2}{2\mu_\gamma} k_\gamma^2 + E_\gamma\right) \hat{\Omega}^\gamma_\pm |k_\gamma, \gamma\rangle \\
&= \left(\frac{\hbar^2}{2\mu_\gamma} k_\gamma^2 + E_\gamma\right) |k_\gamma, \gamma\pm\rangle,
\end{aligned} \tag{2.20}$$

where the eigenvalues of $\hat{H}$ are the same as the eigenvalues of $\hat{H}^\gamma_0$.

Consider the initial state $|\Psi^\gamma_{in(out)}\rangle$ constructed as a product of a linear combination of kets $|k_\gamma\rangle$ with an eigenstate $|\gamma\rangle$,

$$|\Psi^\gamma_{in(out)}\rangle = \int_{-\infty}^{+\infty} dk_\gamma \eta_\pm(k_\gamma) |k_\gamma, \gamma\rangle. \tag{2.21}$$

The corresponding Møller states $|\Psi^\gamma_\pm\rangle$ are given by

$$|\Psi^\gamma_\pm\rangle = \Omega^\gamma_\pm |\Psi^\gamma_{in(out)}\rangle = \int_{-\infty}^{+\infty} dk_\gamma \eta_\pm(k_\gamma) |k_\gamma, \gamma\pm\rangle. \tag{2.22}$$

From Equations 2.21 and 2.22 it is clear that the expansion coefficients, $\eta_{\pm}(k_\gamma)$, used to expand the initial wave function in terms of the eigenstates of $\hat{H}_0^\gamma$ are the same coefficients used to expand the Møller states in terms of the eigenstates of $\hat{H}$. Thus, the eigenstates of the full Hamiltonian can be used to expand the Møller states, $|\Psi_{\pm}^{\gamma}\rangle$.

The isometric subchannel Møller operators, $\hat{\Omega}_{\pm}^{\gamma}$, acting on the basis vectors $|k_\gamma, \gamma\rangle$, which span the asymptotic Hilbert space, generate two sets of basis vectors $|k_\gamma, \gamma\pm\rangle$, which are eigenvectors of the full scattering Hamiltonian H. The two complete sets satisfy the orthogonality relations,[52]

$$\begin{aligned} \langle k'_{\gamma'}, \gamma' \pm | k_\gamma, \gamma \pm \rangle &= \langle k'_{\gamma'}, \gamma' \pm | \hat{\Omega}_{\pm}^{\gamma'\dagger} \hat{\Omega}_{\pm}^{\gamma} | k_\gamma, \gamma \rangle \\ &= \langle k'_{\gamma'}, \gamma' | k_\gamma, \gamma \rangle \\ &= \delta_{\gamma'\gamma} \delta\left(k'_{\gamma'} - k_\gamma\right), \end{aligned} \tag{2.23}$$

and

$$\begin{aligned} \langle k'_{\gamma'}, \gamma' - | k_\gamma, \gamma + \rangle &= \langle k'_{\gamma'}, \gamma' | \hat{\Omega}_{-}^{\gamma'\dagger} \hat{\Omega}_{+}^{\gamma} | k_\gamma, \gamma \rangle \\ &= \langle k'_{\gamma'}, \gamma' | \hat{S} | k_\gamma, \gamma \rangle \\ &= \frac{\hbar \sqrt{|k'_{\gamma'}||k_\gamma|}}{\sqrt{\mu_{\gamma'}\mu_\gamma}} \delta(E' - E) S_{k'_{\gamma'} k_\gamma}^{\gamma'\gamma}, \end{aligned} \tag{2.24}$$

where $\frac{\hbar^2}{\mu_\gamma}|k_\gamma| = \frac{\partial E}{\partial |k_\gamma|}$ is the density of states and $S_{k'_{\gamma'} k_\gamma}^{\gamma'\gamma}$ is the on–shell S–matrix element giving the probability amplitude of scattering from subchannel γ with relative momentum k_γ to subchannel γ' with relative momentum $k'_{\gamma'}$.

Equation 2.24 shows that all that is necessary to obtain S–matrix elements in the momentum representation is the evaluation of the scalar product $\langle k_{\gamma'}, \gamma' - | k_\gamma, \gamma + \rangle$. In the channel packet method this is done by first considering the Fourier transform

of the time evolution of the Møller state $|\Psi_+^{\gamma'}\rangle$,

$$|A_+^{\gamma}(E)\rangle = \int_{-\infty}^{+\infty} dt \exp\left(\frac{iEt}{\hbar}\right) \exp\left(\frac{-i\hat{H}t}{\hbar}\right) |\Psi_+^{\gamma}\rangle. \tag{2.25}$$

Substituting the expansion of $|\Psi_+^{\gamma}\rangle$ in terms of $|k_\gamma, \gamma\rangle$, given in Equation 2.22, into Equation 2.25, it is easy to show that $|A_+^{\gamma}(E)\rangle$ is an unnormalized eigenvector, shown in Appendix A, of the full scattering Hamiltonian given by

$$|A_+^{\gamma}(E)\rangle = \frac{2\pi\mu_\gamma}{\hbar|k_\gamma|}[\eta_+(+k_\gamma)\,|+k_\gamma, \gamma+\rangle + \eta_-(-k_\gamma)\,|-k_\gamma, \gamma+\rangle]. \tag{2.26}$$

The prefix + or − on k_γ in Equation 2.26 explicitly labels the degenerate eigenstates of the full scattering Hamiltonian. The degenerate eigenstates are explicitly labeled by the ± prefix as having positive momentum (+) or negative momentum (−). S-matrix elements result from the evaluation of the scalar product $\langle\Psi_-^{\gamma'}|A_+^{\gamma}(E)\rangle$, where Equation 2.22 is used to expand $|\Psi_-^{\gamma'}\rangle$ in terms of $|k'_{\gamma'}, \gamma'-\rangle$.

$$\begin{aligned}\langle\Psi_-^{\gamma'}|A_+^{\gamma}(E)\rangle &= \frac{2\pi\mu_\gamma}{\hbar|k_\gamma|}\int_{-\infty}^{+\infty} dk'_{\gamma'}[\eta_-^*\left(k'_{\gamma'}\right)\eta_+(+k_\gamma)\,\langle k'_{\gamma'}, \gamma'-|+k_\gamma, \gamma+\rangle \\ &\quad +\eta_-^*\left(k'_{\gamma'}\right)\eta_+(-k_\gamma)\,\langle k'_{\gamma'}, \gamma'-|-k_\gamma, \gamma+\rangle].\end{aligned} \tag{2.27}$$

The orthogonality relation given in Equation 2.24 reduces the integral in Equation 2.27 to

$$\begin{aligned}\langle\Psi_-^{\gamma'}|A_+^{\gamma}(E)\rangle &= \frac{2\pi\sqrt{\mu_\gamma\mu_{\gamma'}}}{\hbar\sqrt{|k'_{\gamma'}||k_\gamma|}}\,[\,\eta_-^*\left(+k'_{\gamma'}\right)\eta_+(+k_\gamma)\,S^{\gamma'\gamma}_{+k'_{\gamma'}+k_\gamma} \\ &\quad +\eta_-^*\left(+k'_{\gamma'}\right)\eta_+(-k_\gamma)\,S^{\gamma'\gamma}_{+k'_{\gamma'}-k_\gamma} \\ &\quad +\eta_-^*\left(-k'_{\gamma'}\right)\eta_+(+k_\gamma)\,S^{\gamma'\gamma}_{-k'_{\gamma'}+k_\gamma} \\ &\quad +\eta_-^*\left(-k'_{\gamma'}\right)\eta_+(-k_\gamma)\,S^{\gamma'\gamma}_{-k'_{\gamma'}-k_\gamma}].\end{aligned} \tag{2.28}$$

We are free to simplify Equation 2.28 since the only requirement that the asymptotic states $|\Psi^{\gamma}_{in(out)}\rangle$ must satisfy in order to obtain Equation 2.28 is that they are elements

of the γ^{th} subchannel Hilbert space. The simplification is to choose the expansion coefficients $\eta_{\pm}(k_\gamma)$ such that they include only one degenerate state for each value of the relative kinetic energy in the γ subchannel. Choosing $\eta_{+}(k_\gamma) = 0$ for $k_\gamma \geq 0$ and $\eta_{-}\left(k'_\gamma\right) = 0$ for $k'_\gamma \leq 0$, the evaluation of Equation 2.28 reduces to

$$\langle \Psi_{-}^{\gamma'} | A_{+}^{\gamma}(E) \rangle = \frac{2\pi\sqrt{\mu_\gamma \mu_{\gamma'}}}{\hbar\sqrt{|k'_{\gamma'}||k_\gamma|}} \eta_{-}^{*}\left(+k'_{\gamma'}\right) \eta_{+}(-k_\gamma) S^{\gamma'\gamma}_{+k'_{\gamma'}-k_\gamma}. \tag{2.29}$$

Now, we make a slight notation change where the label $\pm$ on the relative momentum corresponds to the four possible combinations of $|\pm\Psi^{\gamma}_{in(out)}\rangle$. Inverting Equation 2.29, we obtain the on–shell S–matrix element for scattering from the state $|-k_\gamma, \gamma\rangle$ to the state $|+k_{\gamma'}, \gamma'\rangle$,

$$S^{\gamma'\gamma}_{+k'_{\gamma'}-k_\gamma} = \frac{(2\pi)^{-1}\hbar}{\eta_{-}^{*}\left(+k'_{\gamma'}\right)\eta_{+}(-k_\gamma)} \sqrt{\frac{|k'_{\gamma'}||k_\gamma|}{\mu_\gamma \mu_{\gamma'}}} \langle \Psi_{-}^{\gamma'} | A_{+}^{\gamma}(E) \rangle, \tag{2.30}$$

where the scalar product $\langle \Psi_{-}^{\gamma'} | A_{+}^{\gamma}(E) \rangle$ is given by the Fourier transform of the correlation function $\langle \Psi_{-}^{\gamma'} | \exp\left(\frac{-iHt}{\hbar}\right) | \Psi_{+}^{\gamma} \rangle$,

$$\langle \Psi_{-}^{\gamma'} | A_{+}^{\gamma}(E) \rangle = \int_{-\infty}^{+\infty} dt \exp\left(\frac{iEt}{\hbar}\right) \langle \Psi_{-}^{\gamma'} | \exp\left(\frac{-i\hat{H}t}{\hbar}\right) | \Psi_{+}^{\gamma} \rangle. \tag{2.31}$$

The numerical implementation of Equations 2.30 and 2.31 will be covered as part of the next section.

2.6 *Numerical implementation*

The numerical implementation of the channel packet method is fairly straight forward. In this section, we will outline the steps involved in computing S-matrix elements for the collinear reaction

$$A + BC(\nu) \rightarrow AB(\nu') + C \tag{2.32}$$

where the internal diatom eigenstates are labeled ν and ν'. The actual calculation of S-matrix elements can be broken into three broad sections: calculating the Møller states, calculating the correlation function and calculating S–matrix elements.

2.6.1 Calculating the Møller states. Numerically, the reactant Møller state is calculated in the following manner. In the asymptotic limit of subchannel γ, the asymptotic channel Hamiltonian is separable using Jacobi coordinates according to Equation 2.7. $\hat{H}^{\gamma}_{int}$ is a function only of R_γ and $\hat{H}^{\gamma}_{rel}$ is a function only of r_γ. The solutions to $\hat{H}^{\gamma}_{int}$ are diatomic vibrational eigenstates and the solutions to $\hat{H}^{\gamma}_{rel}$ are plane waves. The reactant state $|\Psi^{\gamma}_{in}\rangle$ is the direct product of a single vibrational eigenstate and a linear combination of eigenstates of $\hat{H}^{\gamma}_{rel}$ given by Equation 2.21. The reactant state $|\Psi^{\gamma}_{in}\rangle$ is then transformed to bond coordinates for propagation. The choice of $t = 0$ and the placement of the wave functions is purely arbitrary, though, the choice of $t = 0$ and placement in the interaction region facilitate the calculation of the correlation function in Section 2.6.2.

The state $|\Psi^{\gamma}_{in}\rangle$ is propagated using the Møller operator $\hat{\Omega}_+$ as follows. The limits $t \rightarrow \pm\infty$ are numerically approximated by $t \rightarrow \pm\tau$ where the time τ is taken to be when the wave packet completely exits the interaction region. The interaction region is taken to be where $\hat{V}^{\gamma}$ is not negligibly small. First, $|\Psi^{\gamma}_{in}\rangle$ is propagated backward in time from $t = 0$ to $t = -\tau$ under $\hat{H}^{\gamma}_{0}$. This can be done analytically

since the internal eigenstate $|\gamma\rangle$ evolves in time as

$$|\gamma(t)\rangle = \exp\left(-i\frac{E_\gamma t}{\hbar}\right)|\gamma(t=0)\rangle, \tag{2.33}$$

and the time evolution of $\eta(k)$ is given by,[53]

$$\begin{aligned}\eta(k) &= \int_{-\infty}^{+\infty} dx \left(2\pi(\Delta x_0)^2\right)^{-\frac{1}{4}} \left(1+\frac{i\hbar t}{2\mu(\Delta x_0)^2}\right)^{-\frac{1}{2}} \\ &\times \exp\left\{\frac{\frac{-(x-x_0)^2}{4(\Delta x_0)^2} + ik_0(x-x_0) - ik_0^2\frac{\hbar t}{2\mu}}{1+\frac{i\hbar t}{2(\Delta x_0)^2\mu}}\right\}\exp(ikx).\end{aligned} \tag{2.34}$$

Equation 2.34 is a complex Gaussian where Δx_0 is the initial wave packet spread in the coordinate representation and k_0 is the initial momentum offset. The advantage to using Equations 2.33 and 2.34 is that half the action of the Møller operator $\hat{\Omega}_\pm^\gamma$, the evolution of the initial state $|\Psi_{in(out)}^\gamma\rangle$ under $\hat{H}_0^\gamma$, can be done analytically.

The numerical propagation is based on the Baker–Campbell–Housdorf theorem[54] which states

$$\exp\left(\hat{A}+\hat{B}\right) = \exp\left(\hat{A}\right)\exp\left(\hat{B}\right)\exp\left([\hat{A},\hat{B}]\right) \tag{2.35}$$

for operators $\hat{A}$ and $\hat{B}$. For the time evolution operator $\hat{U}(t)$, applying the theorem yields

$$\exp[\frac{i}{\hbar}\left(\hat{T}+\hat{V}\right)\Delta t] = \exp\left(\frac{i}{\hbar}\hat{T}\Delta t\right)\exp\left(\frac{i}{\hbar}\hat{V}\Delta t\right)\exp\left(\frac{i}{\hbar}[\hat{T},\hat{V}]\Delta t^2\right), \tag{2.36}$$

where $\hat{T}$ is the kinetic energy operator and $\hat{V}$ is the potential energy operator. Simply neglecting the last term leads to an error on the order of Δt^2 . Instead, we use the split operator approach to achieve the same effect with improved accuracy.[55] The split operator method first splits the Hamiltonian in half before expanding in terms of $\hat{T}$ and $\hat{V}$. Then the Baker–Campbell–Housdorf is applied to the two exponentials.

This leads to an approximation of Equation 2.36 given by

$$\exp[\frac{i}{\hbar}\left(\hat{T}+\hat{V}\right)\Delta t] \approx \exp\left(\frac{i}{2\hbar}\hat{V}\Delta t\right)\exp\left(\frac{i}{\hbar}\hat{T}\Delta t\right)\exp\left(\frac{i}{2\hbar}\hat{V}\Delta t\right)+\mathcal{O}\left(\Delta t^3\right), \tag{2.37}$$

where the error in the approximation is on the order of Δt^3 instead of Δt^2. In Equation 2.37, the potential operator is diagonal in the coordinate representation and the kinetic energy operator is diagonal in the momentum representation. The transformation between the two representations is a Fourier transform pair given by

$$g(k)=\mathcal{F}^{-1}\{g(x)\}=\frac{1}{\sqrt{2\pi}}\int_{-\infty}^{+\infty}dx\exp(i2\pi kx)\,g(x), \tag{2.38}$$

and

$$g(x)=\mathcal{F}\{g(k)\}=\frac{1}{\sqrt{2\pi}}\int_{-\infty}^{+\infty}dk\exp(-i2\pi kx)\,g(k). \tag{2.39}$$

Numerical propagation proceeds by first defining a coordinate grid and a momentum grid using the bond coordinate representation. The coordinate grid is used to determine the diagonal representation of $\exp\left(\frac{i}{2\hbar}\hat{V}\Delta t\right)$ and the momentum grid is used to determine the diagonal representation of $\exp\left(\frac{i}{\hbar}\hat{T}\Delta t\right)$. The initial reactant wave packet $\Psi(r_\gamma, R_\gamma, t=0)$ is transformed to the bond coordinate representation and using Equation 2.40 the wave packet at $t+\Delta t$ is computed,

$$|\Psi_+^\gamma(t+\Delta t)\rangle=\exp\left(\frac{i}{2\hbar}\hat{V}\Delta t\right)\mathcal{F}\{\exp\left(\frac{i}{\hbar}\hat{T}\Delta t\right)\mathcal{F}^{-1}\{\exp\left(\frac{i}{2\hbar}\hat{V}\Delta t\right)|\Psi_+^\gamma(t)\rangle\}\}. \tag{2.40}$$

In order to efficiently propagate using Equation 2.40, we use Fast Fourier transforms (FFTs). Repeated application of Equation 2.40 iteratively determines the wave packet at time τ. The calculation of the product state is similar.

2.6.2 Calculating the correlation function. With the two Møller states $|\Psi_+\rangle$ and $|\Psi_-\rangle$ calculated at $t=0$, the next step is to compute the correlation

function in Equation 2.31 and given by

$$C_{\gamma'\gamma}(t) = \langle \Psi_-^{\gamma'} | \exp\left(\frac{-i\hat{H}t}{\hbar}\right) | \Psi_+^{\gamma} \rangle. \tag{2.41}$$

We need to know $C_{\gamma'\gamma}(t)$ from time $t = -\tau$ to $t = \tau$ in order to take the Fourier transform in Equation 2.31. First, the reactant Møller state $|\Psi_+\rangle$ is propagated from time $t = 0$ to $t = \tau$ under the full scattering Hamiltonian $\hat{H}$. Second, the reactant Møller state $|\Psi_+\rangle$ at $t = 0$, is propagated from time $t = 0$ to $t = -\tau$ under the full scattering Hamiltonian $\hat{H}$ again computing the correlation at each step. It is in calculating the correlation function that absorbing boundary conditions are applied since the Møller states are typically well localized in the interaction region at $t = 0$. The absorbing boundary conditions are applied in an area where $|\Psi_-^{\gamma'}(t = 0)\rangle$ is already zero thus $C_{\gamma'\gamma}$ is zero and the absorbing boundary conditions do not affect its value. The form of the absorbing boundary conditions, on the discretized numeric grid, are altered slightly from those in Equation 2.8 by the multiplication of a step function so that the absorbing boundary conditions are in fact zero where $|\Psi_-^{\gamma'}(t = 0)\rangle$ is non-zero. The absorbing boundary conditions, as implemented numerically are given by

$$V_a = \pm h(x - x_0) Ai \exp\left\{\frac{(x - x_0)^2}{B}\right\}, \tag{2.42}$$

where $h(x - x_0)$ is the heavyside step function given by

$$h(x - x_0) = \begin{pmatrix} 1, & x_0 \leq x \\ 0, & \text{otherwise} \end{pmatrix}. \tag{2.43}$$

2.6.3 Calculating S-matrix elements. In the channel packet method, the formula for computing S-matrix elements is contained in Equations 2.30 and

2.31. Numerically, the starting point is Equation 2.31 given by

$$\begin{aligned}\langle \Psi_-^{\gamma'} | A_+^{\gamma}(E) \rangle &= \int_{-\infty}^{+\infty} dt \exp\left(\frac{iEt}{\hbar}\right) \langle \Psi_-^{\gamma'} | \exp\left(\frac{-i\hat{H}t}{\hbar}\right) | \Psi_+^{\gamma} \rangle \\ &= \int_{-\infty}^{+\infty} dt \exp\left(\frac{iEt}{\hbar}\right) C_{\gamma'\gamma}(t), \end{aligned} \tag{2.44}$$

where $C_{\gamma'\gamma}(t)$ is the correlation function computed in the previous section. Numerically, Equation 2.44 is implemented by taking the discrete Fourier transform of the correlation function computed in Section 2.6.2. We are free to chose the grid on which the discrete Fourier transform is taken. The best choice is an energy grid where the underlying momenta, recall $E = \frac{\hbar^2 k^2}{2\mu}$, are such that the expansion coefficients $\eta_\pm$ in Equation 2.21 are numerically non-zero. This ensures that the normalization by the expansion coefficients in the numeric implementation of Equation 2.30 does not lead to numeric error caused by dividing large numbers by small numbers. After taking the discrete Fourier transform of the correlation function, the computation of S–matrix elements using Equation 2.30 is simple and straight forward. The probability of reaction is given by

$$P_{k'_{\gamma'} k_\gamma}^{\gamma'\gamma} = |S_{k'_{\gamma'} k_\gamma}^{\gamma'\gamma}|^2, \tag{2.45}$$

where $S_{k'_{\gamma'} k_\gamma}^{\gamma'\gamma}$ are the S–matrix elements computed from Equation 2.30.

III. One dimensional quantum scattering

As an introduction to quantum scattering, the channel packet method with absorbing boundary conditions was applied to quantum scattering in one dimension for two systems: A square well, and a Gaussian well with Gaussian barriers.

3.1 One dimensional square well

The computation of S–matrix elements begins with Schrödinger's Equation in one dimension,

$$i\hbar\frac{d}{dt}\Psi(t) = \hat{H}\Psi(t), \tag{3.1}$$

where the Hamiltonian $\hat{H}$ is given by

$$\hat{H} = \hat{T} + \hat{V}, \tag{3.2}$$

$\hat{T}$ is the kinetic energy operator and $\hat{V}$ is the potential operator. Since there is only a single degree of freedom, the particle has no internal structure. The formula for S–matrix elements using the channel packet method, given in Equation 2.30, simplifies to

$$S_{k'k} = \frac{(2\pi)^{-1}\hbar}{\eta_-^*(+k')\,\eta_+(-k)}\frac{\sqrt{|k'||k|}}{m}\langle\Psi_-|A_+(E)\rangle, \tag{3.3}$$

where the scalar product $\langle\Psi_-|A_+(E)\rangle$ is given by the Fourier transform of the correlation function

$$\langle\Psi_-|A_+(E)\rangle = \int_{-\infty}^{+\infty} dt \exp\left(i\frac{Et}{\hbar}\right)\langle\Psi_-|\exp\left(-i\frac{\hat{H}t}{\hbar}\right)|\Psi_+\rangle. \tag{3.4}$$

The mathematical form of the one dimensional square well is given by

$$V(x) = \left\{ \begin{array}{l} -V_0,\ -a \le x \le a \\ 0,\ \text{otherwise} \end{array} \right\}, \tag{3.5}$$

where the potential $V(x)$ is non-zero from $x = -a$ to $x = a$. This square well is shown in Figure 3.1. It should be noted that the sides of the one dimensional square well are discontinuous at $x = \pm a$. This discontinuity and the impact on the numerical implementation is discussed further in Section 3.1.1

For the potential illustrated in Figure 3.1, the scattering is elastic and S–matrix elements are non-zero only for $|k'| = |k|$. For a one dimensional square well potential energy surface the Hamiltonian is given by

$$\hat{H} = \frac{P^2}{2m} + \left\{ \begin{array}{l} -V_0,\ -a \leq x \leq a \\ 0,\ \text{otherwise} \end{array} \right\} \tag{3.6}$$

and the probability of transmission, given by $P_{k'k} = |S_{k'k}|^2$, has an analytic solution[56,57] given by

$$P(E) = [\cos^2(2ka) + \left(\frac{\epsilon'}{2}\right)^2 \sin^2(2ka)]^{-1}, \tag{3.7}$$

with

$$k = \sqrt{\frac{2m}{\hbar^2}(E - V_0)} \tag{3.8}$$

$$k' = \sqrt{\frac{2m}{\hbar^2}E} \tag{3.9}$$

$$\text{and} \quad \epsilon' = \frac{k}{k'} + \frac{k'}{k}, \tag{3.10}$$

where $2a$ is the well width, V_0 is the well depth, E is the particle energy and m the particle mass.

3.1.1 Choosing the grid. The first step in applying the channel packet method to a given scattering problem is determining the grid parameters. Kosloff's seminal article[58] on time dependent scattering outlines the constraints on choosing grids. Consider first the total energy a particle may have during the scattering event.

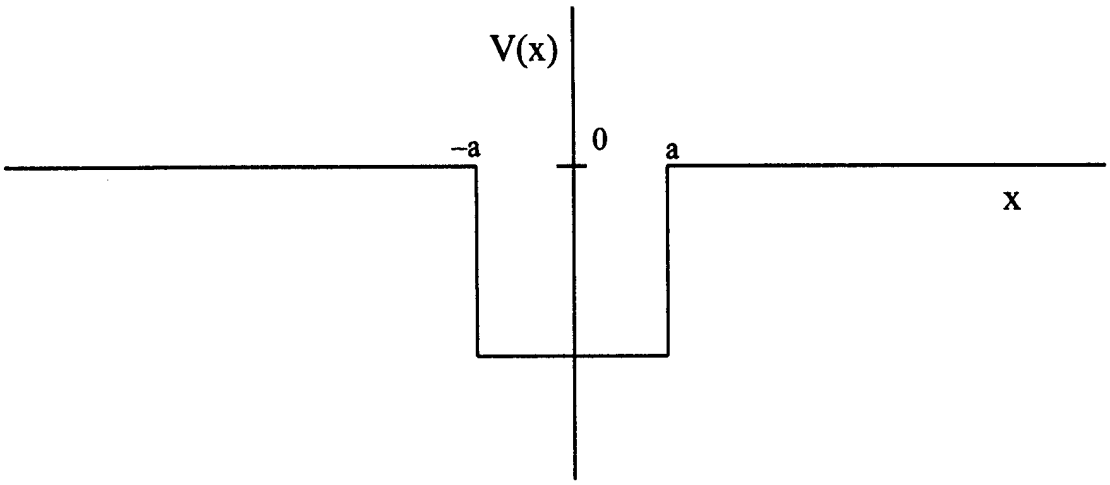

Figure 3.1 One dimensional square well of width $2a$ and depth V_0.

The total energy, $E_{\max}$, given by

$$E_{\max} = E_{int} + T_{\max} - V_{\max}, \tag{3.11}$$

is not the same as the expectation value of the Hamiltonian $\langle \hat{H} \rangle$. Instead, it is a combination of the maximum translational energy, the maximum potential energy and the internal energy. In one dimensional scattering, there is no internal energy to consider, leaving only translational and potential energy. The maximum translational energy is taken to be the energy of the single component of the wave packet with the highest absolute value of k. For the potential energy, the maximum depth of the potential well is added to the total energy in Equation 3.11. Barrier energies are not subtracted from the total energy.

From the total energy, the maximum value of the momentum grid, $k_{\max}$ is derived through the relationship between energy and momentum for non-relativistic scattering,

$$\hbar k_{\max} = \sqrt{2mE_{\max}}. \tag{3.12}$$

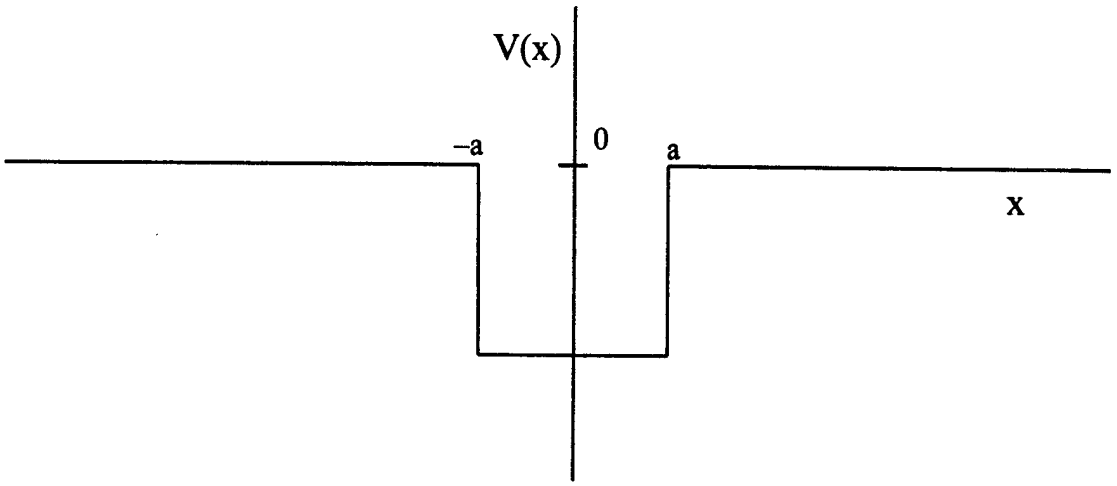

Figure 3.1 One dimensional square well of width $2a$ and depth V_0.

The total energy, $E_{\max}$, given by

$$E_{\max} = E_{int} + T_{\max} - V_{\max}, \tag{3.11}$$

is not the same as the expectation value of the Hamiltonian $\langle \hat{H} \rangle$. Instead, it is a combination of the maximum translational energy, the maximum potential energy and the internal energy. In one dimensional scattering, there is no internal energy to consider, leaving only translational and potential energy. The maximum translational energy is taken to be the energy of the single component of the wave packet with the highest absolute value of k. For the potential energy, the maximum depth of the potential well is added to the total energy in Equation 3.11. Barrier energies are not subtracted from the total energy.

From the total energy, the maximum value of the momentum grid, $k_{\max}$ is derived through the relationship between energy and momentum for non-relativistic scattering,

$$\hbar k_{\max} = \sqrt{2m E_{\max}}. \tag{3.12}$$

The momentum and coordinate representations are related through a Fourier transform pair, given by Equations 2.38 and 2.39. However, this choice of Fourier transform pair requires the channel packet method to make use of a different momentum usually denoted by k_b and given by

$$k_b = \frac{k}{2\pi}. \tag{3.13}$$

Throughout this document, k_b is used and the subscript b is omitted. The Fourier transform pair in Equations 2.38 and 2.39 also yields the relationship between $k_{\max}$ and Δx the coordinate grid spacing,

$$\Delta x = \frac{1}{2k_{\max}}. \tag{3.14}$$

The choice of the maximum value of the coordinate grid is less straightforward. The usual manner in which $x_{\max}$ is determined is to consider the time evolution of the Møller states. The coordinate grid must be large enough to support the evolving Møller states until the calculation of the correlation function can be terminated. The purpose behind using absorbing boundary conditions is to decrease the size of the grid and exponentially attenuate the evolving Møller state before it reaches the edges of the smaller grid. Thus, the grid must only be large enough to contain the interaction region [a] as well as the Møller states at $t = 0$ and the absorbing boundary conditions. The absorbing boundary conditions are placed as close as possible to the Møller states without overlapping them. This maximizes the benefit of using absorbing boundary conditions. The extent of the grid past the point at which the absorbing boundary conditions are placed need only be large enough so that the evolving Møller state is fully attenuated before it reflects from the edge of the grid. Initially, the location of the absorbing boundary conditions is based upon the estimated spatial extent of the Møller states with the absorbing boundary conditions

[a] The area in which the interaction potential is non-zero.

location adjusted later as necessary. The numerical implementation of the channel packet method, discussed in Section 2.6, makes use of FFTs and the Temperton[55] FFT used in this project requires that N be a power of 2. 3 or 5. The most efficient FFT is for N to be a power of 2. In choosing N to be a power of 2, that restriction combined with the estimated $x_{\max}$ leads to choosing N such that it is a power of 2 and $\frac{N}{2} \times \Delta x \geq x_{\max}$. In one dimension, we use $\frac{N}{2}$ since the spatial grid contains both positive and negative values of x and is chosen to be symmetric.

The total energy in Equation 3.11 is also used to determine the time step Δt. Similar to the momentum and coordinate representations. energy and time are also related by a Fourier transform pair which yields the relationship between $E_{\max}$ and $\Delta t_{\max}$,

$$\Delta t_{\max} = \frac{\hbar}{E_{\max}}. \tag{3.15}$$

At this point, the parameters $\Delta t_{\max}$, $k_{\max}$, and Δx have been determined.

The one dimensional square well is discontinuous at $x = \pm a$ as shown in Equation 3.5 and Figure 3.1. Using a discrete spatial variable x leads to a modeling of the discontinuous sides as slopes instead of perfectly vertical. Numerically, it would require an infinite number of points in the spatial grid to reach vertical sides. Fewer points leads to the square well being modeled as a trapezoid. As the number of points increases, the slope of the sides of the trapezoid approaches the perfectly vertical, and discontinuous, sides of the square well. This is shown in Figure 3.2 where the numeric implementation of the analytic square well is shown as the number of grid points increases and their spacing decreases. With an infinite number of points, the numeric potential perfectly matches the analytic potential in Equation 3.5. Using the Δx previously determined, the number of points N needs to be 4096 in order to obtain a numeric solution that is close to the analytic solution.

3.1.2 Møller states. In constructing the initial wave packets, the reactant channel is chosen arbitrarily to be the left side of the potential, $x < 0$, and

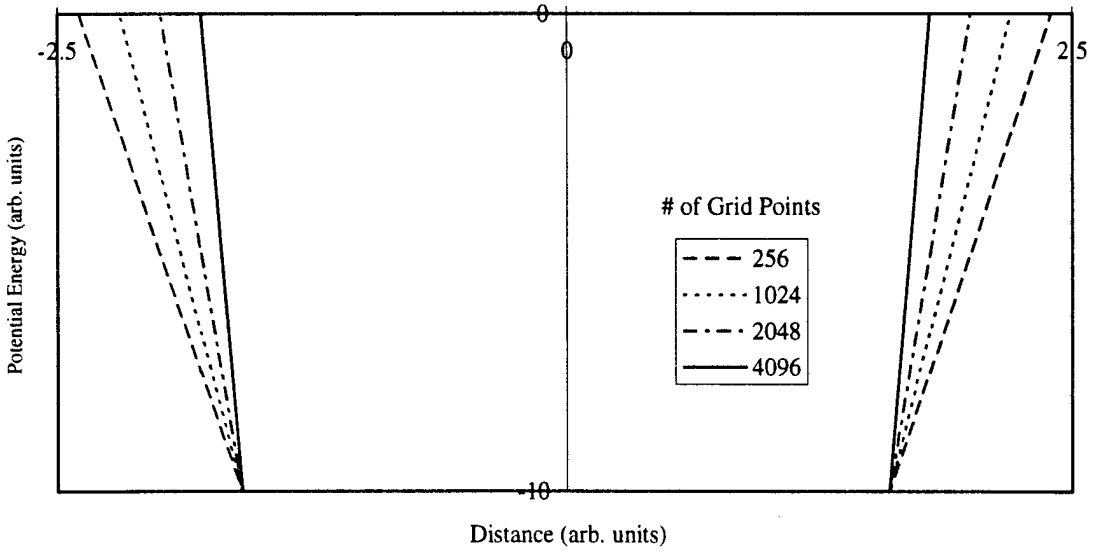

Figure 3.2 The discontinuous sides of the one dimensional square well modeled as trapezoidal sides.

the product channel is the right side of the potential, $x > 0$. Compact Møller states are important in reducing the overall grid size and the most compact Møller states for scattering from a one dimensional square well are those with an initial spread in the coordinate representation less than the width of the well. This determination of compactness is based solely on trial and error. In this case, the reactant Møller state was computed for a range of initial spreads and then plotted on the spatial grid. After a few trials, it became clear that the narrower spreads were leading to more compact Møller states. The trials were then performed again to find the most compact Møller state, i.e. narrowest spatial spread, without excessive spread in the momentum representation as the spread in k is inversely proportional to the spread in x. The two wave packets, representing reactants and products, have zero coordinate offset and the same spread in the coordinate representation in order to locate the compact Møller states in the interaction region. The momentum offset must be large enough so that the initial wave packet, in the momentum representation, has only

positive or negative momentum in order to apply the formula for S–matrix elements given in Equation 3.3. With the initial wave packets created, the reactant Møller state is computed by propagating the initial reactant wave packet backward in time analytically using Equation 2.34 and then forward in time numerically under the full scattering Hamiltonian $\hat{H}$ using the split operator approximation. Likewise, the product Møller state is computed by propagating the initial product wave packet forward in time analytically and then backward in time numerically under the full scattering Hamiltonian.

3.1.3 Correlation function. In calculating the correlation function, the reactant Møller state remains at $t = 0$ and the product Møller state evolves in time. First, the product Møller state is propagated from $t = 0$ to $t = -\tau$ while computing the correlation function at every step. Second, the product Møller state at $t = 0$, which is stored in memory, is propagated to $t = +\tau$, again computing the correlation function at every step. Without the use of absorbing boundary conditions, the coordinate grid would have to be large enough to support the evolving Møller state; instead, absorbing boundary conditions are used to exponentially attenuate the evolving Møller state and prevent reflection from the edges of the smaller grid. The form of the absorbing boundary conditions, given in Equation 2.8, needs only three parameters, $A, B,$ and x_0. The choice of x_0 is based on the spatial extent of the Møller states and is chosen so that the absorbing boundary conditions begin close to the Møller states but that the Møller states are numerically zero at x_0. The parameters A and B are determined by the need to fully absorb the evolving Møller state while minimizing reflection. Reflection is minimized by selecting an absorbing boundary condition amplitude large enough to absorb the highest energy components of the evolving Møller state. It is also important to avoid the sudden onset of absorbing boundary conditions that will tend to reflect the lower energy components of the evolving Møller state. As investigated in Section 3.2.3, absorbing boundary conditions that reach a height of 7 au are sufficient to fully attenuate the

evolving Møller state before it reaches the edge of the grid. The initial step has only a small effect and should be in the range of 1×10^{-5} to 1×10^{-3}. The parameter A is determined by two competing factors: the need to place the absorbing boundary conditions in as small a space as possible to reduce the grid size while avoiding the steep onset of absorbing boundary conditions. A safe first choice for A is on the order of 1×10^{-5}. While a larger value of A may lead to more compact absorbing boundary conditions, it may possibly lead to reflection errors. A small value will most likely eliminate that possibility.

3.1.4 Results and convergence testing. The initial parameters of the one dimensional square well and the resulting grid parameters, are listed in Table 3.1. The small time step and the fact that potential wells tend to trap long-lived, quasi-bound states requires a long computation time in order for the correlation function to reach zero numerically. The choice of zero is important. Choosing to terminate too early leads to incomplete information for computing S–matrix elements and a resultant oscillation in the probability of transmission. Reviewing the literature reveals that a typical choice for numeric zero is on the order of $|C| = 10^{-6}$.[14–17,21,25,37,38,43,58] This is the cutoff used throughout this research project. The reactant Møller state is shown in Figure 3.3 and the resulting correlation function is shown in Figure 3.4. The probability of transmission, both numeric and analytic, are shown in Figure 3.5. They are in agreement and show that the combination of the channel packet method with absorbing boundary conditions provides a valid approach to computing S–matrix elements. The main source of error is that the discontinuous square sides of the one dimensional square well are computationally modeled as trapezoids.

The performance of a numerical solution needs to be evaluated against two tests of convergence. First, does the solution converge to the correct solution? A solution which converges to a wrong answer is of little use. The channel packet method uses discrete spatial and temporal variables and the solution is only approximate. However, as the spatial and temporal grids are refined, the channel packet

Table 3.1 Initial parameters for scattering from a one dimensional square well.

Parameter	Value (au)	Notes
mass	1.0	Electron mass
Δx	0.005	x grid resolution
nstep	450	Number of time steps for reactant propagation
npstep	1000	Number of time steps for correlation function propagation
Δt	0.001	Time step
ioff	0.0	initial x offset
imom	1.8	initial momentum offset in units of k_b
sprd	0.25	initial wave packet spread in coordinate representation

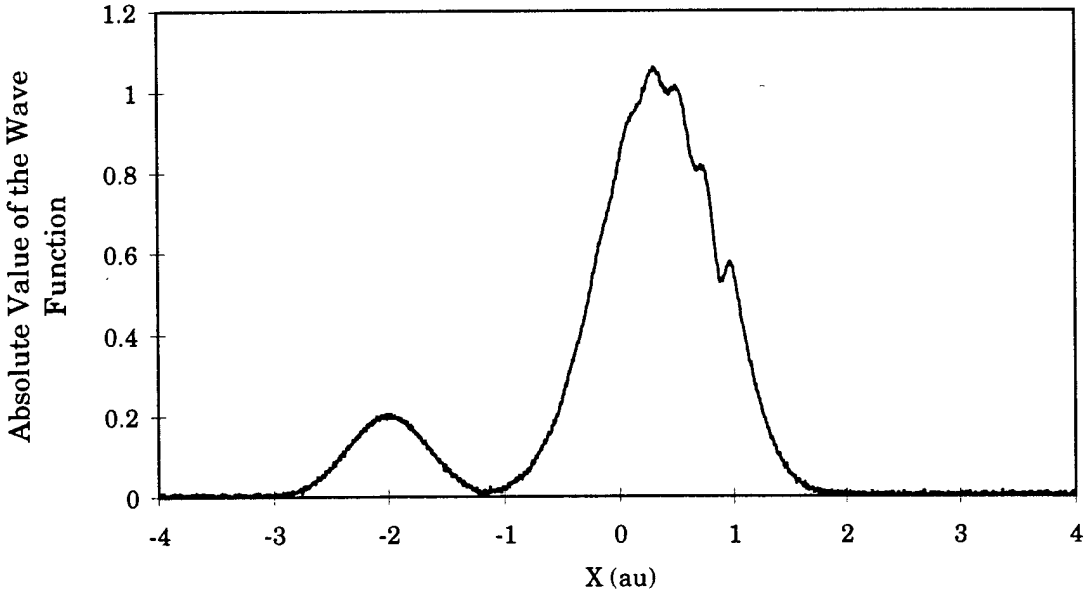

Figure 3.3 Reactant Møller state for a one dimensional square well. The well extends from -1 to 1.

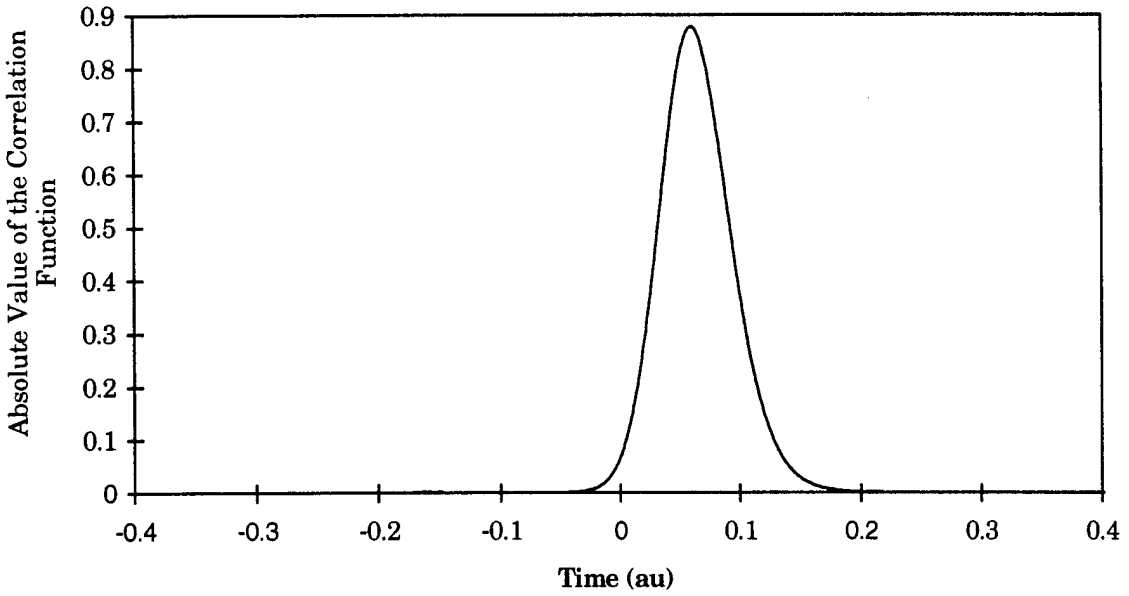

Figure 3.4 Absolute value of the correlation function for scattering from a one dimensional square well.

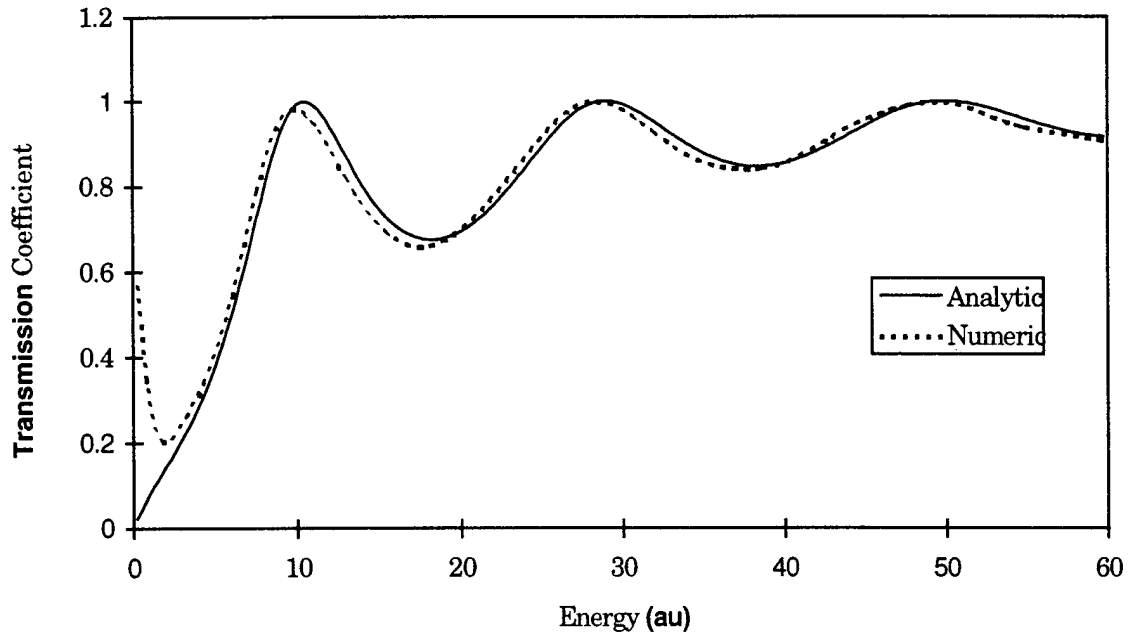

Figure 3.4 Probability of transmission for a one dimensional square well.

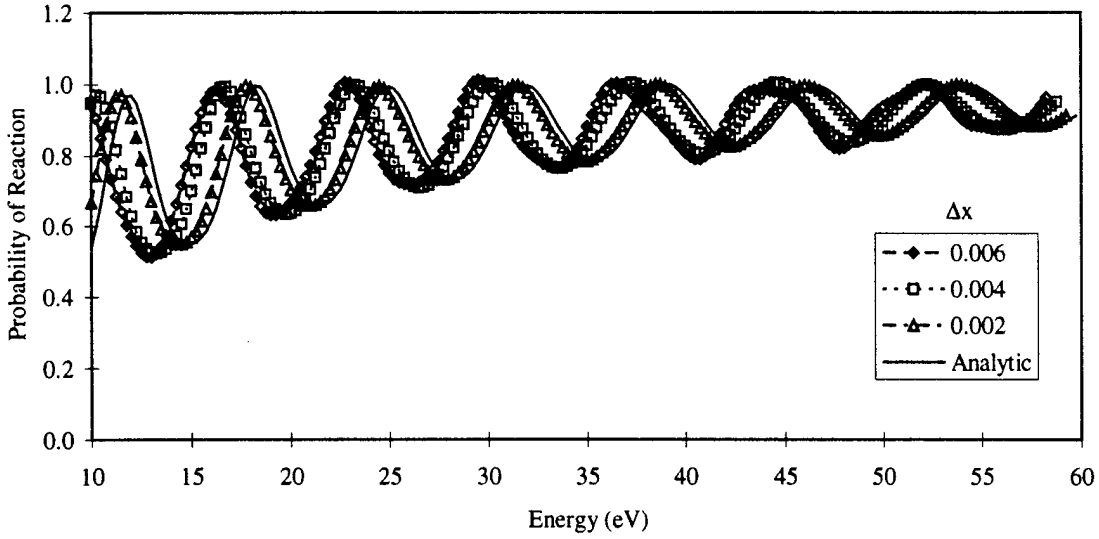

Figure 3.6 Convergence of the channel packet method solution towards the analytic solution for a one dimensional square well.

method should converge to the exact solution. The L_1 norm is used as a measure of convergence and is defined by

$$L_1 = \frac{1}{N} \sum_{j=1}^{N} \frac{|P_{j,analytic} - P_j|}{P_{j,analytic}}, \tag{3.16}$$

where N is the number of points computed in the probability of reaction curve, $P_{j,analytic}$ is the analytic solution at point j and P_j is the calculated probability. The solution is considered to have converged when the L_1 norm has converged to three digits. For the one dimensional square well, this is illustrated in Figure 3.6 where the spatial grid resolution Δx is gradually reduced and the L_1 norm has converged to three digits and the method is considered to have converged to the correct answer.

The second test of convergence illustrates the efficiency of the channel packet method. This test concerns how the approximate solution approaches the analytic solution when one grid resolution is varied while the rest remain fixed. In the first case, the temporal resolution remains fixed while the spatial resolution is changed. In the second case, the temporal resolution is varied while the spatial resolution

remains fixed. However, there is one proviso to the case where the spatial resolution is changed. Since the one dimensional square well, in the approximate solution, consists of trapezoidal sides [b] it is important to model the trapezoidal sides so that the improvement in the accuracy of the solution is due solely to the changes in the spatial grid and not the trapezoidal potential approaching the analytic square well potential. The trapezoidal result of discretizing the spatial grid was discussed in Section 3.1.1 and illustrated in Figure 3.2. In determining the order of convergence for changes in Δx, the one dimensional square well potential given in Equation 3.5 is modified to explicitly model the trapezoidal potential. This new potential is illustrated in Figure 3.7 and given by

$$V(x) = \left\{ \begin{array}{l} 0,\ x \leq -a_0 \\ m_2 \times x + b_2,\ -a_0 \leq x \leq -a \\ -V_0,\ -a \leq x \leq a \\ m_4 \times x + b_4,\ a \leq x \leq a_0 \\ 0,\ x \geq a_0 \end{array} \right\}, \tag{3.17}$$

where $-a_0$ is the boundary between Region I and Region II in Figure 3.7, m_2 and b_2 are the slope and intercept of the trapezoidal side in Region II, $-a$ is the boundary between Region II and Region III, V_0 is the depth of the potential well in Region III, m_4 and b_4 are the slope and intercept of the trapezoidal side in Region IV, and a_0 is the boundary between Region IV and Region V. Changes in the spatial grid resolution where the potential is given by Equation 3.17 has the effect of adding more points to the sloping sides of the trapezoid and not changing the slope of the trapezoid to approach the analytical square well. This ensures that the order of convergence for Δx is due solely to changes in the spatial grid resolution and not to the numerical square well (the trapezoidal well) approaching the analytic square well.

[b] See the discussion near the end of Section 3.1.1.

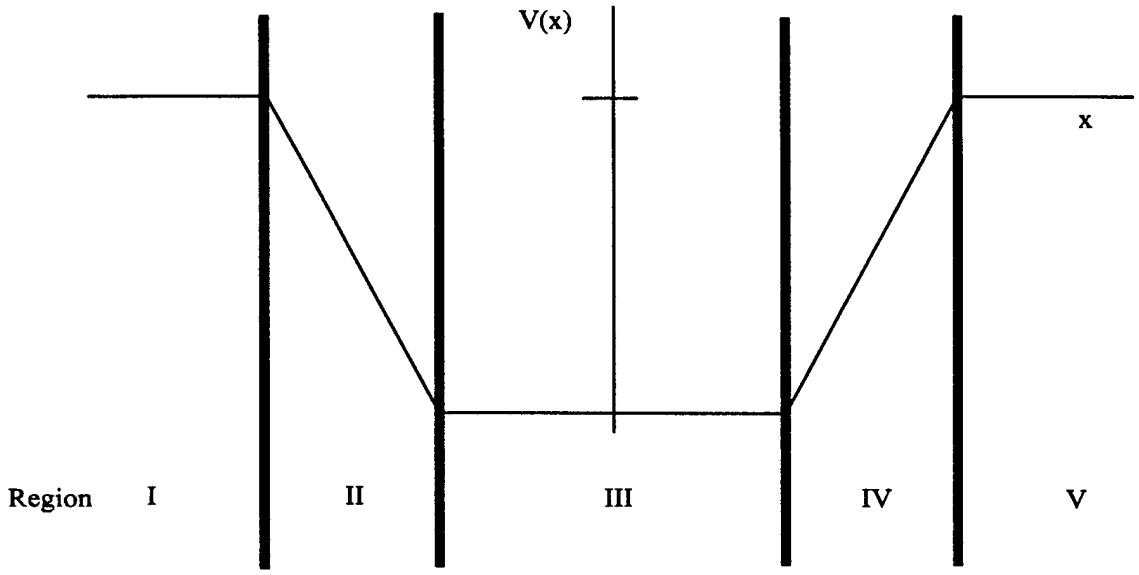

Figure 3.7 One dimensional trapezoid potential well used in determining the order of convergence for changes in Δx.

The efficiency of the numeric solution, also known as the order of convergence, is derived in the following manner. As the resolution of the spatial grid is increased by a factor $\delta = \Delta x_i / \Delta x_{i+1}$, $\Delta x_i > \Delta x_{i+1}$ where Δx is the spatial grid resolution, the error in the approximate solution should be reduced according to

$$\frac{\epsilon_i}{\epsilon_{i+1}} = \delta^n, \tag{3.18}$$

where n is the order of convergence. The relative errors ϵ_i and ϵ_{i+1} are given by

$$\epsilon_i = \frac{|S_\infty - S_i|}{S_\infty}, \tag{3.19}$$

where S_∞ is the benchmark solution. On a log-log plot of the error versus the grid resolution refinement, the order of convergence is the slope of the resulting curve. Methods with a large order of convergence n show a greater reduction in error for a given grid refinement as opposed to those methods with a small order of convergence.

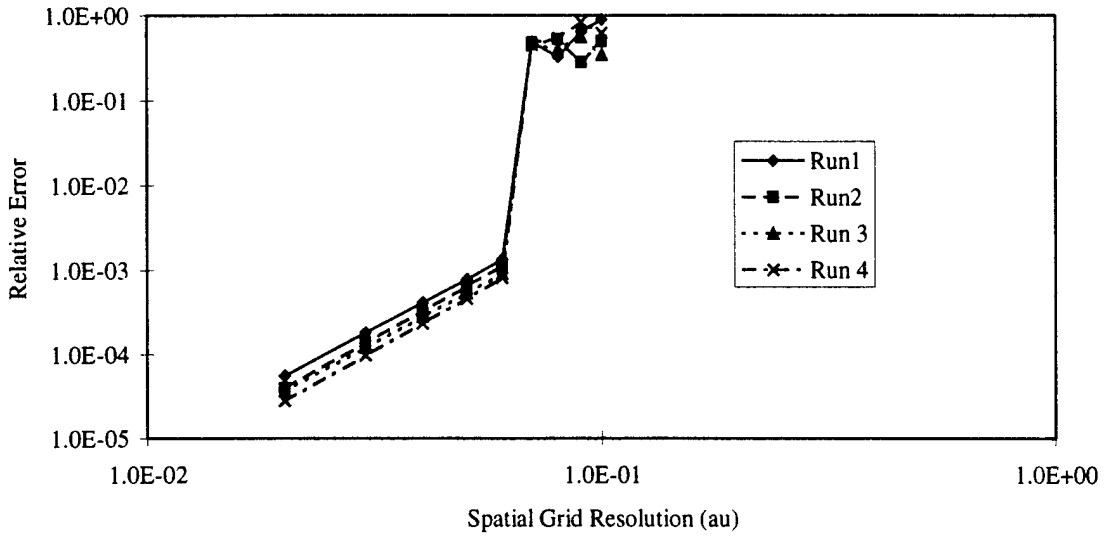

Figure 3.8 In a one dimensional trapezoidal well, relative error vs. changes in spatial grid resolution for the probability of transmission in a one dimensional square well potential.

Figure 3.8 illustrates the convergence behavior of the channel packet method for spatial grid resolution refinement. The four runs, where for each run the shape of the trapezoid was changed in order to reflect a trapezoid approaching a square well, exhibit similar behavior and all four have an order of convergence of 3. The dramatic change and behavior in the relative error for a spatial grid resolution of greater than 0.06 au reflects the rules laid down in Section 3.1.1 for choosing the grid. Using $\Delta x > 0.06$ au results in a maximum momentum grid value that is too small to support the wave function on the momentum grid which leads to spurious behavior and incorrect results for the probability of reaction.

Likewise, Figure 3.9 illustrates the convergence behavior of the channel packet method for temporal grid resolution refinement. Since changes in Δt do not affect the shape of the numeric trapezoidal well, only one potential was needed. For changes in the temporal grid resolution, the channel packet method exhibits an order of convergence of 4. Again, the dramatic change in relative error and the oscillations for $\Delta t > 0.001$ au reflects a violation of the rules in Section 3.1.1.

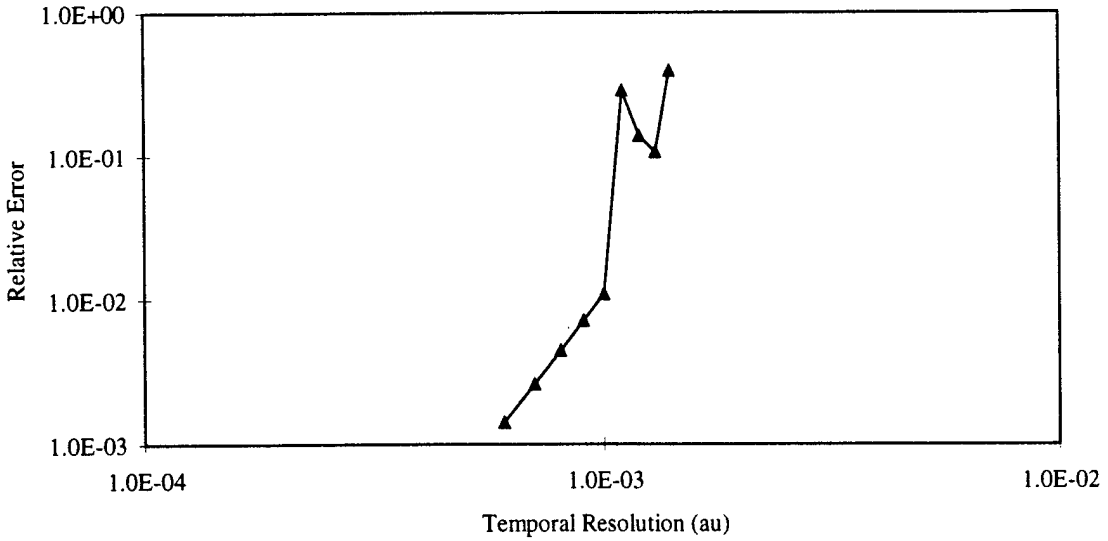

Figure 3.9 In a one dimensional square well, relative error vs. changes in temporal grid resolution for the probability of transmission in a one dimensional square well potential.

3.2 Gaussian well with Gaussian barriers

A Gaussian well with Gaussian barriers provides a smooth potential to investigate the influence of barriers and wells on one dimensional scattering. Since the Gaussian well lacks the discontinuity of the one dimensional square well, the spatial grid requires fewer points in order to effectively model the potential and the computation runs in less time. This allows investigation of many different aspects of one dimensional scattering in a relatively short time.

3.2.1 The potential. The potential is a Gaussian well with symmetric Gaussian barriers,

$$V(x) = A\exp\left\{-(x-x_{1,0})^2\right\} - 0.09\exp\left\{-x^2\right\} + A\exp\left\{-(x-x_{2,0})^2\right\}, \quad (3.20)$$

where A is the height of the barriers and $x_{1,0}$ and $x_{2,0}$ are the left and right offsets for the barriers with the offsets chosen so that the barriers are zero before the well becomes non-zero. Figure 3.10 illustrates the potential for 0.03 au barriers. The

Table 3.2 Initial parameters for scattering from a one dimensional Gaussian barrier-well-barrier potential for a barrier height of 0 au.

Parameter	Value (au)	Note
mass	1224.0	Reduced mass of $H + H_2$ system
Δx	0.10	x grid resolution
nstep	1500	number of time steps for reactant propagation
npstep	1500	number of time steps for product propagation
Δt	1.0	time step
ioff	0.0	initial x offset
imom	1.5	initial momentum offset in units of k_b
sprd	0.55	initial wave packet spread in coordinate representation

initial parameters for the calculation are shown in Table 3.2. The parameter imom is changed with changes in barrier height so that the initial wave packet has a peak energy near the energy of the barrier height. Both the reactant and product wave packets are propagated out to the asymptotic limit under $\hat{H}_0$ to $t = \pm\text{nstep} \times \Delta t$ and back to $t = 0$ under the full scattering Hamiltonian $\hat{H}$. Figure 3.11 illustrates the resulting reactant Møller state for a barrier height of 0.03 au. The correlation function is then calculated for negative times from $t = 0$ to $t = -1 \times \text{nstep} \times \Delta t$. Since this action reverses the propagation from the asymptotic limit to the interaction region, the evolving Møller state quickly exits the interaction region. However, for $t > 0$ the evolving Møller state becomes trapped in the interaction region and the propagation time necessary for the correlation function to reach zero can become very long. The parameter npstep sets the limit for the propagation forward in time to $t = \text{npstep} \times \Delta t$. For a barrier height of 0.05 au, the correlation function reached zero after approximately 200,000 steps compared to the correlation function reaching zero after 1500 time steps for a barrier height of zero. Again, with non-zero barrier heights and without absorbing boundary conditions, the grid would have to be quite large in order to support the evolving Møller state before completely exiting the interaction region. These calculations were performed on a spatial grid of 2048 points. Without absorbing boundary conditions, the spatial grid would have to be 21

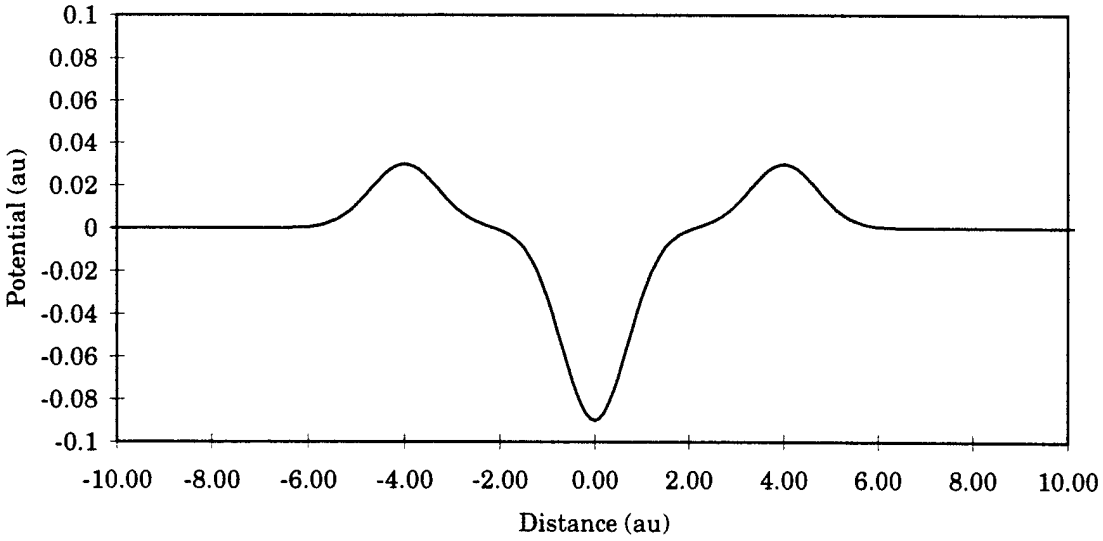

Figure 3.10 Gaussian well bounded by Gaussian barriers.

times larger in order to accommodate the evolving wave packet until the quasi-bound state completely exited the interaction region in the case where the barrier height was 0.05 au. However, the restriction that the number of points in the spatial grid be a power of 2 forces the grid to be 32 times larger instead of 21. An estimate can be made of the cost savings resulting from the smaller grid. Since the majority of the computational effort is in the FFTs, we can estimate the reducting in computational time due to the smaller grid from how an FFT scales computationally. For N a power of 2, the computational cost of an FFT scales as $N \log_2 N$. Using a small grid of N_j points instead of a larger grid of N_l points leads to a savings in the computational effort in the FFT of

$$\xi = \frac{N_l \log_2 N_l}{N_j \log_2 N_j}, \tag{3.21}$$

where ξ is the estimated savings. For the case where the barrier height was 0.05 au, N_j was 2048 and N_l is estimated to be 65536. This leads to an estimated savings of $\xi = 46$.

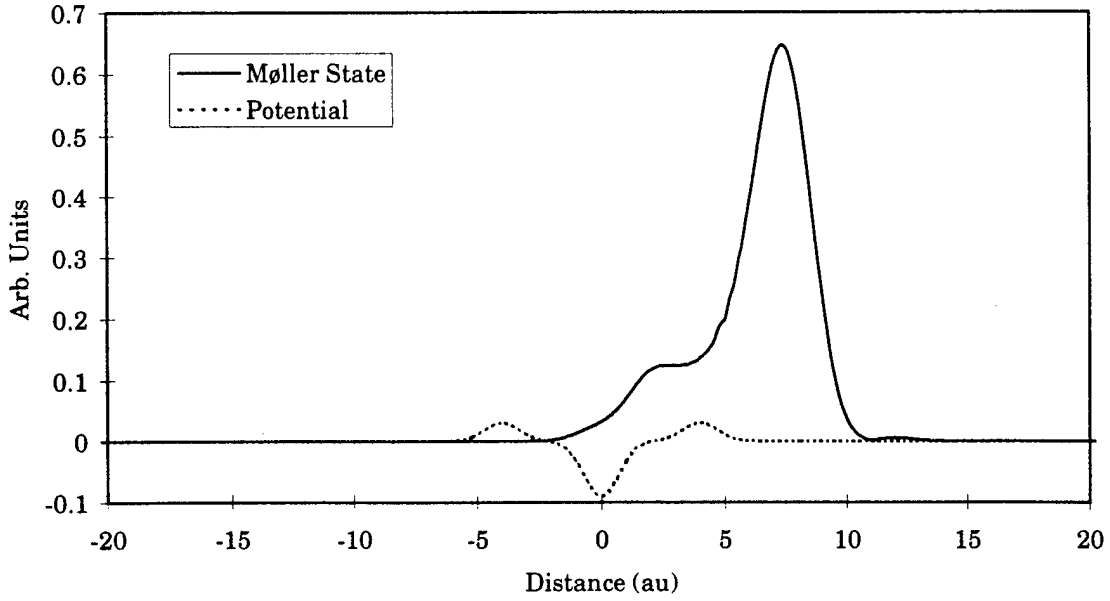

Figure 3.11 Reactant Møller state for a Gaussian barrier-well-barrier potential. The dashed line is the potential and the solid line is the absolute value of the Møller state, $\langle x|\Psi_+(t=0)\rangle$.

3.2.2 S-matrix elements. Figure 3.12 illustrates the probability of transmission for the Gaussian barrier-well-barrier potential. The Gaussian well without barriers exhibits 100% transmission for the range of energies examined using the channel packet method. The high transmission rate is not unexpected due to the smooth nature of the potential. The behavior at very low energies is not resolvable in the channel packet method due to the requirement that the initial wave packet contain no negative momenta. With the addition of barriers at $x = \pm 6$ au, the probability of transmission exhibits significant amplitude below the barrier height, and some reflection at energies above the barrier height. Transmission coefficients computed for all three barrier heights have the same general form. However, the features in each curve are offset in energy by the barrier height. The influence of the barriers is most significant in the quasi-bound states that they trap in the interaction region. A quasi-bound state can be pictured as the part of the evolving Møller state that remains behind in the interaction region after the major part of the evolving Møller state has exited the interaction region. The remaining wave packet is not

Table 3.3 Initial parameters used for the absorbing boundary conditions.

Parameter	Value
B	5.6
A	1.0×10^{-7}
x_0	± 7.3

truly bound; over time the quasi-bound state will exit the interaction region. The overlap between the quasi-bound state and the non-evolving reactant Møller state prevents the correlation function from rapidly approaching zero. Without absorbing boundary conditions, the grids would have to be quite large in order to support the evolving Møller state in the presence of quasi-bound states. For the case where the barrier height is 0.03 au, the spatial grid would have to be 8 times larger.

3.2.3 Influence of absorbing boundary conditions. The Gaussian barrier-well-barrier potential, with a barrier height of 0.03 au, was used to investigate the influence of absorbing boundary conditions on the S–matrix elements. In particular, how do poorly chosen absorbing boundary conditions influence the final result? Three sets of poorly chosen absorbing boundary conditions were investigated: too steep, too shallow and large initial step height. The numeric implementation of absorbing boundary conditions, given in Equation 2.42, leads to a initial step where the absorbing boundary conditions are first non-zero. The Gaussian potential was chosen for two reasons: the overall computation time is short allowing for a wide variety of poor absorbing boundary conditions to be investigated, and the probability of transmission has many features for poorly chosen absorbing boundary conditions to influence. The initial parameters used for the absorbing boundary conditions in the probabilities of transmission illustrated in Figure 3.12 are given in Table 3.3.

Absorbing boundary conditions which are too steep will reflect more strongly than properly chosen absorbing boundary conditions. Table 3.4 lists the values of the parameter B, which governs the steepness in Equation 2.8, for the three sets of

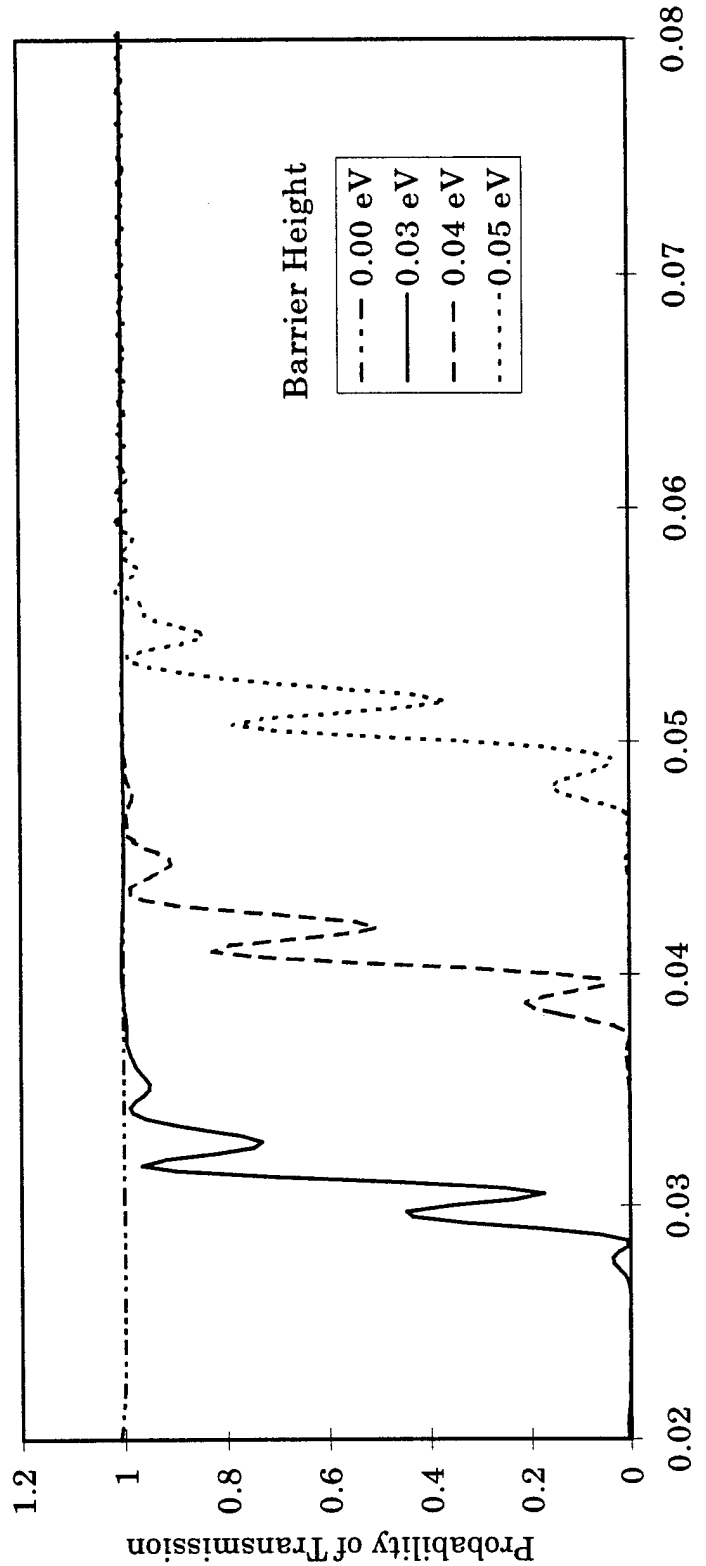

Figure 3.12 Probability of transmission in a Gaussian barrier-well-barrier potential.

Table 3.4 Values for the parameter B used in determining when absorbing boundary conditions are too steep.

Run	B
0	5.6
1	2.0
2	1.0
3	0.1
4	0.01

S–matrix elements shown in Figure 3.13. Run 0 is the value of B for the original absorbing boundary conditions that were used in the calculations of S–matrix elements shown in Figure 3.12. Runs 1 and 2 produced results that were nearly indistinguishable from the results of Run 0. Runs 3 and 4 produced the dramatic changes in the S–matrix elements shown in Figure 3.13. Absorbing boundary conditions which are too steep lead to nearly periodic oscillations in the S–matrix elements that rapidly obscure the correct result. The erroneous probability of transmission elements range from slightly more than 1 to values much more than 1.

Absorbing boundary conditions which are too shallow will not fully attenuate the evolving Møller state. For example, a wave packet headed out the product channel, moving to the right, will reappear in the asymptotic limit of reactant channel, on the left, still moving to the right. This is due to the imposition of periodic boundary conditions by the use of FFTs. The FFT treats the end points of the grid as the same point thus the evolving wave packet wraps around. Table 3.5 lists the values of the parameter B, which governs the steepness in Equation 2.8, for the three sets of S–matrix elements shown in figure 3.14. Again, Run 0 is the original absorbing boundary condition computation. Runs 5 and 6 produced results nearly indistinguishable from Run 0. Run 7 leads to a slight, nearly periodic oscillation overlying the answer in Run 0. Run 8 leads to clear oscillations which are beginning to obscure the correct answer. While absorbing boundary conditions which are too shallow do not fully attenuate the evolving wave packet, they can attenuate a significant por-

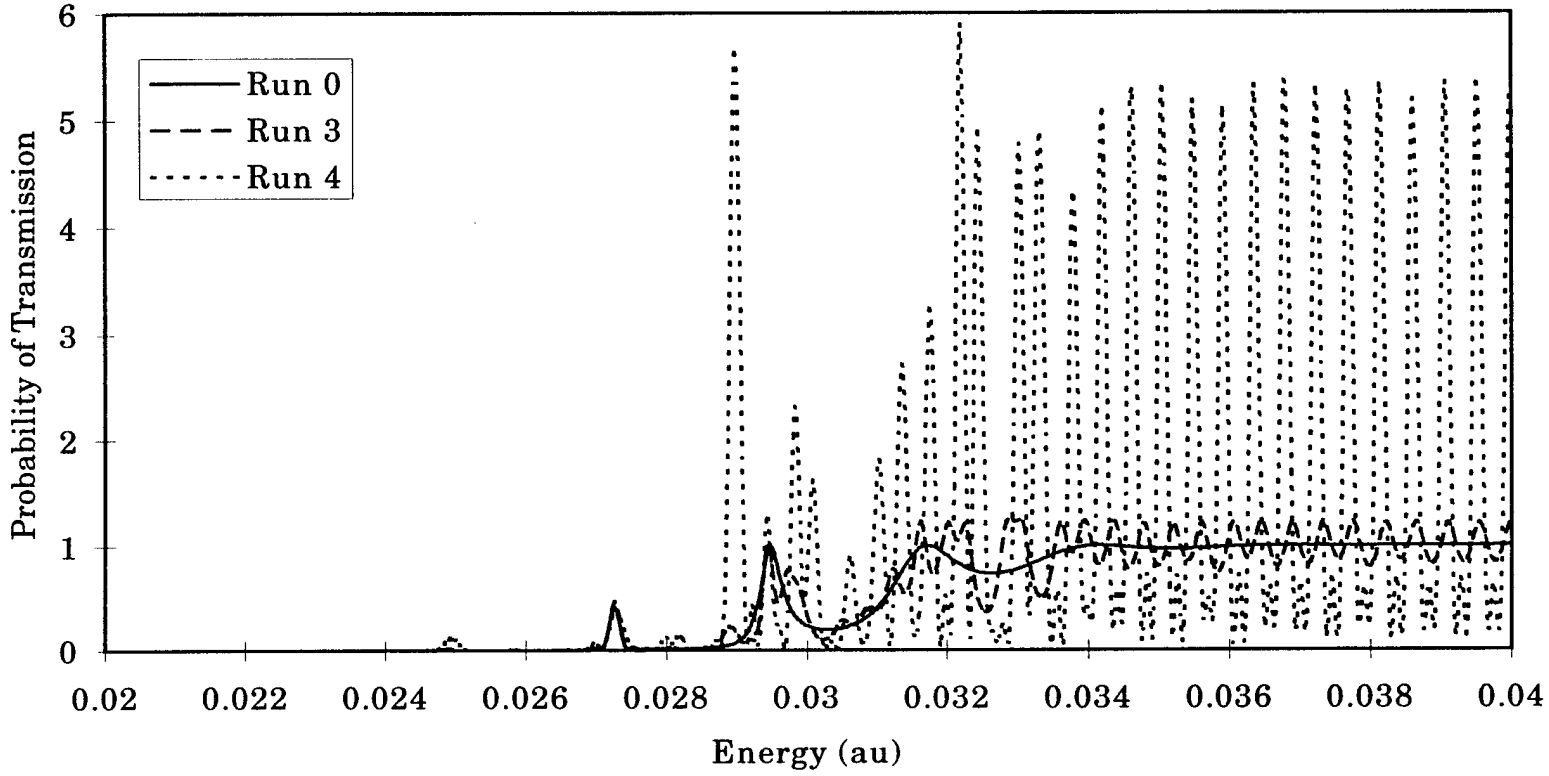

Figure 3.13 Probability of transmission for a Gaussian barrier-well-barrier potential in which the absorbing boundary conditions are too steep.

Table 3.5 Values for the parameter B used in determining when absorbing boundary conditions are too shallow.

Run	B
0	5.6
5	10.0
6	20.0
7	40.0
8	60.0

Table 3.6 Values for the step height parameter A used in determining when the absorbing boundary condition step height is too high.

Run	A
0	1×10^{-7}
9	1×10^{-5}
10	1×10^{-3}

tion of the evolving wave packet introducing less error into the S–matrix elements than absorbing boundary conditions which are too steep. Figure 3.14 illustrates the results when the absorbing boundary conditions are too shallow.

The final set of poorly chosen absorbing boundary conditions concerns the initial step height governed by the parameter A in Equation 2.8. Initially, the step height was fixed at the very low value of 1×10^{-7} in an effort to avoid any reflection from a sudden onset of absorbing boundary conditions. Table 3.6 lists the values of the parameter A for the three sets of S–matrix elements shown in Figure 3.15. The step height was adjusted as well as the steepness B so that the absorbing boundary conditions had the same peak amplitude as in Run 0. Again, Run 0 is the original result. As seen in Figure 3.15, the step height has only a slight influence on the final values of the S–matrix elements. From these computations, a valid first choice of absorbing boundary conditions has a parameter A of 1×10^{-3} and a parameter B such that the absorbing boundary conditions are as shallow as possible while still reaching a peak amplitude greater than 7 au. A valid initial set of

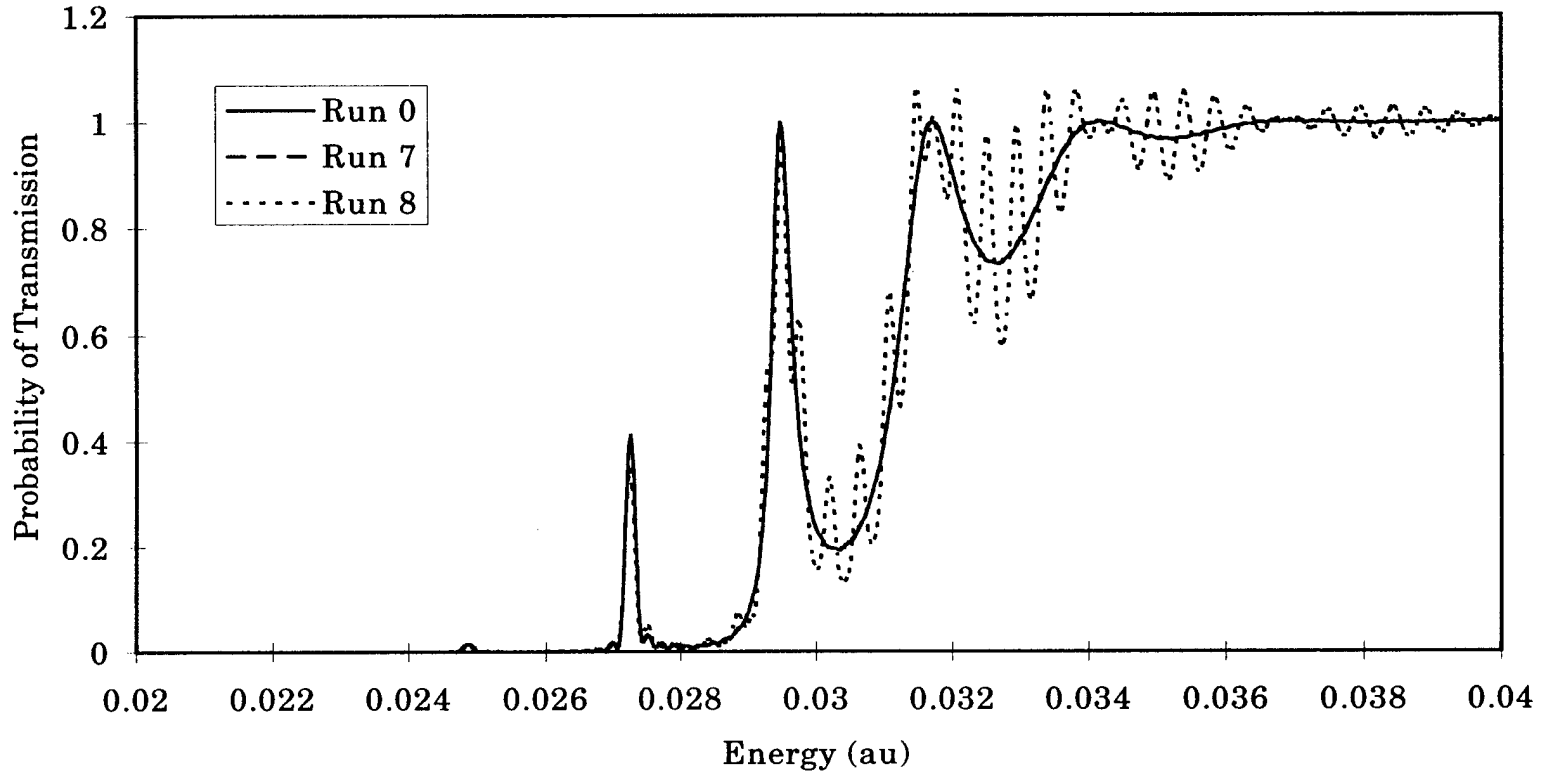

Figure 3.14 Probability of transmission for a Gaussian barrier-well-barrier potential in which the absorbing boundary conditions are too shallow.

absorbing boundary condition parameters based on this analysis is $A = 1 \times 10^{-5}$ and $B = 5.6$. The value of x_0 is dependent on the reaction under consideration can not be determined in advance since it sets the point at which the absorbing boundary conditions are non-zero.

3.3 Summary

Since S–matrix elements for the one dimensional square well have an analytic solution, a comparison of the analytic solution with the computational result, illustrated in Figure 3.5, shows the combination of the channel packet method with absorbing boundary conditions is a valid approach to computing S–matrix elements. The validity of the method is further demonstrated through two tests of convergence. The first, illustrated in Figure 3.6, shows that as the spatial grid resolution is refined, the numeric solution approaches the analytic solution. Second, the channel packet method exhibits third order convergence for spatial grid resolution refinement and fourth order convergence for temporal grid resolution refinement. These orders of convergence are illustrated in Figures 3.8 and 3.9.

Using a Gaussian well with symmetric Gaussian barriers, the effects of barriers and wells on scattering was explored. A well without barriers may or may not trap a quasi-bound state in the interaction region requiring long computation times in calculating the correlation function. However, the addition of barriers does lead to quasi-bound states with possibly long lifetimes. Correct S–matrix elements are rapidly obscured by errors introduced into the correlation function calculation by poorly chosen absorbing boundary conditions as seen in Section 3.2.3. Absorbing boundary conditions which are too steep quickly lead to large oscillations in the probability of transmission and unphysical values much greater than one. Absorbing boundary conditions which are too shallow lead to oscillations in the probability of transmission that rapidly obscure the correct result. However, the initial step height introduced by the numeric implementation of absorbing boundary conditions has

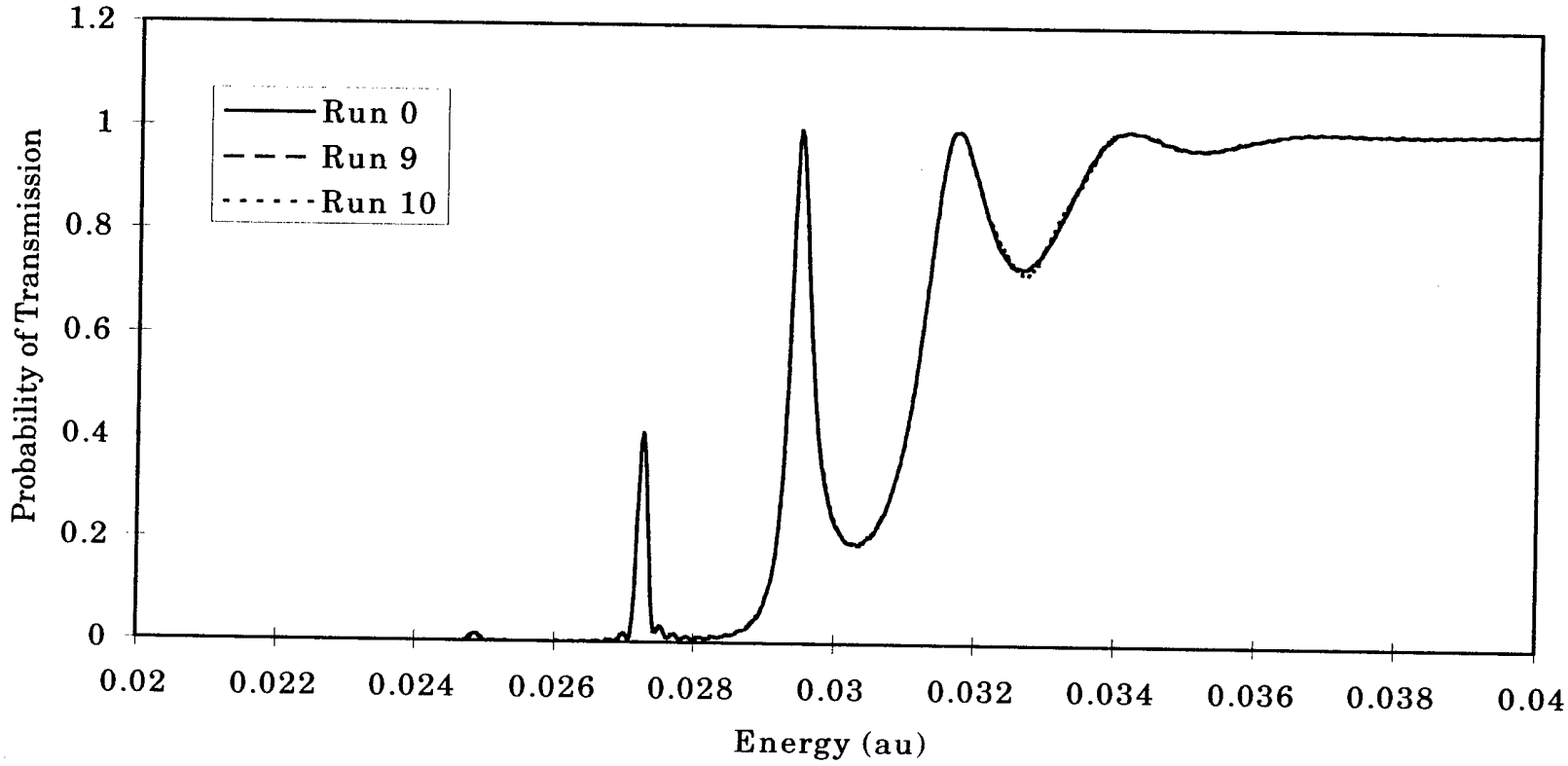

Figure 3.15 Probability of transmission for a Gaussian barrier-well-barrier potential where the intial step height of the absorbing boundary conditions is varied.

only a small influence on the probability of transmission and a choice of 1×10^{-3} for the parameter A in Equation 2.42 is a valid first choice.

IV. Two dimensional $H + H_2$

The two dimensional $H + H_2$ system has been extensively studied and S-matrix elements have been calculated using a wide variety of methods.[17,25,31-35,39] In this study, computing S-matrix elements for collinear $H + H_2$ and comparing the results with previous work provides proof of concept for the combination of absorbing boundary conditions with the channel packet method.[41]

4.1 Background

Liu, Siegbahn, Truhlar and Horowitz (LSTH) have computed a highly accurate potential energy surface for collinear $H + H_2$.[59,60] The LSTH potential energy surface, which is accurate to within 0.1% of the true potential, is characterized by two troughs parallel to the relative coordinate in each of the channels $H + H_2$ and $H_2 + H$, and a saddle point, or barrier, in the interaction region. Computations involving the $H + H_2$ system are simplified by the barrier in the interaction region. Figure 4.1 is a contour plot of the LSTH potential energy surface. The plain in the upper right corner of Figure 4.1 represents the $H+H+H$ channel and is energetically inaccessible in this study.

The application of the channel packet method begins with the definition of two initial wave packets $\Psi_{in}^{1,\nu}(X,Y)$ and $\Psi_{out}^{2,\nu'}(X,Y)$ at $t = 0$, where X and Y are the bond coordinates describing the three collinear hydrogen atoms.[42] The first wave packet $\Psi_{in}^{1,\nu}(X,Y)$ is used to describe the incoming reactants, $H + H_2(\nu)$, in arrangement channel 1 where the diatom is prepared in a single vibrational eigenstate labeled ν. A Gaussian wave packet is used to describe the wave packet in the relative coordinate between H and H_2. The second wave packet $\Psi_{out}^{2,\nu'}(X,Y)$ is used to represent outgoing products $H_2(\nu') + H$ in arrangement channel 2 where the diatom is in a single vibrational eigenstate labeled ν'. Again, a Gaussian wave packet is used to describe the wave packet in the relative coordinate between H_2

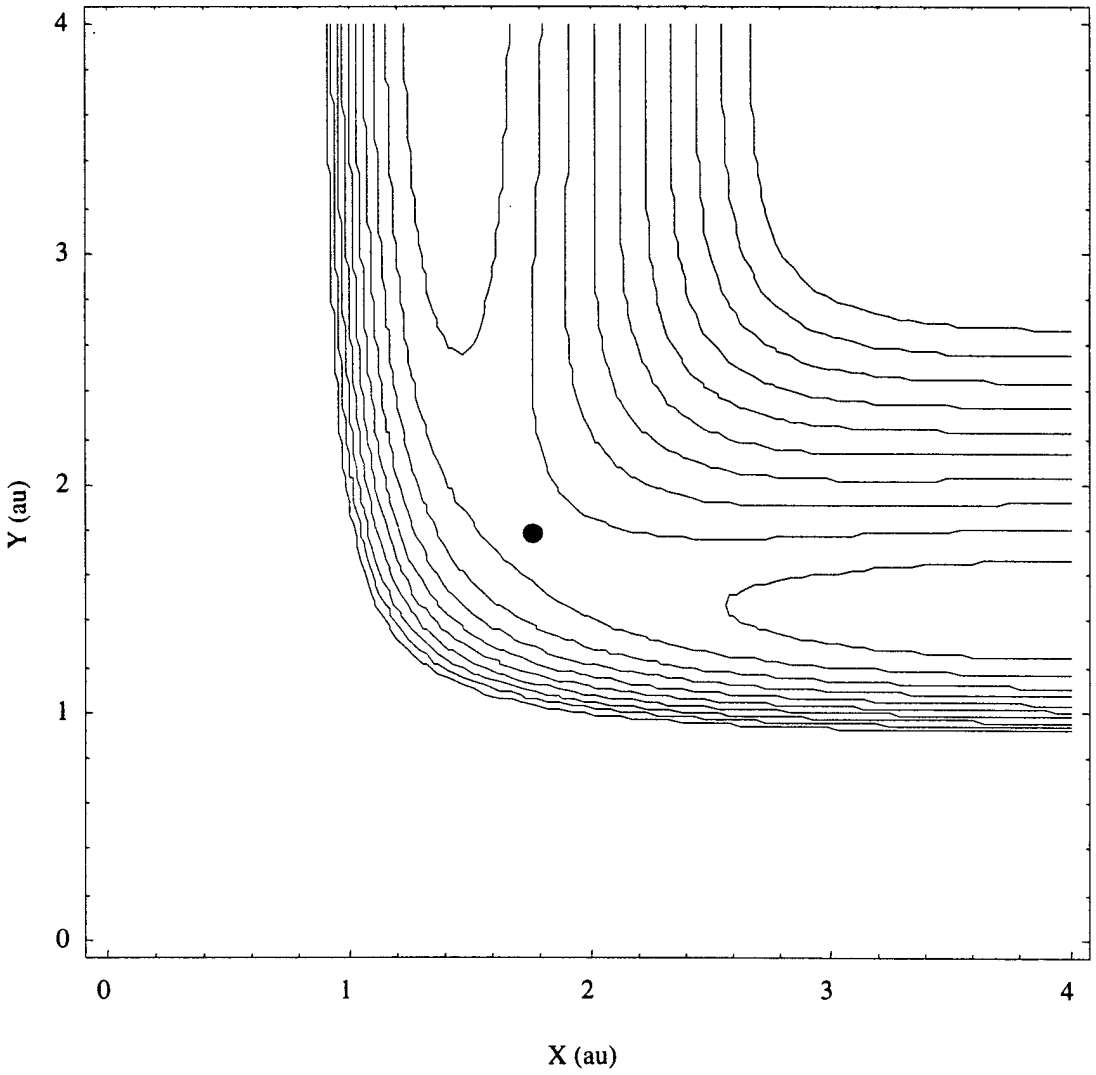

Figure 4.1 Contour plot of the LSTH potential energy surface. The contour lines are evenly spaced from 0 au to 0.1 au. The saddle point is marked with a dot.

and H. The next step is to compute a pair of intermediate states obtained from the initial states by propagating $\Psi_{in}^{1,\nu}(X,Y)$ backward in time to $t = -\infty$ using the asymptotic channel Hamiltonian $\hat{H}_0^1$ and propagating $\Psi_{out}^{2,\nu'}(X,Y)$ forward in time to $t = +\infty$ using the channel Hamiltonian $\hat{H}_0^2$. This is illustrated in Figure 4.2 where infinity is reached numerically at $t = -4000$ au. The intermediate reactant (product) states are then propagated from $+\infty\,(-\infty)$ using the full Hamiltonian backward (forward) to time $t = 0$ to obtain the reactant (product) Møller states. The correlation function between the resulting reactant and product Møller states is then computed using absorbing boundary conditions as they continue to evolve forward and backward in time to $t = \pm\infty$. The application of absorbing boundary conditions with the channel packet method when computing the correlation function is facilitated by the fact that the resulting reactant and product Møller states are typically well localized in the interaction region of the potential at $t = 0$. The well localized Møller states $\Psi_{+}^{1,0}(X,Y)$and$\Psi_{-}^{2,0}(X,Y)$ are shown in Figures 4.3 and 4.4. To compute the correlation function, we choose one Møller state to evolve while the other remains static. The evolving Møller state will eventually reach the absorbing boundary conditions and be exponentially attenuated. However, since the absorbing boundary conditions are placed where the static Møller state has zero amplitude, there is no overlap between the static Møller state and the evolving Møller state in the region where the evolving state is being attenuated. The correlation function is therefore unaffected by the absorbing boundary conditions. Figure 4.5 illustrates the placement of absorbing boundary conditions with respect to the Møller states. S–matrix elements are then obtained from the Fourier transform of the correlation function.[25,37,38]

Recently, Jäckel and Meyer[46] employed absorbing boundary conditions in a version of the channel packet method adapted to work with a time-dependent-self-consistent-field approach to compute S–matrix elements for the collinear $H + H_2$ reaction. Dai and Zhang[36] have also used absorbing boundary conditions with the

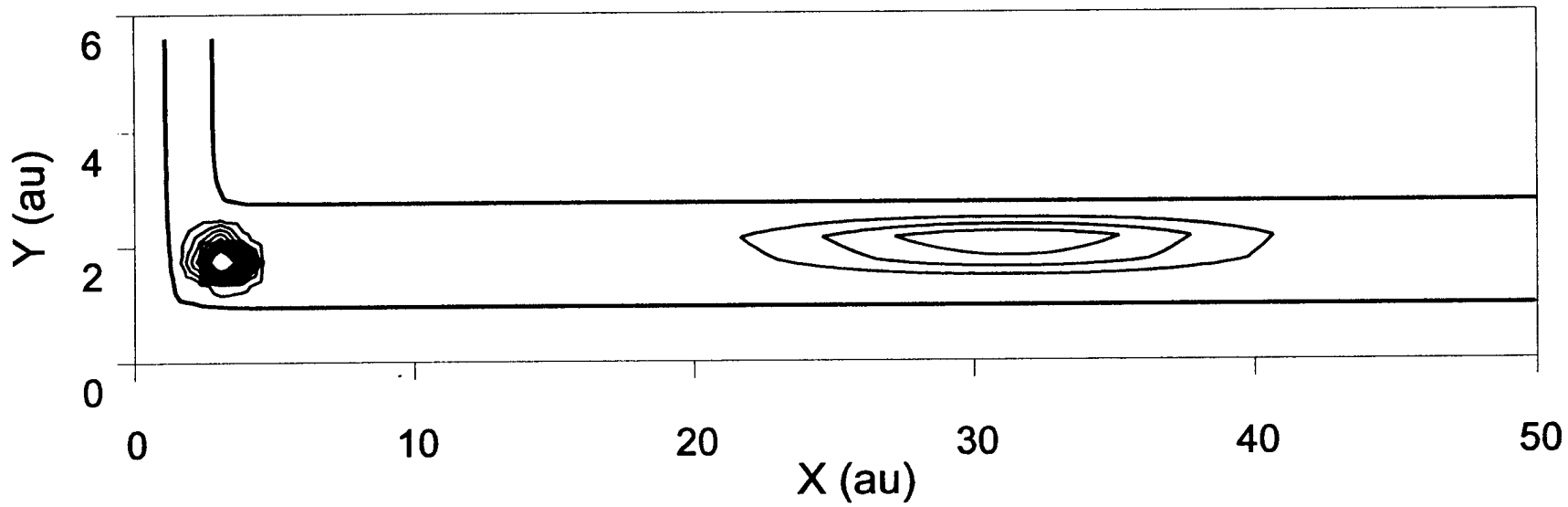

Figure 4.2 Contour plot of the absolute value of the initial wave packet $\langle X,Y|\Psi_{out}^{2,0}\rangle$ at t = 0 and t = +4000 au. The scale in the Y direction is increased by a factor of 2 for clarity. The two parallel contours mark the 0.1 au contour of the LSTH potential energy surface.

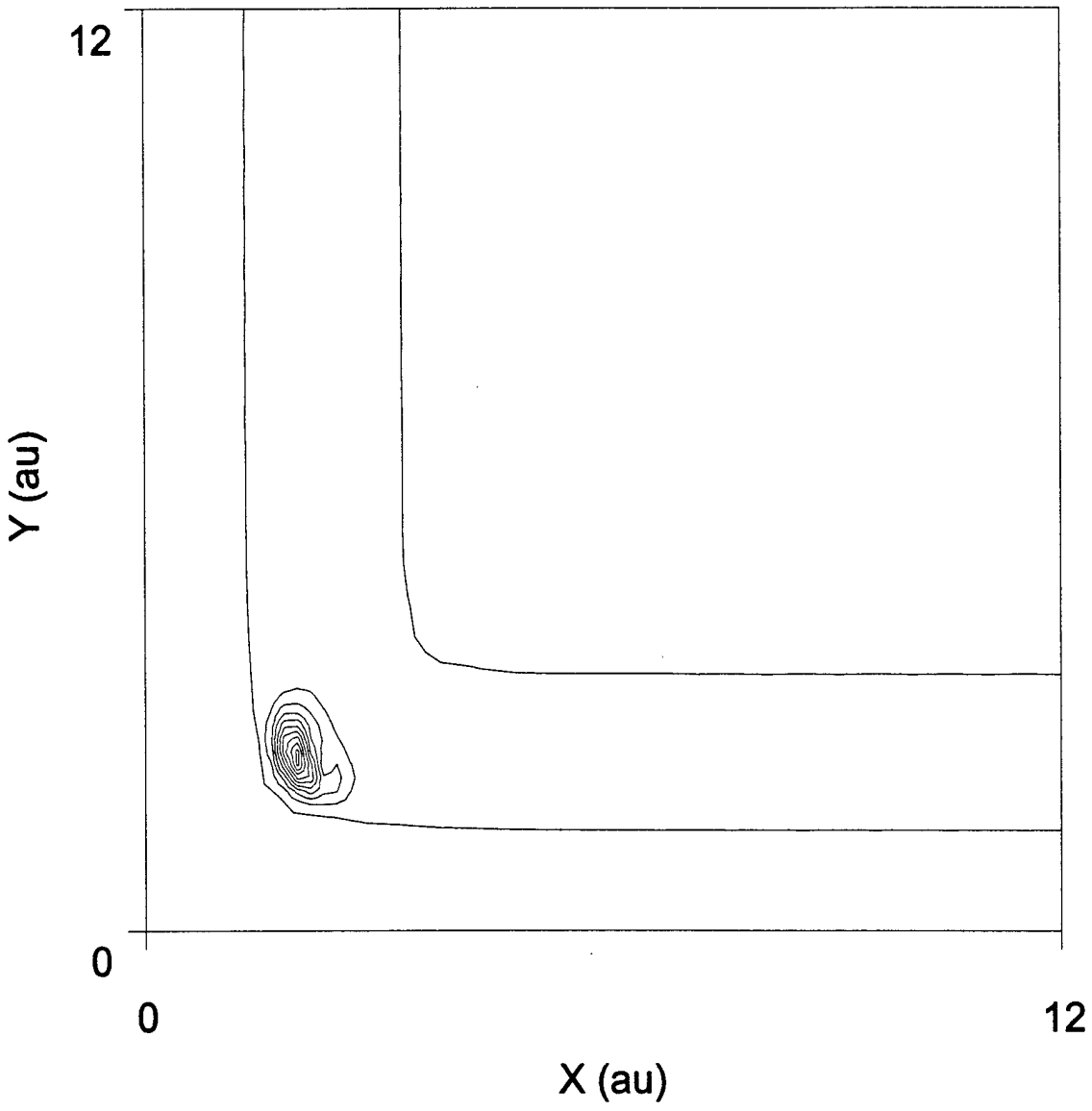

Figure 4.3 Contour plot of the absolute value of the Møller state $\langle X, Y|\Psi_+^{1,0}\rangle$ at $t = 0$. The two parallel contours mark the 0.1 au contour of the LSTH potential energy surface.

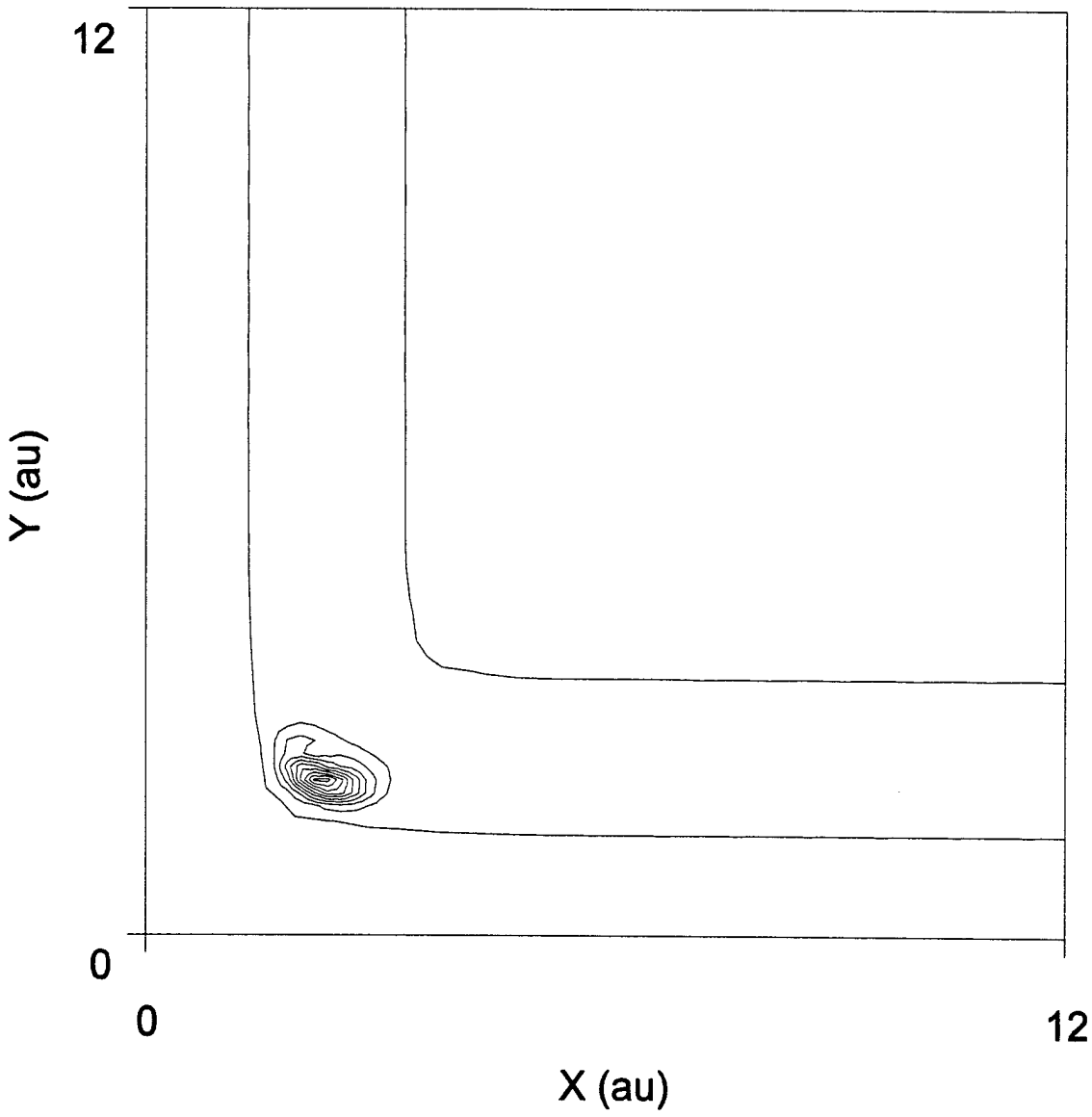

Figure 4.4 Contour plot of the absolute value of the Møller state $\langle X, Y|\Psi_{-}^{2,0}\rangle$ at $t = 0$. The two parallel contours mark the 0.1 au contour of the LSTH potential energy surface.

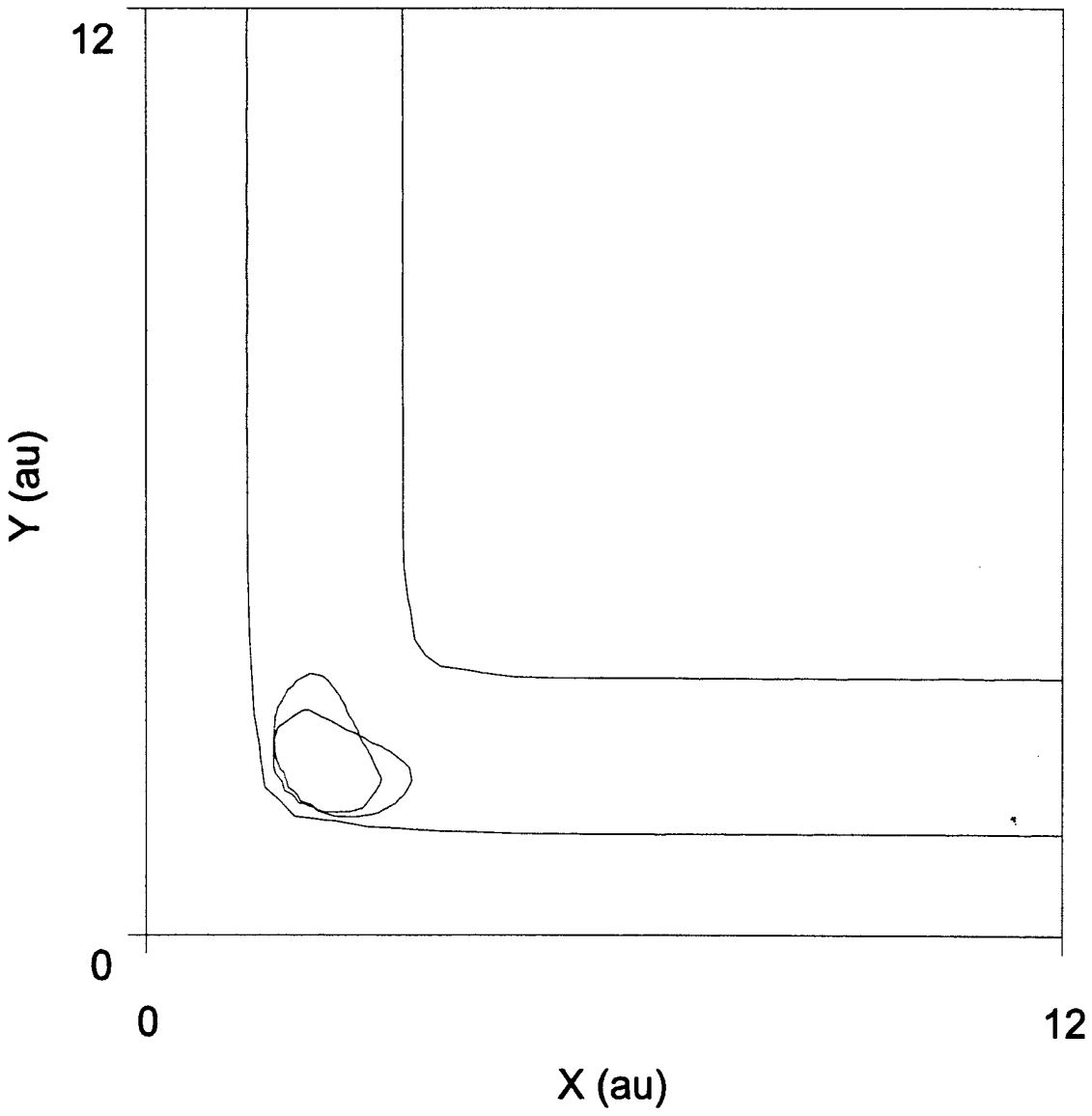

Figure 4.5 Contour plot of the placement of the absorbing boundary conditions with respect to the Møller states. The two closed contours are the 0.1 au contours of the Møller states. The two parallel contours are the 0.1 au contours of the LSTH potential energy surface. The saddle point is marked with a dot. The shaded region represents the area in which the absorbing boundary conditions are non-zero.

channel packet method in their analysis of the three dimensional $H + O_2$ reaction. In their analysis, Dai and Zhang selected a product Møller state located in the asymptotic limit. As a result, the absorbing boundary conditions are placed far from the interaction region of the potential. The idea behind this research is to use the smallest possible grid in order to achieve the most efficient use of computational resources. Any grid must contain the interaction region where the physics occurs. A small grid must somehow eliminate the asymptotic regions while simultaneously supporting the evolving wave packet until the interaction is complete. A product Møller state that lies in the asymptotic region far from the interaction region leads to the use of a large grid which defeats the purpose. Our approach differs in that we localize both the reactant and product Møller states in the interaction region. Thus there is no need to support the far regions of the asymptotic limit, where Dai and Zhang's product Møller state is placed, leading to the use of a smaller, more efficient grid.

4.2 Computational Procedure

The initial wave packets are constructed from a linear combination of eigenstates of the relative Hamiltonian $\hat{H}_{rel}$, given by Equation 2.21 and a single eigenstate of the internal Hamiltonian $\hat{H}_{int}$. The parameters *deltax1, deltax2*, and *deltat* are all chosen according to Kosloff's paper[58] and discussed in more detail in Section 3.1.1. The choice of *xmin1* and *xmin2* is based on the behavior of the LSTH potential near zero. Near zero, the LSTH potential flattens out at a value of 5 au and *xmin1* and *xmin2* are chosen so that the potential at (*xmin1,xmin2*) is just at 5 au. Since the time necessary to fully compute the correlation function is greatly affected by the grid size, compact Møller states are necessary in order to use small grids. In the one dimensional case, the final form of the Møller state was heavily influenced by the parameters *ioff, imom* and *sprd.* Likewise, the final form of the reactant Møller state in channel 1 is heavily influence by *ioff1, imom1* and *sprd1.*

Following the results of the one dimensional square well case, the initial choice for *ioff1* was made to center the initial wave packet over the interaction region with a wave packet spread, *sprd1*, such that the initial wave packet did not extend past the edge of the interaction region. The choice of the momentum offset, *imom1*, was based on the requirement that the initial wave packet have no negative momentum in the relative coordinate. The reactant Møller state was computed based on these choices. However, this turned out to not be the optimal choice for two reasons. In order to accommodate the spread of the wave packet on the spatial grid as the packet is propagated back in time, a long narrow grid is the most efficient one to use. The spread along with the long narrow grid is illustrated in Figure 4.2. In centering the initial wave packet in the interaction region, the resulting Møller state at $t = 0$ has bifurcated into both channels and the initial, long, narrow grid would have to be widened to accommodate the bifurcation. Instead, the parameter *ioff1* is set so that the initial wave packet is slightly offset into the reactant channel. The resulting Møller state is well localized in the interaction region as illustrated in Figure 4.3. The parameters for the reactant Møller state calculation are shown in Table 4.1. The $H + H_2$ potential energy surface has a barrier and no well so the total energy contains only the maximum relative kinetic energy and internal vibrational eigenstate energy.

To obtain eigenstates of the internal Hamiltonian, $\hat{H}_{int}$ is represented in a basis of Morse oscillator eigenstates and that matrix representation is diagonalized. The transformation matrix that diagonalizes $\hat{H}_{int}$ contains the linear combination of Morse oscillator eigenstates required to compute the eigenstates of $\hat{H}_{int}$. In the collinear $H + H_2$ reaction, the Møller state calculations are most efficiently computed on long, rectangular grids as illustrated in Figure 4.2. The initial wave packet is shown at $t = 0$ with the intermediate state at $t = -4000$ au. The intermediate state is obtained by analytically propagating the initial state from $t = 0$ to $t = -4000$ au using Jacobi coordinates. The propagation spreads the initial wave packet in the relative coordinate r according to Equation 2.34 and develops a phase factor in the

Table 4.1 Initial Møller state calculation parameters for the $H + H_2$ reactant channel.

Parameter	Value (au)	Notes
xmin1	1×10^{-7}	minimum X grid boundary
xmin2	1×10^{-7}	minimum Y grid boundary
ma	1837.1526025	mass of hydrogen atom a
mb	1837.1526025	mass of hydrogen atom b
mc	1837.1526025	mass of hydrogen atom c
deltax1	0.2	X grid resolution
deltax2	0.2	Y grid resolution
nstep	4000	number of time steps
sftcnt	4000	number of time steps to stop the propagation at
deltat	1.0	time step
ioff1	1.40105	initial X offset
ioff2	0.0	initial Y offset
imom1	-1.3	initial P_X offset
imom2	0.0	initial P_Y offset
sprd1	0.4	initial relative wave packet spread in the X direction
sprd2	0.0	initial relative wave packet spread in the Y direction
tau1	-4000.0	temporal offset for channel 1 initial wave packet
tau2	0.0	temporal offset for channel 2 initial wave packet
evch	1	asymptotic eigenstate number

internal coordinate R according to Equation 2.33. The intermediate wave packet is then transformed to bond coordinates and the final Møller state is computed by propagating back to $t = 0$ under the full scattering Hamiltonian $\hat{H}$. This propagation is done numerically using the split-operator method discussed in Section 2.6, using a modified version of the code first developed by Weeks and Tannor.[25] Figures 4.3 and 4.4 show the Møller states $\langle X, Y|\Psi_{+}^{1,0}\rangle$ and $\langle X, Y|\Psi_{-}^{2,0}\rangle$ respectively. Note that the Møller states are well localized in the interaction region. This permits the absorbing boundary conditions to be placed close to the interaction region and still have the spatial extent to fully attenuate the evolving Møller state during the correlation function computation. The placement of the absorbing boundary conditions with the LSTH potential energy surface and the Møller states is shown in Figure 4.5. The absorbing boundary conditions in two dimensions take a form similar to those in one dimension given by Equation 2.42. For the collinear $H + H_2$ reaction, the absorbing boundary conditions are given by

$$V_a(X,Y) = \left\{ \begin{array}{l} \pm h(X_0)\, Ai \exp\left\{\frac{(X-X_0)^2}{B}\right\}, X > Y \\ \pm h(Y_0)\, Ai \exp\left\{\frac{(Y-Y_0)^2}{B}\right\}, X < Y \end{array} \right\}, \tag{4.1}$$

where $h(\xi)$ is the heavyside step function given in Equation 2.43, X_0 and Y_0 are where the absorbing boundary conditions begin in channel 1 and channel 2, respectively, and A and B govern the shape of the absorbing boundary conditions. For the collinear $H + H_2$ reaction, the parameters $A = 1 \times 10^{-5}$ and $B = 2$ were chosen so that the evolving Møller state was completely attenuated before reflecting from the grid edges with a minimum of reflection. The offsets X_0 and Y_0 were chosen to be 6.2 so that the absorbing boundary conditions begin just beyond where the Møller states reached numeric zero.

In Weeks and Tannor's original calculation,[25] the grid size was 256 points by 256 points in order for the correlation function to reach zero before the evolving Møller state reached the edge of the grid and reflected. The reactant and product

Møller states are well localized inside a grid of 32 by 32 points. An initial grid of 64 by 64 points was used to apply the combination of absorbing boundary conditions and the channel packet method to the computation of the correlation function. The choice of 64×64 was partly arbitrary and partly due to the FFT being most efficient for N a power of 2.

4.3 Results

In order to compute S–matrix elements for the $\nu = 0 \rightarrow \nu' = 0, 1$ reactions, the Møller state $|\Psi_+^\gamma\rangle$ is computed using the $\nu = 0$ internal vibrational eigenstate and two Møller states $|\Psi_-^{\gamma'}\rangle$ are computed using the $\nu' = 0, 1$ internal vibrational eigenstates.[25] At $t = 0$, the reactant and product Møller states are localized in the interaction region of the potential and the absorbing boundary conditions are located as shown in Figure 4.5. In this computation, the reactant Møller state is chosen to evolve in time to both $t = -\tau$ and $t = +\tau$. As the reactant Møller state evolves backward in time, it retraces its path along channel 1. However, as it reaches the region containing the absorbing boundary conditions, it is steadily attenuated before it reaches the edge of the smaller grid. While there is some reflection, it is minimized by the choice of the absorbing boundary conditions. Likewise, as the reactant Møller state evolves forward in time, it bifurcates into both channels. Again, as it reaches the regions containing the absorbing boundary conditions, it is attenuated with a minimum of reflection and does not reach the grid edges as illustrated in Figure 4.6. As the reactant Møller state evolves from $-\tau$ to τ, its correlation $C_{\gamma'\gamma}(t)$ with the product Møller state is calculated. Correlation functions for the $\nu = 0$ to $\nu' = 0$ and $\nu = 0$ to $\nu' = 1$ reactions are shown in Figures 4.7 and 4.8. The correlation function $C_{\gamma'\gamma}(t)$ is then used to compute S–matrix elements, $S^{\gamma'\gamma}_{k'_{\gamma'}k_\gamma}$, according to Equation 2.30. Figures 4.9 and 4.10 show the probability of transmission for two reactions $H + H_2(\nu = 0) \rightarrow H_2(\nu' = 0, 1) + H$.and are in agreement with previous calculations.[25,31–35,39] In order to quantify the error in the new method compared

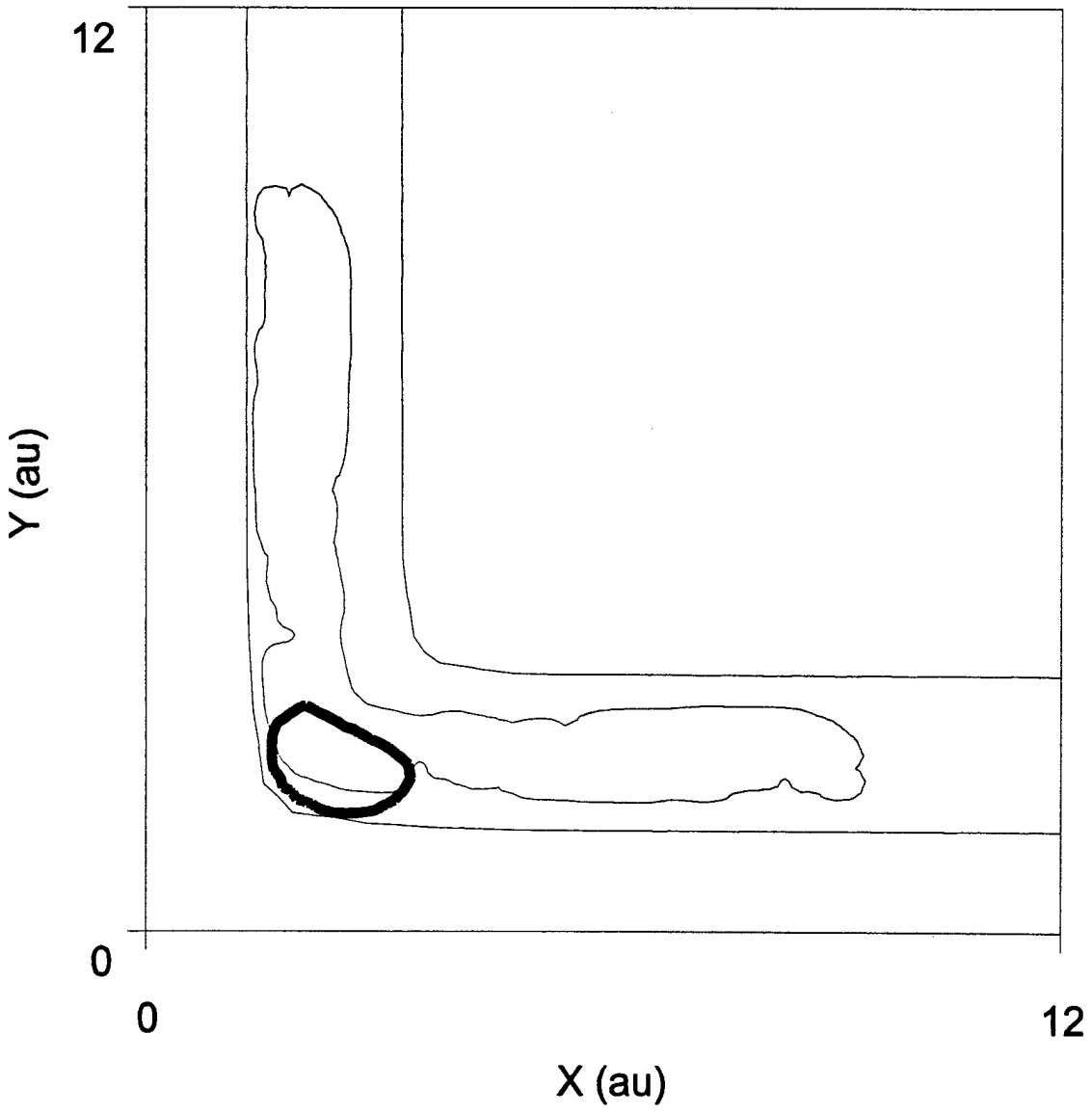

Figure 4.6 Contour plot of the time evolution of the Møller state $|\Psi_+^{1,0}\rangle$ at $t = +1000$ au. The closed contours are the 0.1 au contours of $|\langle X, Y|\Psi_+^{1,0}\rangle|$. The thick closed contour is the 0.1 au contour of the non-evolving Møller state $|\langle X, Y|\Psi_-^{2,0}\rangle|$. The two parallel contours are the 0.1 au contours of the LSTH potential energy surface. The shaded region represents the area in which the absorbing boundary conditions are non-zero.

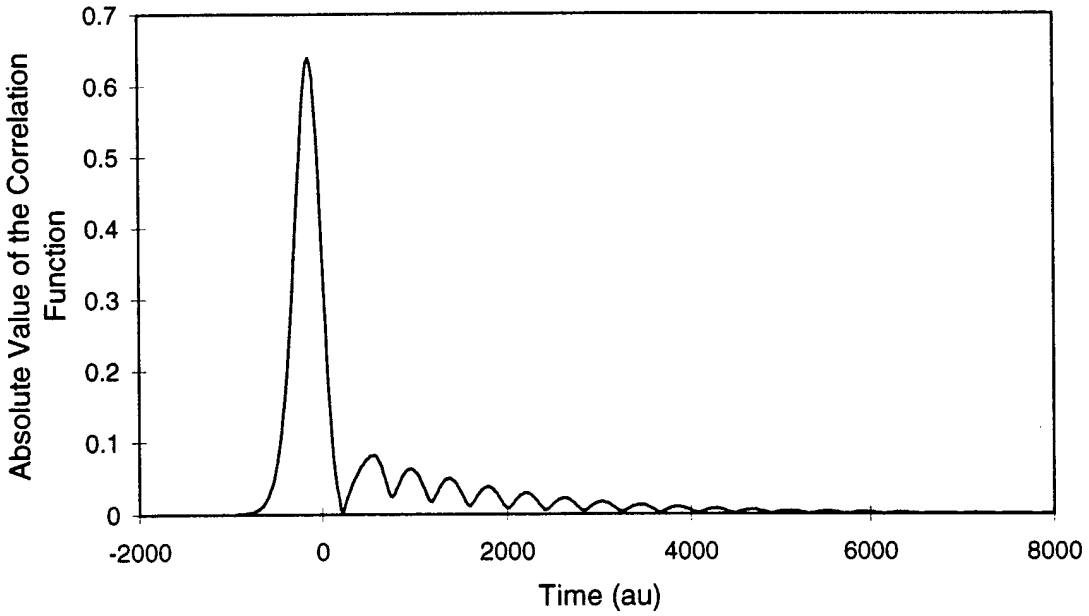

Figure 4.7 Absolute value of the correlation function calculated using the channel packet method with absorbing boundary conditions for $H + H_2(v = 0) \rightarrow H_2(v' = 0) + H$.

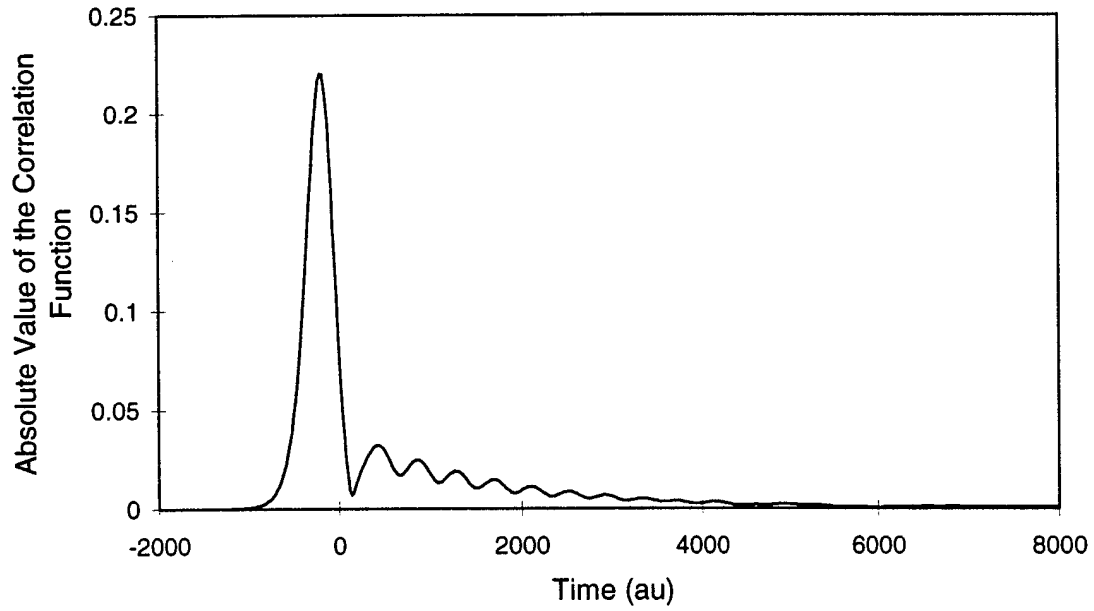

Figure 4.8 Absolute value of the correlation function calculated using the channel packet method with absorbing boundary conditions for $H + H_2(v = 0) \rightarrow H_2(v' = 1) + H$.

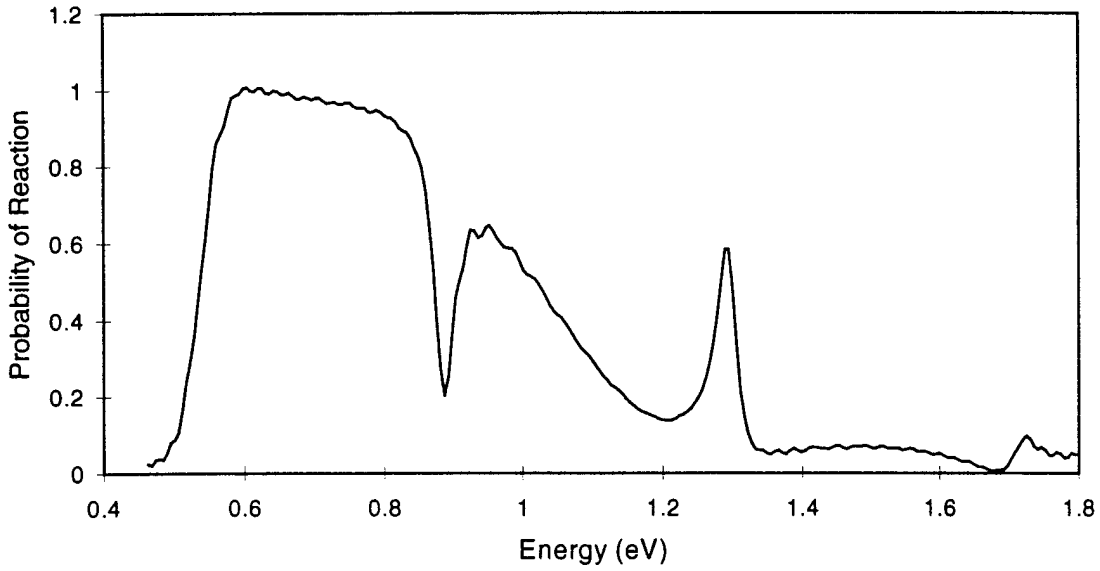

Figure 4.9 Probability of reaction calculated using the channel packet method with absorbing boundary conditions for $H + H_2(v = 0) \rightarrow H_2(v' = 0) + H$.

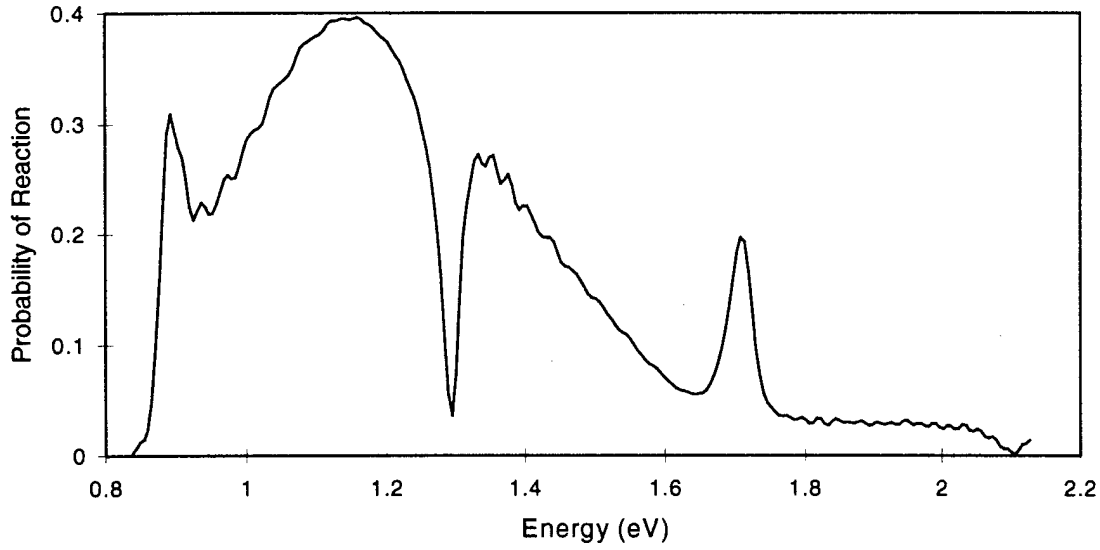

Figure 4.10 Probability of reaction calculated using the channel packet method with absorbing boundary conditions for $H + H_2(v = 0) \rightarrow H_2(v' = 1) + H$.

to previous work, the work of Weeks and Tannor[25] was used as a benchmark and the L_1 norm was computed using

$$L_1 = \frac{1}{N} \sum \frac{|P_{Weeks} - P_{abc}|}{P_{Weeks}}, \tag{4.2}$$

where N is the number of probabilities of reaction computed, p_{Weeks} is the work of Weeks and Tannor[25] and p_{abc} is the computation performed using absorbing boundary conditions. The L_1 norm error was 6.3×10^{-3} which is at the third digit convergence test used in Chapter III and the calculation is considered to have converged to the correct solution.

Using absorbing boundary conditions, the correlation functions used to compute S-matrix elements shown in Figures 4.9 and 4.10 are computed using a 64×64 grid compared with a 256×256 grid required to compute the correlation function without absorbing boundary conditions.[25] The calculation of $C_{\gamma'\gamma}$ without absorbing boundary conditions took $\sim 31,000$ seconds of CPU time on a MIPS R3000 Silicon Graphics workstation and on the same computer the calculation with absorbing boundary conditions took ~ 2500 seconds of CPU time. Similarly, on a MIPS R10000 Silicon Graphics workstation, the calculation without absorbing boundary conditions took ~ 1450 seconds of CPU time and the calculation with absorbing boundary conditions took ~ 80 seconds. Thus, an order of magnitude improvement in the calculation time is obtained when using absorbing boundary conditions with the channel packet method to compute the correlation function for the $H + H_2$ reaction. Similar to Chapter III, an estimate of the savings can be computed from the computational scaling of the FFTs used in the calculation. For a grid of $N_1 \times N_2$ points, the FFT scales as $(N_1 \times N_2) \log_2 (N_1 \times N_2)$. In the special case where $N_1 = N_2$, this reduces to $2 \times N^2 \log_2 N$. Reducing the grid from 256×256 to 64×64 leads to an estimated cost savings of 21. The actual savings was 18 with the difference due to the fact that not all the computational effort is in the FFTs.

4.4 Convergence testing

Similar to the one dimensional case, the channel packet method in two dimensions is tested against two criteria for convergence. The first test is convergence to the correct answer and the second is the efficiency, or order, of convergence. Convergence to the correct answer is is necessary as a method which converges, but not to the correct answer, is of little use. Figure 4.11 illustrates the channel packet method with absorbing boundary conditions converging towards the correct answer for the reaction $H + H_2(\nu = 0) \rightarrow H_2(\nu' = 0) + H$. The data set labels in Figure 4.11 do not reflect the values of any one parameter. Between each of the data sets, Δx_1, Δx_2, N and Δt may have changed. The line labeled "10" in Figure 4.11 illustrates the result when the guidance for grid selection in Section 3.1.1 is violated. In this case, the temporal grid was too coarse to properly support the wave packet. As in Section 3.1.4, the L_1 norm defined in Equation 3.16 is used to judge the convergence towards the correct solution. The data sets labeled "1" and "2" have in fact converged to the correct solution such that the L_1 norm has converged to 3 digits.

The second test of convergence, the efficiency or order, was outlined in Section 3.1.4. In the two dimensional case, only the parameter Δt can be isolated and tested due to the nature of the $H + H_2$ collinear reaction. The symmetric potential energy surface and the two reaction channels require equal spatial grid parameters. Unequal spatial grid parameters in the Møller state calculation requires interpolation between grid points for one or both Møller states in the correlation function calculation. The order of convergence for the two dimensional channel packet method is 4 as is illustrated in Figure 4.12. This is the same as in the one dimensional case. The dramatic rise in the relative error in Figure 4.12 for values of $\Delta t > 1.0$ au is due to temporal grid that is too coarse to support the wave packet.

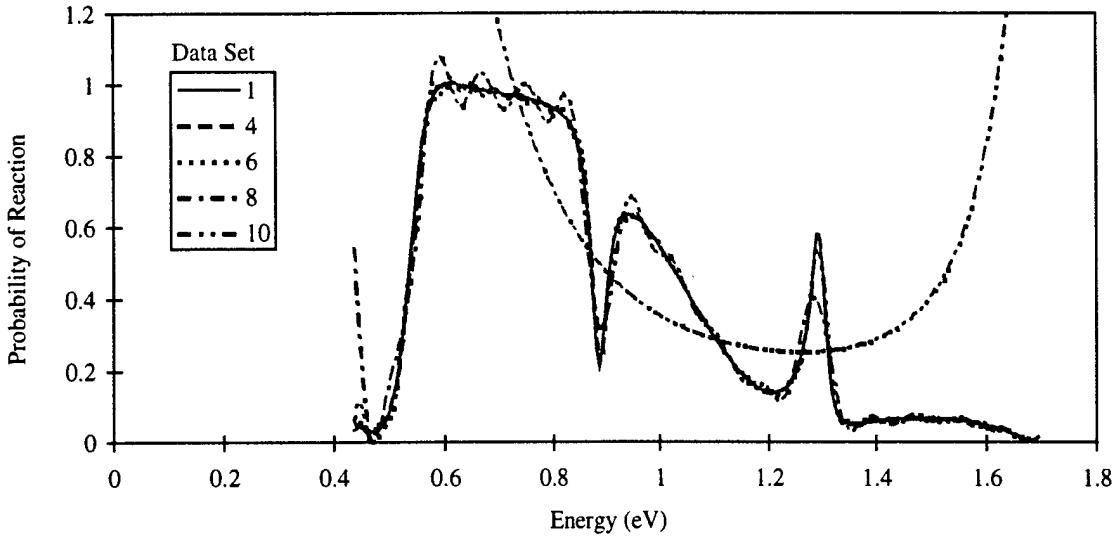

Figure 4.11 Convergence of the probability of reaction using the channel packet method with absorbing boundary conditions towards the correct answer for the reaction $H + H_2(v = 0) \rightarrow H_2(v' = 0) + H$.

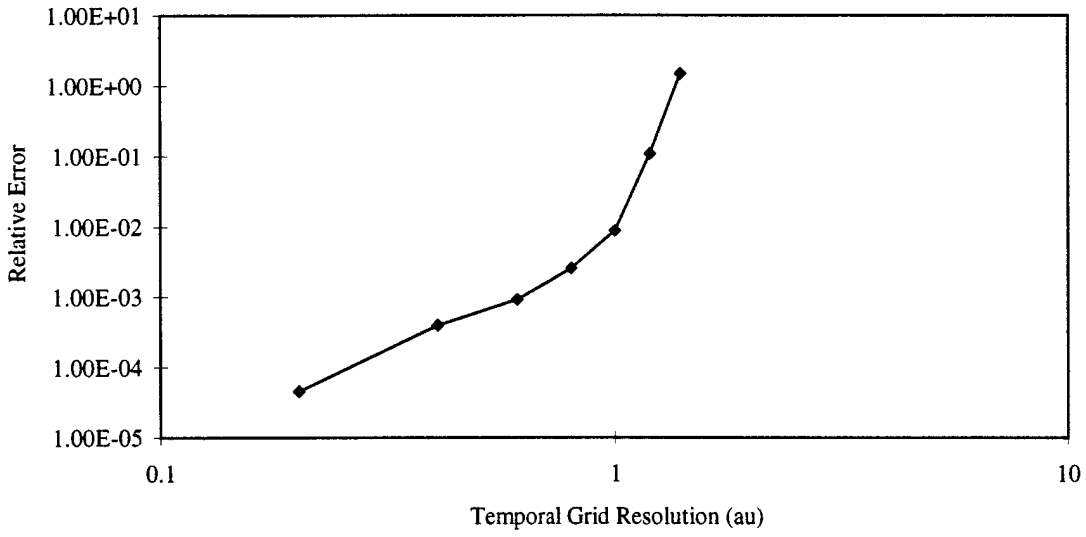

Figure 4.12 Relative error vs. Temporal grid resolution for the probability of reaction for the reaction $H + H_2(v = 0) \rightarrow H_2(v' = 0) + H$.

4.5 Summary

The two dimensional $H + H_2$ system has been extensively studied and S–matrix elements have been calculated using a wide variety of methods[17,25,31-35,39] and provides an excellent benchmark for testing the combination of the channel packet method with absorbing boundary conditions. The results are in agreement with previous calculations[25,31-35,39] with the L_1 norm error between the channel packet method and the channel packet method with absorbing boundary conditions is on the order of 6×10^{-3}. This is a small error in comparison to the dramatic reduction in computational effort the combination of the channel packet method with absorbing boundary conditions produces. The grid for computing the correlation function was reduced by a factor of 16, from 256×256 to 64×64. Overall, the result of the grid reduction was an order of magnitude improvement in the time necessary to compute the correlation function.[41]

V. *Two dimensional reactive quantum scattering for a model system of two coupled Morse oscillators*

A simple model system of two coupled Morse oscillators is proposed to investigate the combination of the channel packet method with absorbing boundary conditions in systems with a well in the interaction region. In this chapter, three mass configurations are investigated: light-light-light (LLL), medium-light-medium (MLM) and heavy-light-heavy (HLH). The light-heavy-light (LHL) mass configuration is treated in the next chapter. The mass configurations label the masses of the collinear atoms in the reaction from left to right. For example, HLH labels atom A as heavy, B as light and C as heavy in the reaction $A + BC\,(\nu) \rightarrow AB\,(\nu') + C$.

5.1 Two coupled Morse oscillator potential

The equation for the potential energy surface of two coupled Morse oscillators is simply

$$V(X,Y) = D_e\left\{1 - \exp\left[-\alpha(X - r_e)\right]\right\}^2 + D_e\left\{1 - \exp\left[-\alpha(Y - r_e)\right]\right\}^2 - D_e, \quad (5.1)$$

where D_e is the dissociation energy, α is related to the anharmonicity and r_e is the diatomic equilibrium separation. The dissociation energy is subtracted from the potential energy surface so that in the asymptotic limit at the equilibrium position the potential energy surface is equal to zero. The parameters governing the potential energy surface are completely variable in this model. For the reactions in this chapter, a single potential energy surface was constructed having a dissociation energy of $D_e = 0.1$ au $= 2.72$ eV, an equilibrium separation of $r_e = 0.7$ au, and the anharmonicity, $\alpha = 5$, such that the asymptotic limit could be reached while remaining on a 256×256 grid. These choices are governed by the fact that in order to reach the asymptotic limit, the value of the AB Morse oscillator potential in the $A + BC$ channel has to be

numerically zero. However, there must still be room on the coordinate grid in that channel so that the evolving wave packets completely exit the interaction region, i.e. reach the asymptotic limit, without reflecting from the edge of the grid. For comparison, a model proton transfer system[61] has $D_e = 0.16$ au and the collinear $H + H_2$ reaction has $D_e = 0.17$ au. A contour plot of the model potential energy surface where $D_e = 0.1$ au and $\alpha = 5$ is shown in Figure 5.1. The well is 0.1 au below the bottom of the asymptotic limit of the troughs and 0.2 au below the plain representing the energetically inaccessible $A + B + C$ channel.

5.2 Mass configurations

Initially, three mass configurations were considered: LLL, MLM and HLH. The purpose was to investigate for the same potential energy surface the effect of the kinetic energy operator $\hat{T}$ on reactive quantum scattering. In bond coordinates, $\hat{T}$ is given by

$$\hat{T} = \frac{\hat{P}_X^2}{2\mu_{a,bc}} + \frac{\hat{P}_Y^2}{2\mu_{c,ab}} - \frac{\hat{P}_X \hat{P}_Y}{m_b}, \tag{5.2}$$

where $\hat{P}_X$ and $\hat{P}_Y$ are the conjugate momentum operators for the bond coordinates (X, Y) and the reduced masses $\mu_{a,bc}$ and $\mu_{c,ab}$ are given by

$$\mu_{j,kl} = \frac{m_j (m_k + m_l)}{m_j + m_k + m_l}. \tag{5.3}$$

Equation 5.2 illustrates that the kinetic energy operator is parameterized by the masses of the reacting particles. In this investigation, the masses were chosen to model the $H + H_2$ reaction for the LLL mass configuration. The MLM configuration was chosen to be slightly mass disparate compared to the non-mass disparate LLL configuration and the HLH configuration was chosen to have very disparate masses. The mass configurations are given in Table 5.1. The three configurations have different asymptotic limits in the number of internal vibrational eigenstates and energies due to the mass in the kinetic energy term in Equation 5.2. The eigenstates and

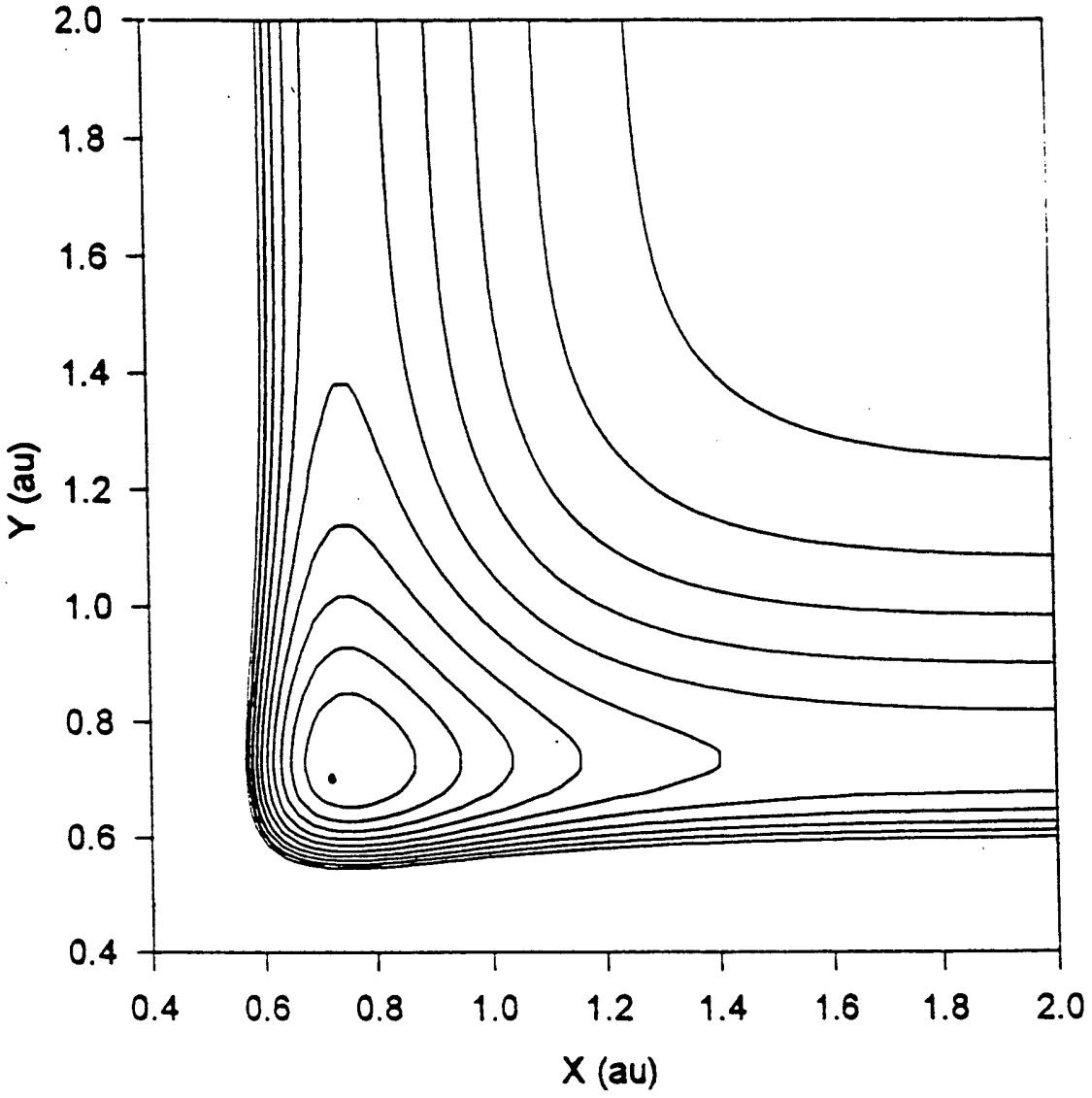

Figure 5.1 Contour plot for the model two coupled Morse oscillator potential energy surface. The contours range from –0.1 au to 0.1 au in steps of 0.04 au. The dot in the center of the well represents the lowest point on the potential energy surface.

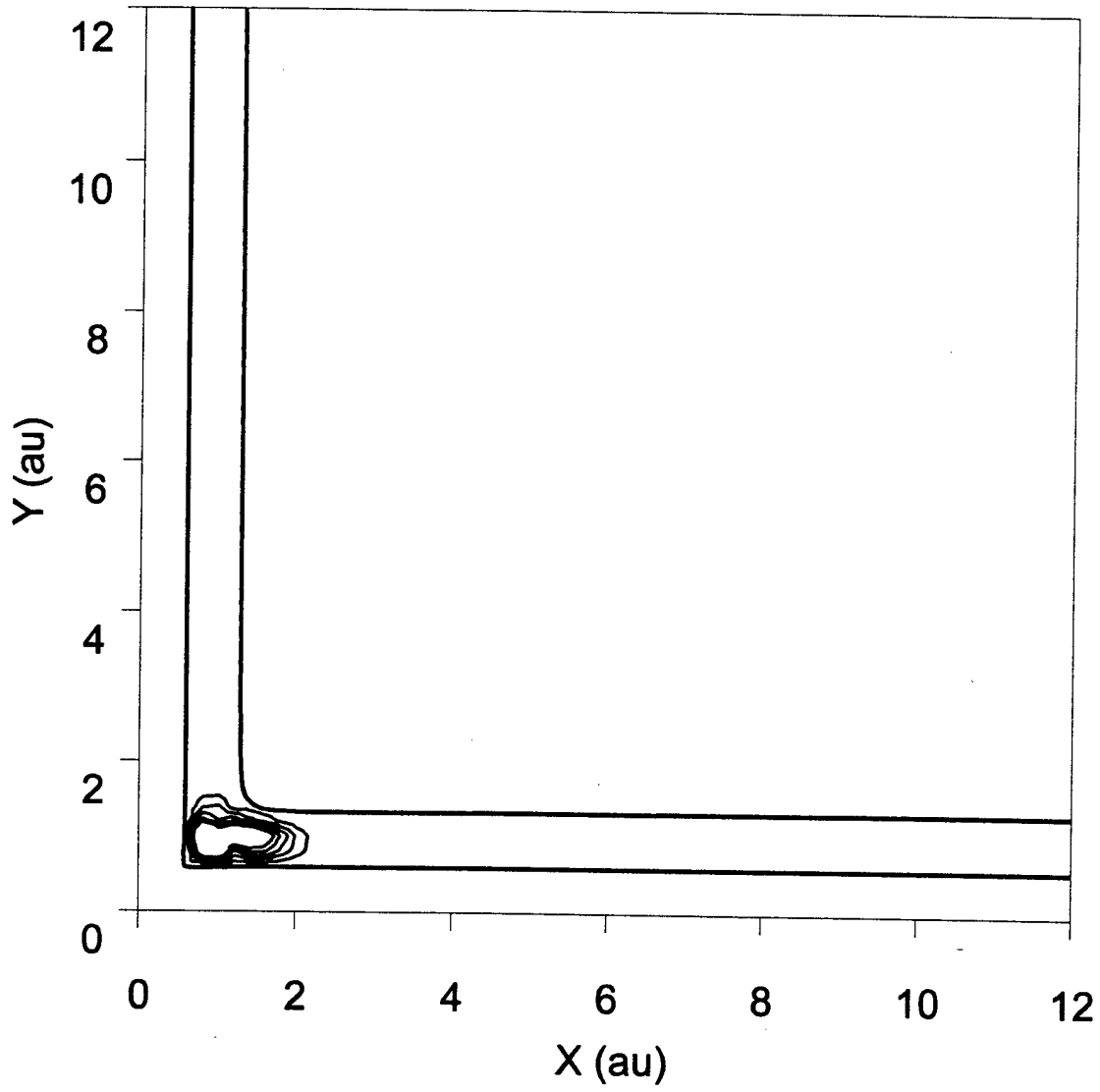

Figure 5.2 Reactant Møller state for the two coupled Morse oscillator LLL mass configuration. The two parallel contours are the 0.1 au contours of the two coupled Morse oscillator potential energy surface. The closed contours represent the absolute value of the Møller state $\langle X, Y|\Psi_+^{1,0}\rangle$.

plitude of $\langle X, Y|\Psi_+^{1,0}\rangle$ has exited the interaction region into the product channel. A small amount of reflection back into the reactant channel is also visible. The correlation function calculation, shown in Figure 5.5, rapidly approaches zero for negative times but not for positive times indicating the presence of a quasi-bound state in the interaction region.

The probability of reaction shown in Figure 5.6 exhibits an overall oscillation that is questionable in nature. Similar oscillations can be induced by terminating the computation of the correlation function prior to the correlation function reaching zero. However in Figure 5.5 it is clear that the correlation function has reached zero and the oscillation is not due to early termination of the correlation function computation. In an attempt to understand the oscillations in Figure 5.6, the correlation function was computed using a smaller grid where the absorbing boundary conditions have been placed closer to the interaction region. The correlation function for this calculation is shown in Figure 5.7. Figure 5.8 illustrates the probability of reaction for the LLL mass configuration computed from the correlation function shown in Figure 5.7. While the underlying shape of the curve has not changed, including the drop in the probability of reaction at 0.75 eV, the oscillations have changed in both frequency and amplitude. In order to determine if the feature at 0.75 eV is real or an artifact of the absorbing boundary condition reflection error, the correlation function, shown in Figure 5.9, for the LLL mass configuration was computed without using absorbing boundary conditions. The feature at 0.75 eV is

Table 5.2 The three lowest internal vibrational eigenstate energies for the two coupled Morse oscillator potential energy surface for the three mass configurations. Energies are in atomic units.

ν''	LLL	MLM	HLH
0	0.03223	0.02967	0.02551
1	0.07794	0.07339	0.06528
2	0.09865	0.09627	0.09006

Table 5.3 Initial Møller state calculation parameters for the LLL mass configuration.

Parameter	Value (au)	Notes
xmin1	0.2	minimum X grid boundary
xmin2	0.2	minimum Y grid boundary
ma	2000.0	mass of atom a
mb	2000.0	mass of atom b
mc	2000.0	mass of atom c
deltax1	0.05	X grid resolution
deltax2	0.05	Y grid resolution
nstep	800	number of time steps
sftcnt	800	number of time steps to stop the propagation at
deltat	1.0	time step
ioff1	1.4	initial X offset (0 for product wave packet)
ioff2	0.0	initial Y offset (1.4 for product wave packet)
imom1	-1.5	initial P_X offset (0 for product wave packet)
imom2	0.0	initial P_Y offset (-1.5 for product wave packet)
sprd1	0.3	initial relative wave packet spread in the X direction
sprd2	0.3	initial relative wave packet spread in the Y direction
tau1	-800.0	temporal offset for channel 1 initial wave packet
tau2	-800.0	temporal offset for channel 2 initial wave packet
evch	1	asymptotic eigenstate number

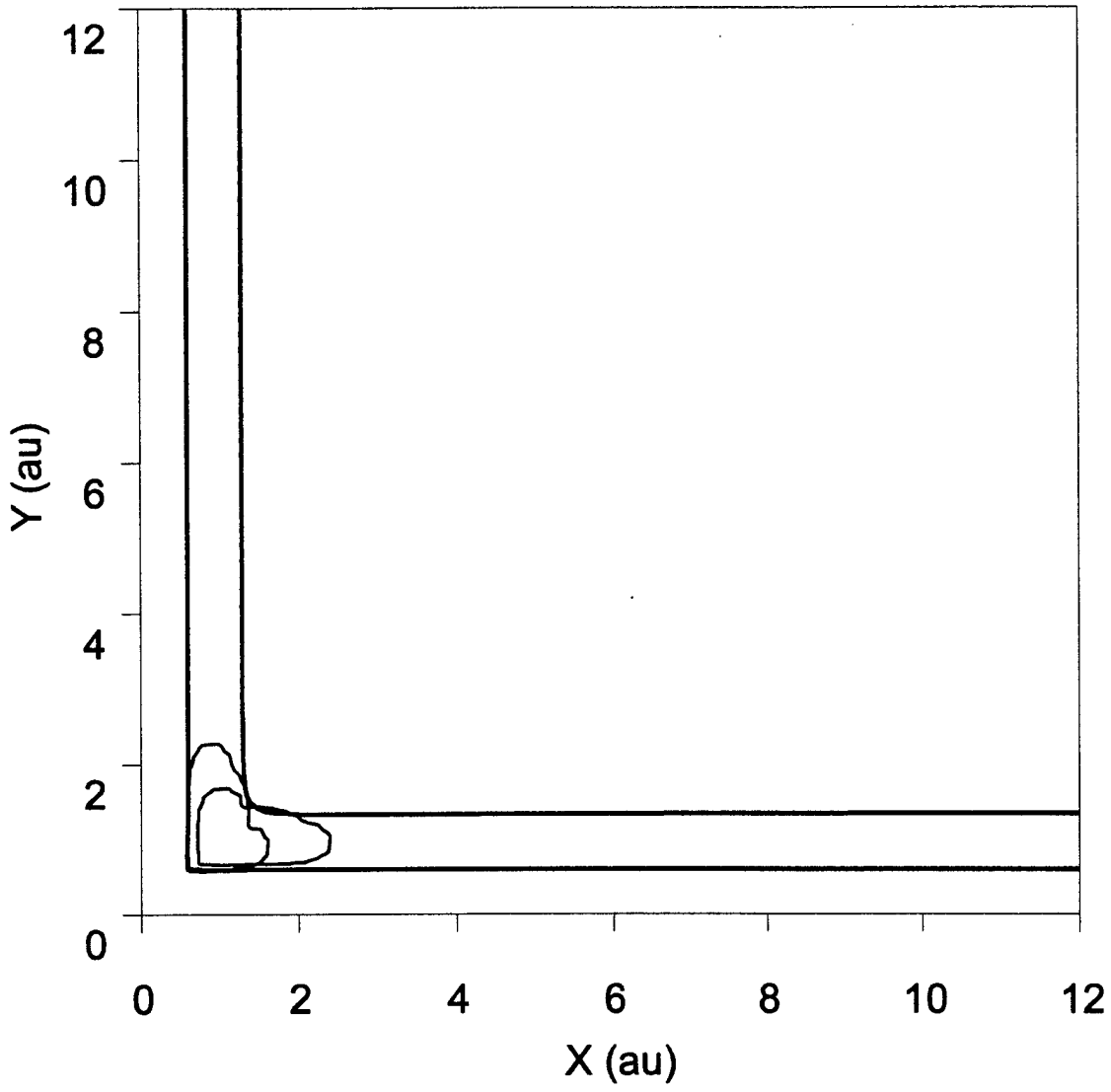

Figure 5.3 Compact Møller states and absorbing boundary condition placement for the two coupled Morse oscillator LLL mass configuration. The two parallel contours represent the 0.1 au contours of the potential energy surface. The dot represents the bottom of the well in the interaction region. The two closed contours are the 0.1 au contours of the absolute value of the Møller states. The shaded region represents the area in which the absorbing boundary conditions are non-zero.

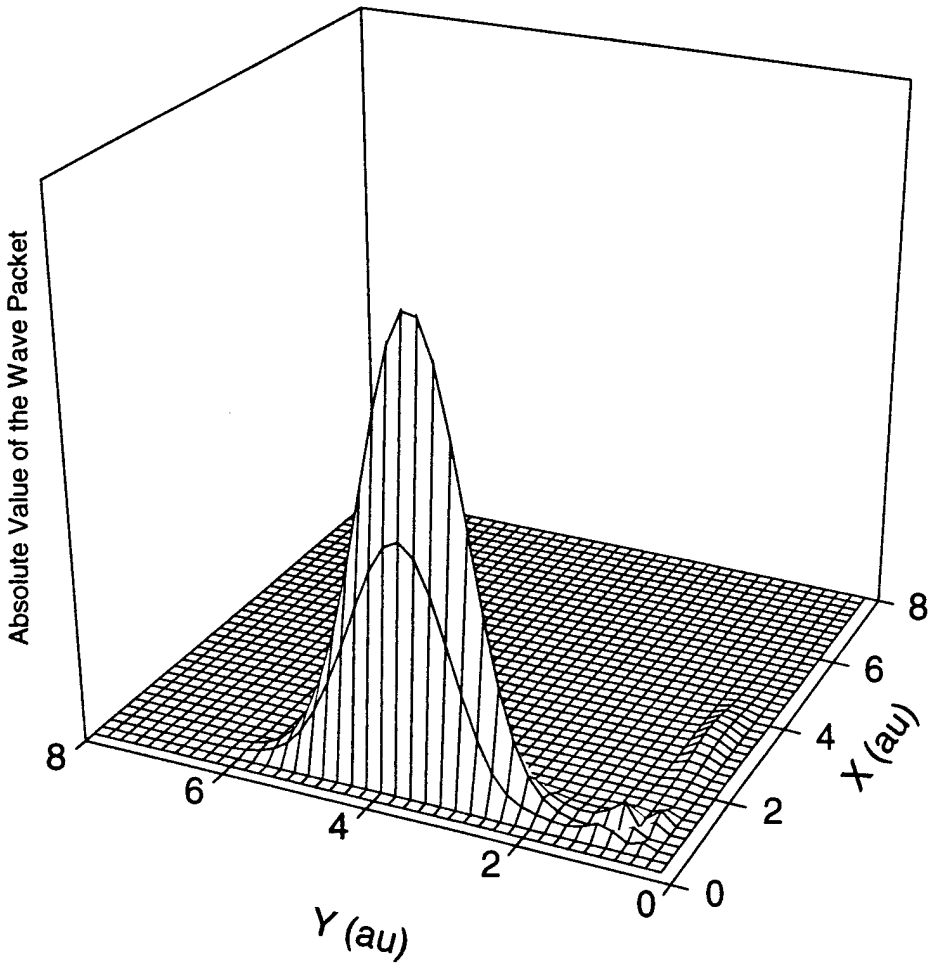

Figure 5.4 Surface plot of the absolute value of the evolving LLL reactant Møller state at $t = +800$ au. The reactant channel is parallel to the X direction and the product channel is parallel to the Y direction. Almost all the evolving Møller state has exited the interaction region in the product channel.

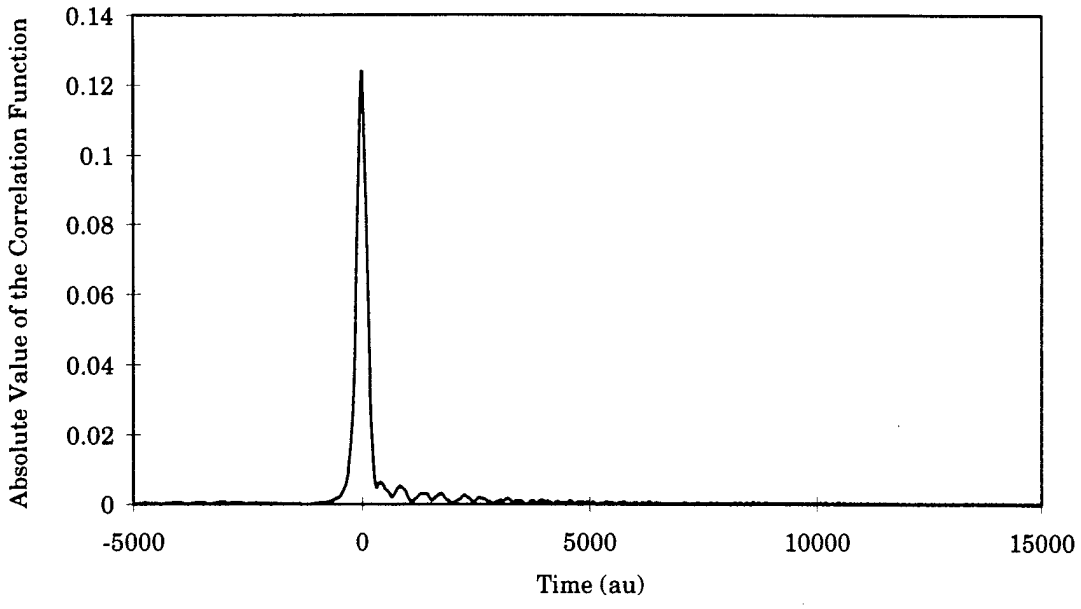

Figure 5.5 Absolute value of the correlation function for the two coupled Morse oscillator LLL mass configuration for the reaction $A + BC(v = 0) \rightarrow AB(v' = 0) + C$.

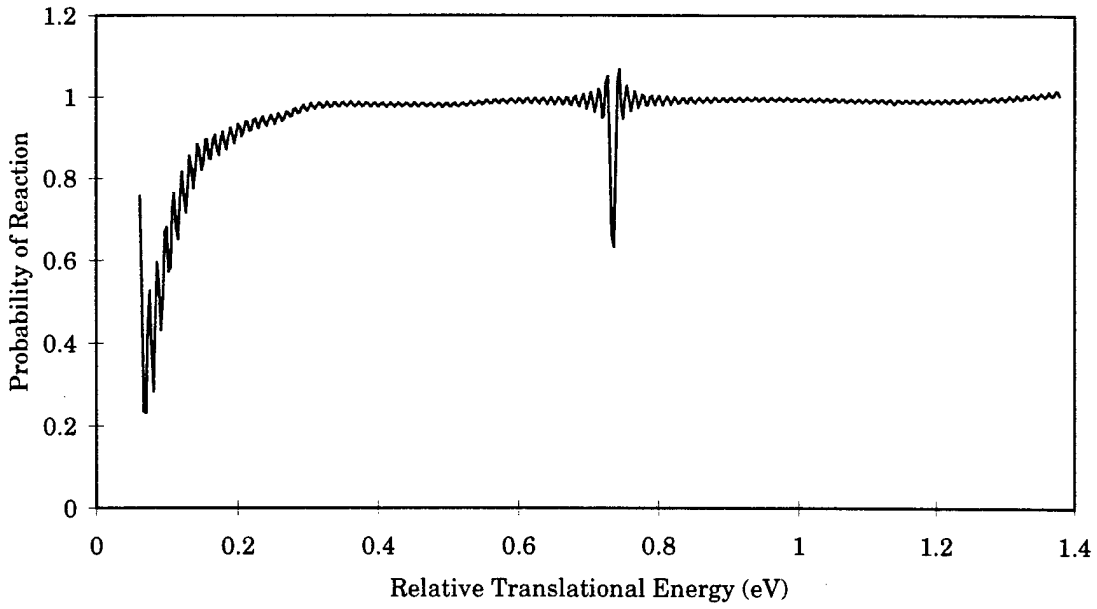

Figure 5.6 Probability of reaction for the two coupled Morse oscillator LLL mass configuration for the reaction $A + BC(v = 0) \rightarrow AB(v' = 0) + C$.

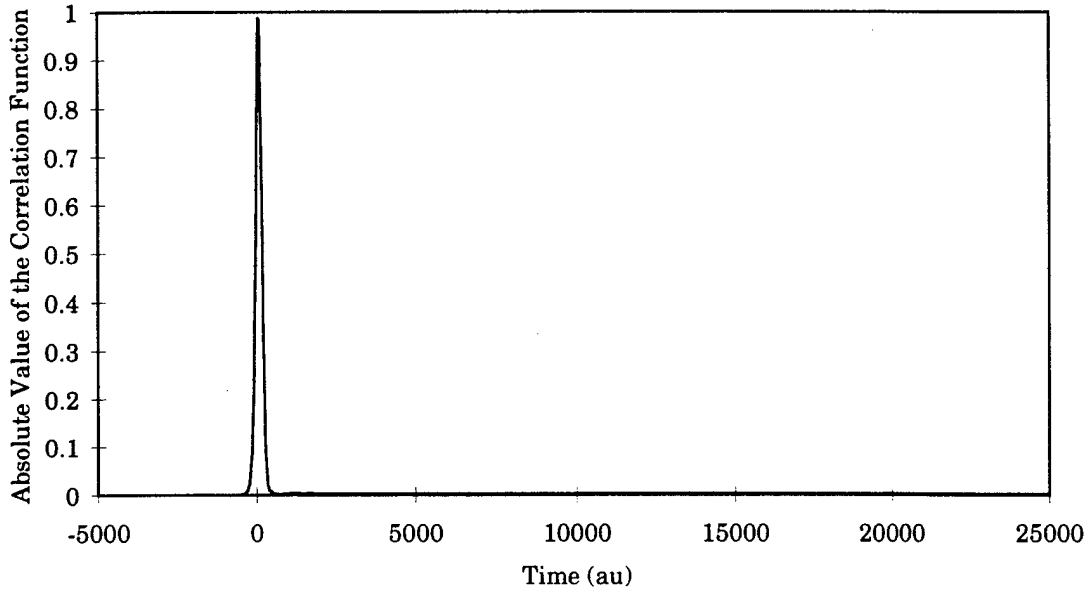

Figure 5.7 Absoute value of the correlation function for the two coupled Morse oscillator LLL mass configuration for the reaction $A + BC(v = 0) \rightarrow AB(v' = 0) + C$. In this calculation, the ABC have been moved closer to the interaction region and the grid size reduced.

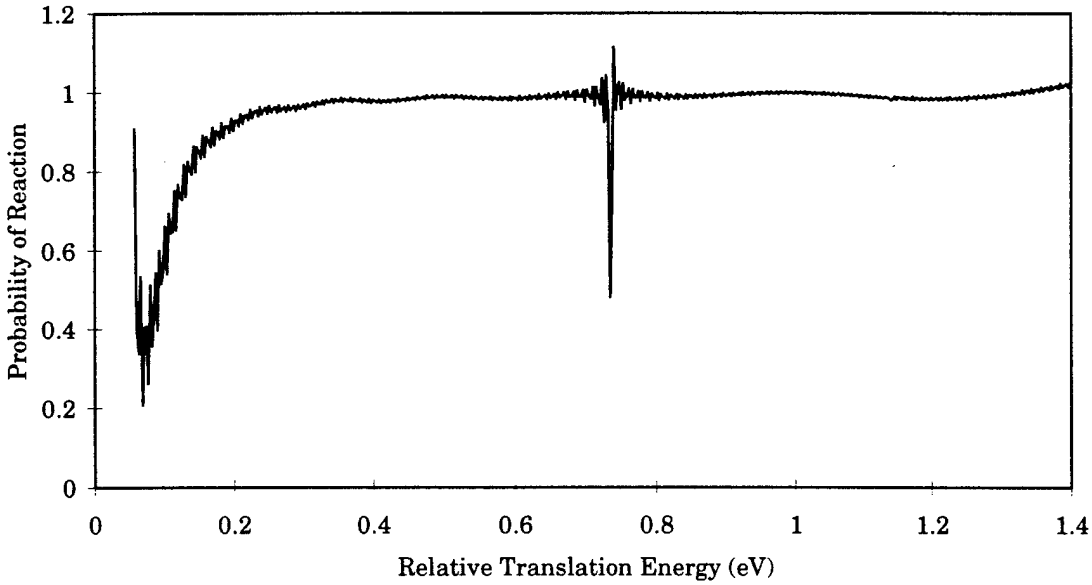

Figure 5.8 Probability of reaction for the two coupled Morse oscillator LLL mass configuration for the reaction $A + BC(v = 0) \rightarrow AB(v' = 0) + C$. In this calculation, the ABC have been moved closer to the interaction region and the grid size reduced.

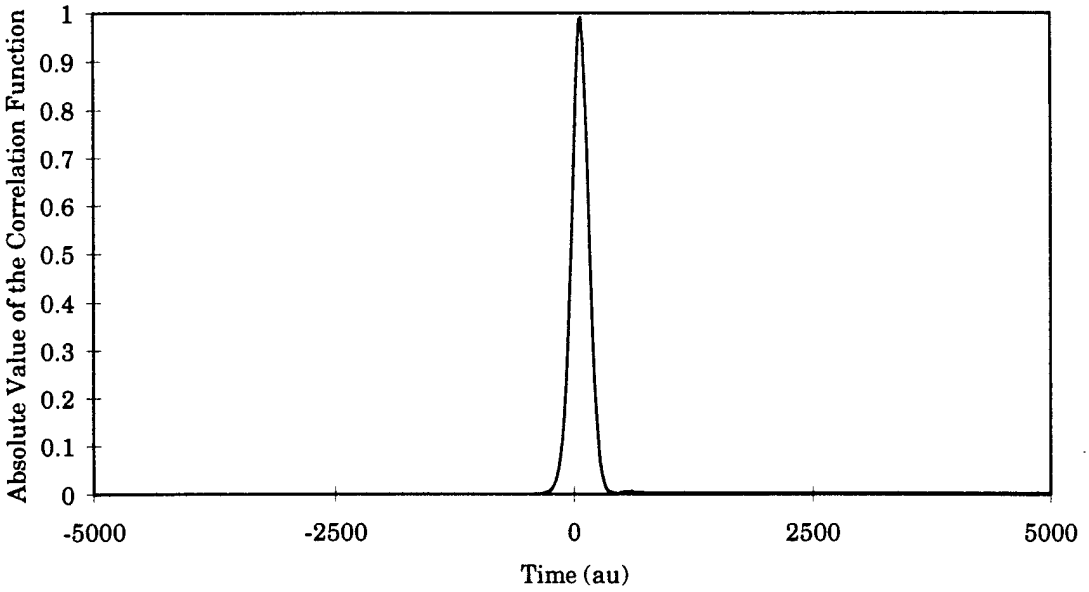

Figure 5.9 Absolute value of the correlation function for the two coupled Morse oscillator LLL mass configuration for the reaction $A + BC\,(\nu = 0) \rightarrow AB\,(\nu' = 0) + C$ where absorbing boundary conditions were not used.

clearly evident in the probability of reaction computed from the correlation function in Figure 5.9 and shown in Figure 5.10 and is likely to be real. In Figure 5.10, the probability of reaction at low energies and the overlying oscillations are due to prematurely terminating the computation of the correlation function in order to avoid edge of grid reflection.

5.2.3 MLM S-matrix elements. Figure 5.11 illustrates that the MLM Møller states are well localized in the interaction region. A surface plot of the evolving reactant Møller state, shown in Figure 5.12, illustrates how the evolving Møller state bifurcates into both channels. The correlation function, shown in Figure 5.13, rapidly approaches zero in both the negative and positive time directions. However, the probability of reaction shown in Figure 5.14 again exhibits an overlying oscillation as in the LLL mass configuration shown in Figure 5.6. In order to determine if the resonances were real or artifacts of absorbing boundary condition reflection error, the correlation function was computed using a new set of absorbing

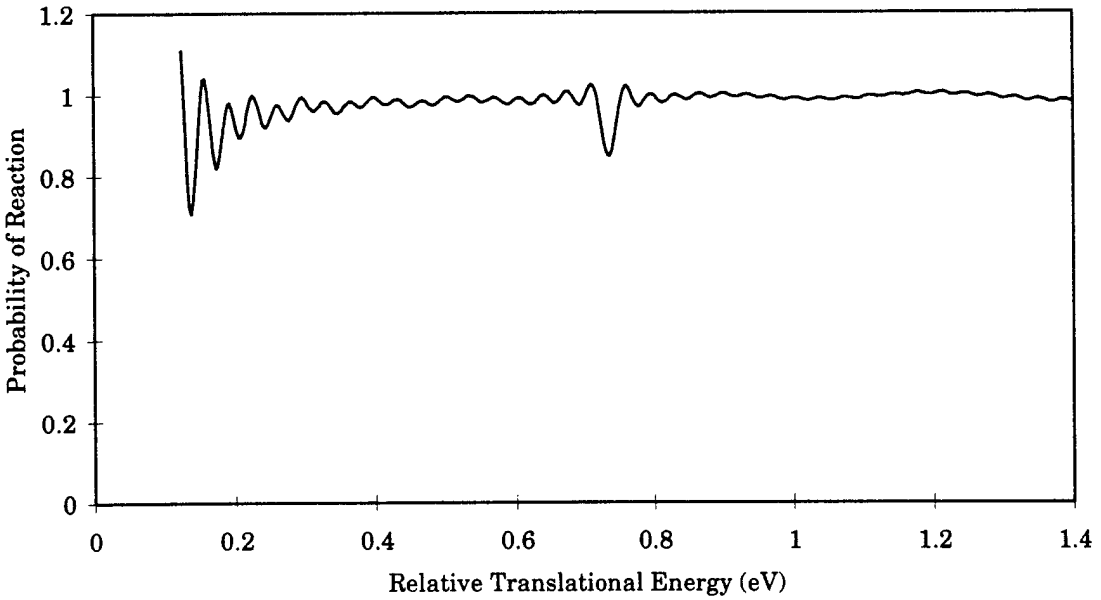

Figure 5.10 Probability of reaction for the two coupled Morse oscillator LLL mass configuration for the reaction $A + BC(\nu = 0) \rightarrow AB(\nu' = 0) + C$ where the correlation function is computed without the use of absorbing boundary conditions.

boundary conditions, shown in Figure 5.15, and without using absorbing boundary conditions, shown in Figure 5.16. The new set of absorbing boundary conditions are constructed using Jacobi coordinates appropriate to each channel and then transforming them to bond coordinates. For example, in the $A + BC$ channel, the area of the channel in which to apply absorbing boundary conditions is selected. Then, at each point in this area, the (X, Y) coordinates are transformed according to Equation 2.4 into the Jacobi coordinates (r_α, R_α). Next, the absorbing boundary conditions are computed using Equation 2.8 except that now the potential is given in terms of $V_a(r_\alpha, R_\alpha)$ instead of $V_a(X)$. The placement of the absorbing boundary conditions is still subject to the restriction that they are non-zero only where the initial Møller states are zero. Figure 5.17 illustrates the probability of reaction for the three sets of absorbing boundary conditions. In each case, the oscillations change but the position of the resonances do not. The resonances and the underlying shape of the curve are probably real with the overlying oscillations due to either absorbing boundary

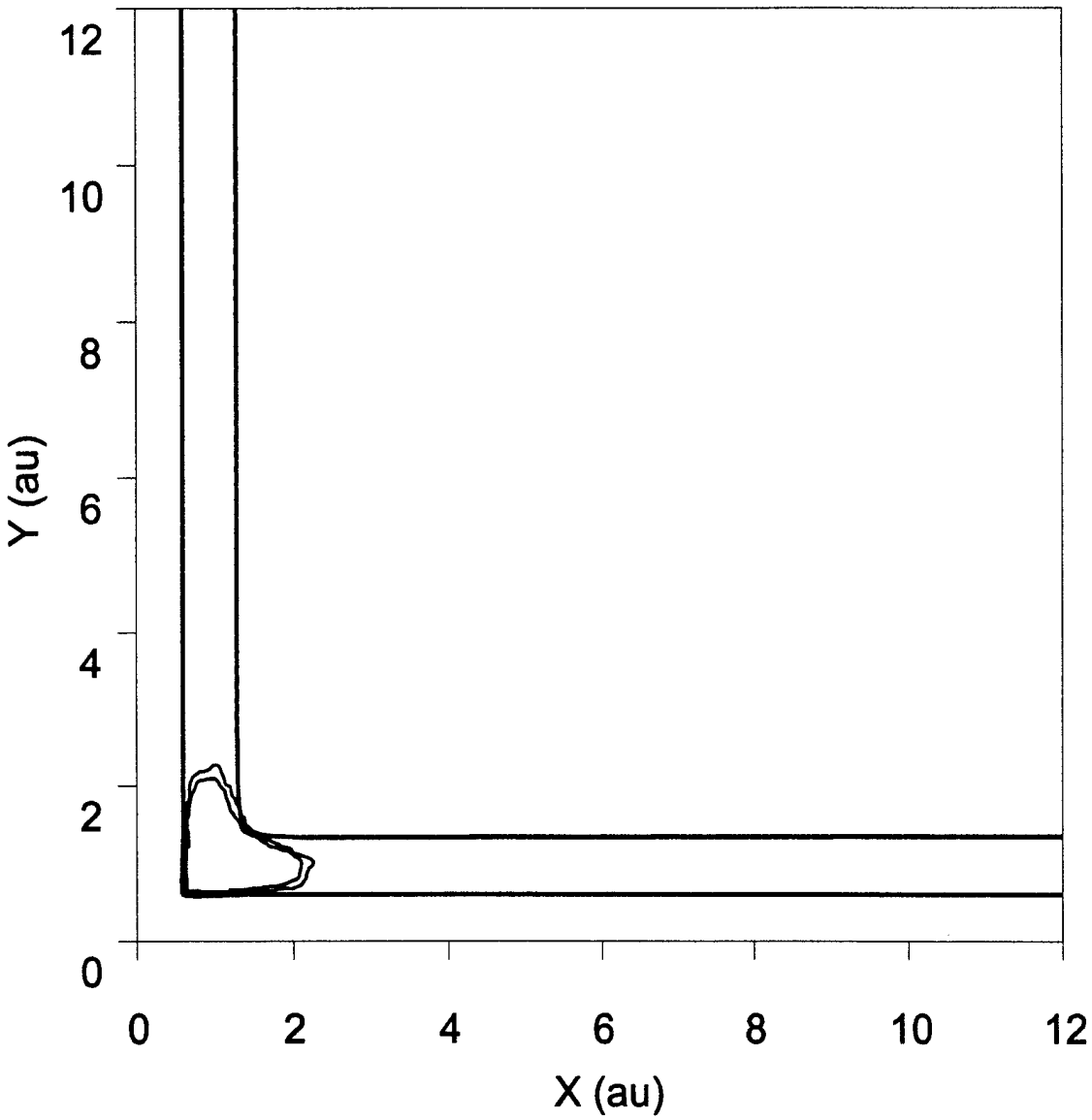

Figure 5.11 Compact Møller states and absorbing boundary condition placement for the two coupled Morse oscillator MLM mass configuration. The two parallel contours represent the 0.1 au contours of the potential energy surface. The dot represents the bottom of the well in the interaction region. The two closed contours are the 0.1 au contours of the absolute value of the Møller states. The shaded region represents the area in which the absorbing boundary conditions are non-zero.

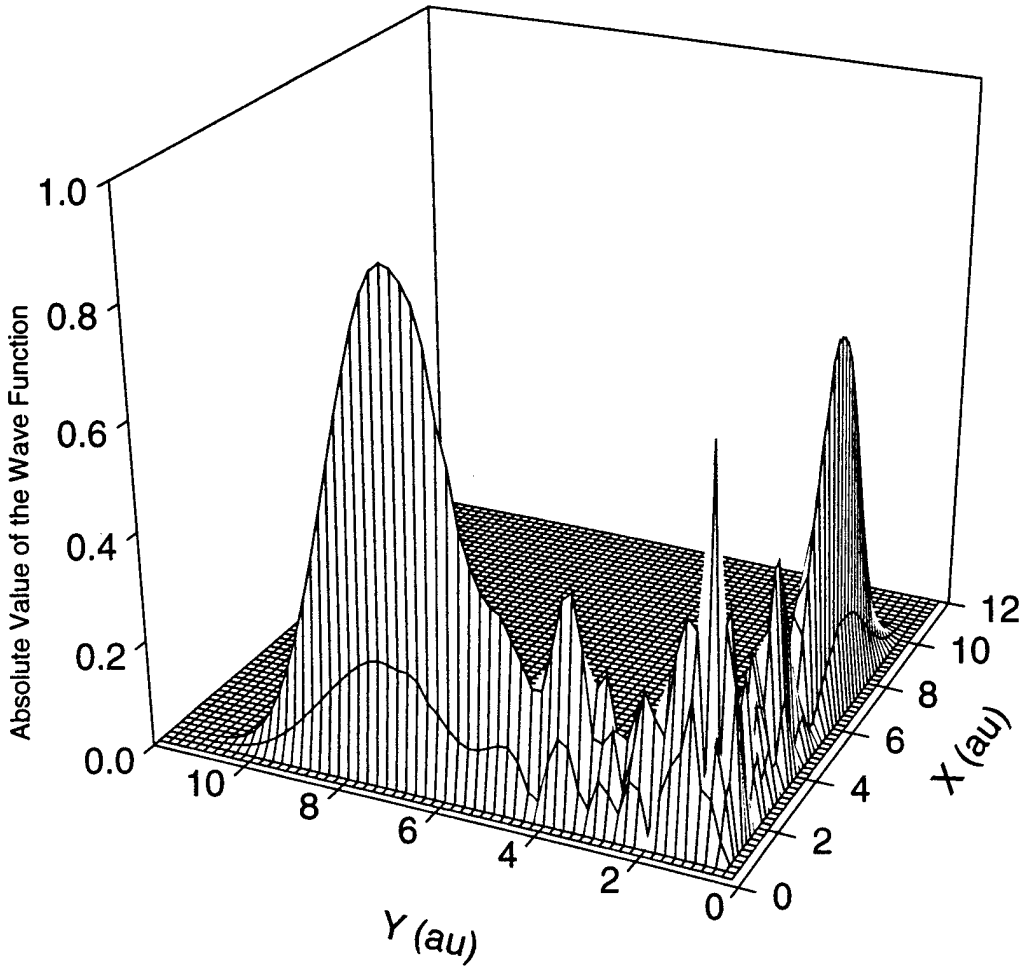

Figure 5.12 Surface plot of the absolute value of the evolving MLM reactant Møller state at $t = +1000$ au. The reactant channel is parallel to the X direction and the product channel is parallel to the Y direction. The evolving Møller state has bifurcated into both channels while a quasi-bound state is evident in the interaction region.

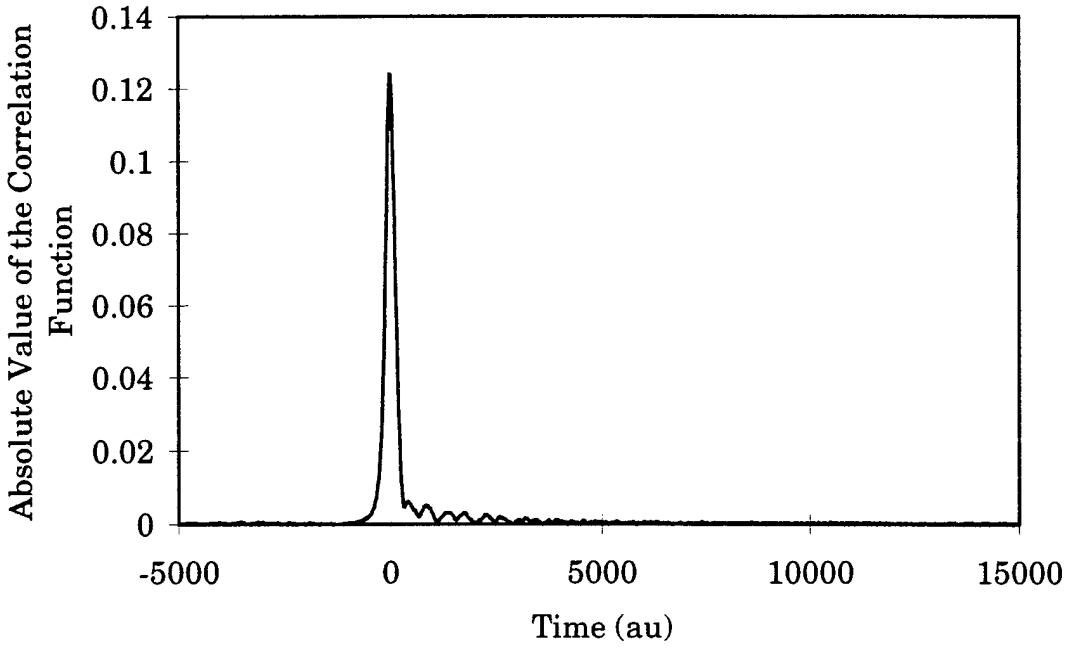

Figure 5.13 Absolute value of the correlation function for the two coupled Morse oscillator MLM mass configuration for the reaction $A + BC(v = 0) \rightarrow AB(v' = 0) + C$.

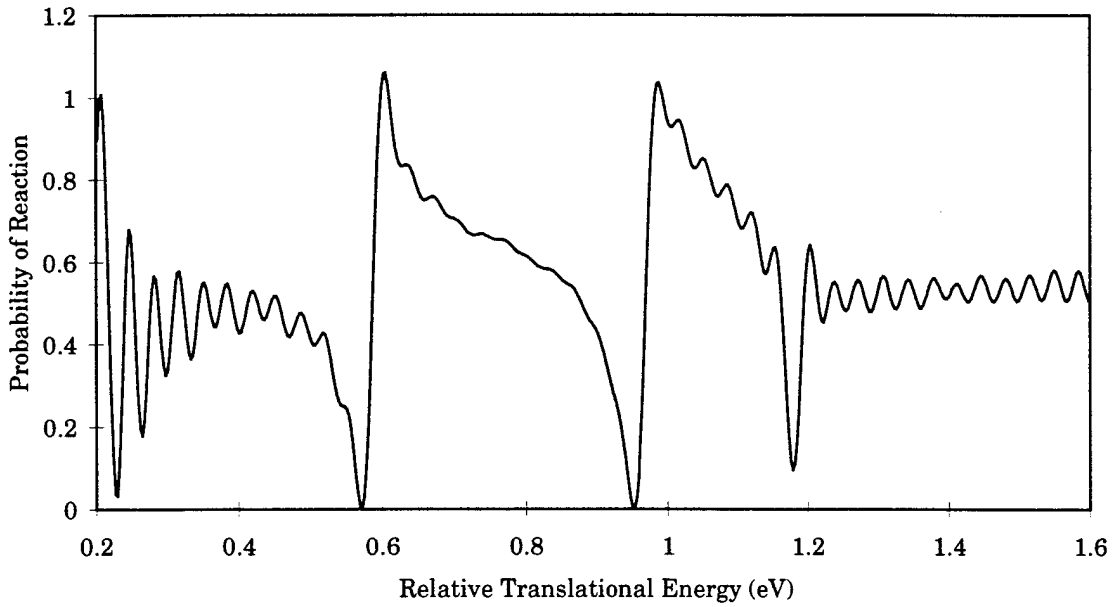

Figure 5.14 Probability of reaction for the two coupled Morse oscillator MLM mass configuration for the reaction $A + BC(v = 0) \rightarrow AB(v' = 0) + C$.

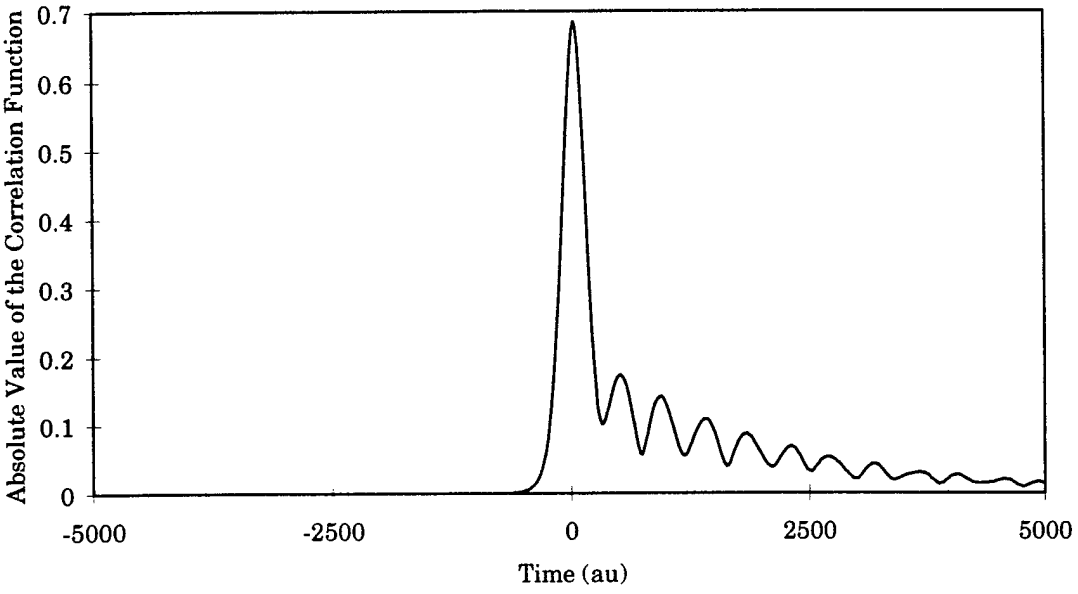

Figure 5.15 Absoute value of the correlation function for the two coupled Morse oscillator MLM mass configuration for the reaction $A + BC(v = 0) \rightarrow AB(v' = 0) + C$. In this calculation, the ABC are first constructed in Jacobi coordinates and then transformed to bond coordinates.

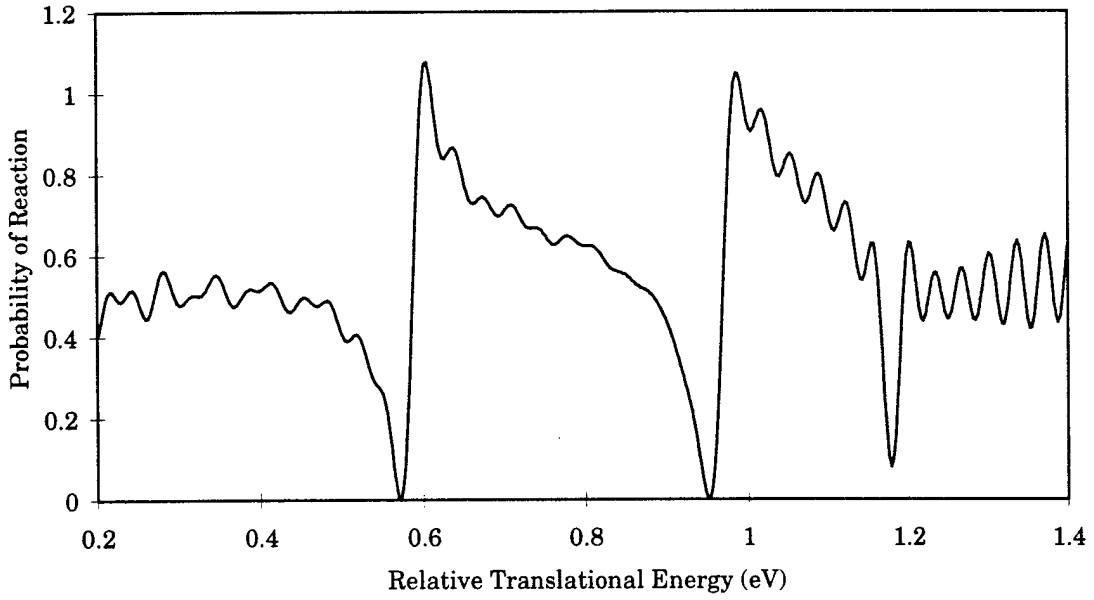

Figure 5.16 Probability of reaction for the two coupled Morse oscillator MLM mass configuration for the reaction $A + BC(v = 0) \rightarrow AB(v' = 0) + C$. In this calculation, the ABC are first constructed in Jacobi coordinates and then transformed to bond coordinates.

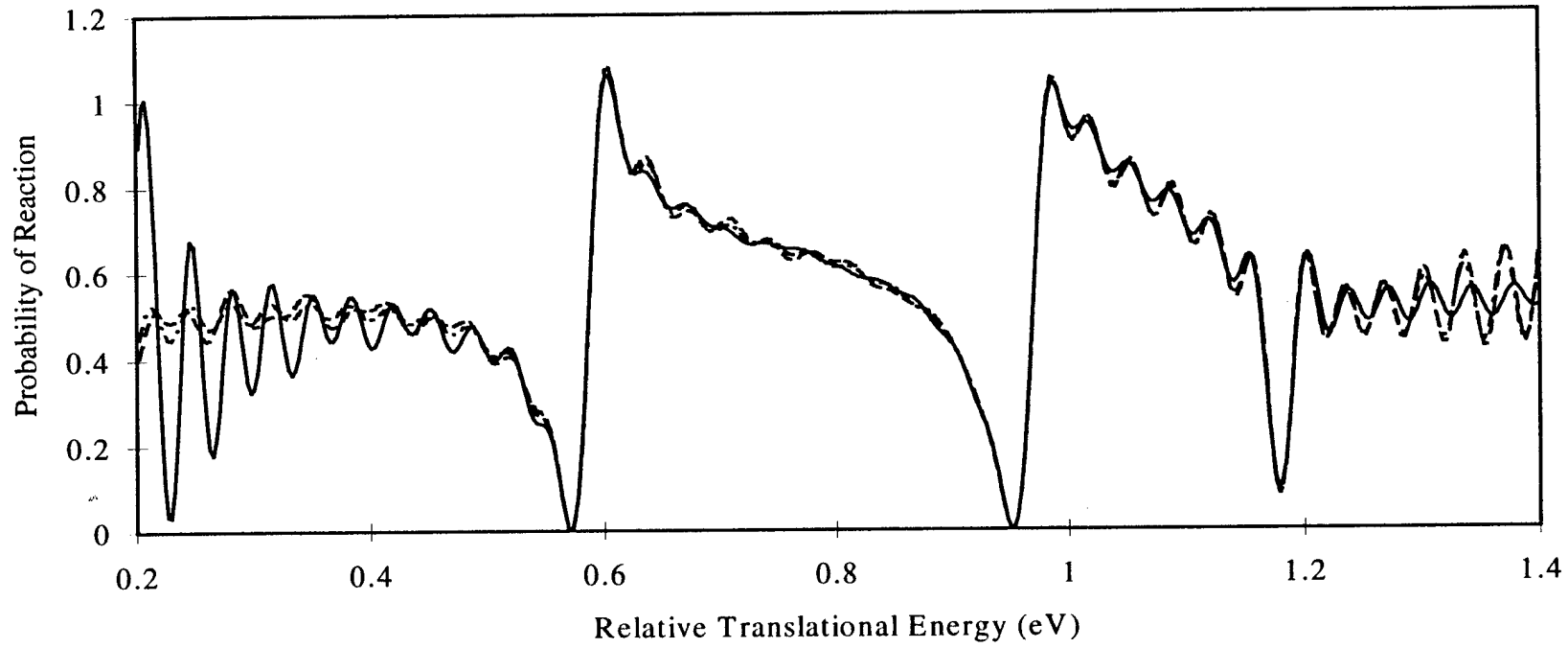

Figure 5.17 Probability of reaction for the two coupled Morse oscillator MLM mass configuration for the reaction $A + BC(v = 0) \rightarrow AB(v' = 0) + C$. Two of the calculations were performed using different absorbing boundary conditions were used (solid and dashed lines). One calculation (dash-dot line) did not use absorbing boundary conditions at all.

condition reflection error, for the solid and dashed lines, or are due to prematurely terminating the computation of the correlation function in order to avoid edge of grid reflection for the dash-dot line.

5.2.4 HLH S-matrix elements. Figure 5.18 illustrates that the HLH Møller states are well localized in the interaction region. In the correlation function, shown in Figure 5.19, the onset of absorbing boundary condition reflection error is quite clearly visible at approximately $t = +6000$ au. In order to test that the oscillations in Figure 5.19 are due to absorbing boundary condition reflection, another calculation was performed using the same absorbing boundary conditions placed further from the interaction region on a larger grid. Figure 5.20 illustrates that as the absorbing boundary conditions are moved further from the interaction region, the onset of oscillations in the correlation function do occur later in time are are due to absorbing boundary condition reflection error. The probability of reaction, shown in Figure 5.21 using the correlation function shown in Figure 5.19, exhibits a resonance at 0.34 eV and an overlying oscillation. As in both the LLL and MLM mass configurations, another computation of the correlation function without the use of absorbing boundary conditions was performed in order to determine which features in the probability of reaction in Figure 5.21 are most likely real and which are due to reflection error. Figure 5.22 illustrates the resulting probability of reaction for the three calculations. Figure 5.23 illustrates the correlation function where the computation does not use absorbing boundary conditions. The oscillations at $t = +6000$ au are absent. However, in order to avoid edge of grid reflections, the computation is terminated prematurely which will lead to spurious oscillations in the resulting S–matrix elements. In each calculation, the resonance in the probability of reaction at 0.34 eV remains and is most likely real as well as the underlying shape of the curve. However, the remaining oscillations change in both amplitude and frequency are are due to errors introduced by reflection from the absorbing boundary conditions (solid

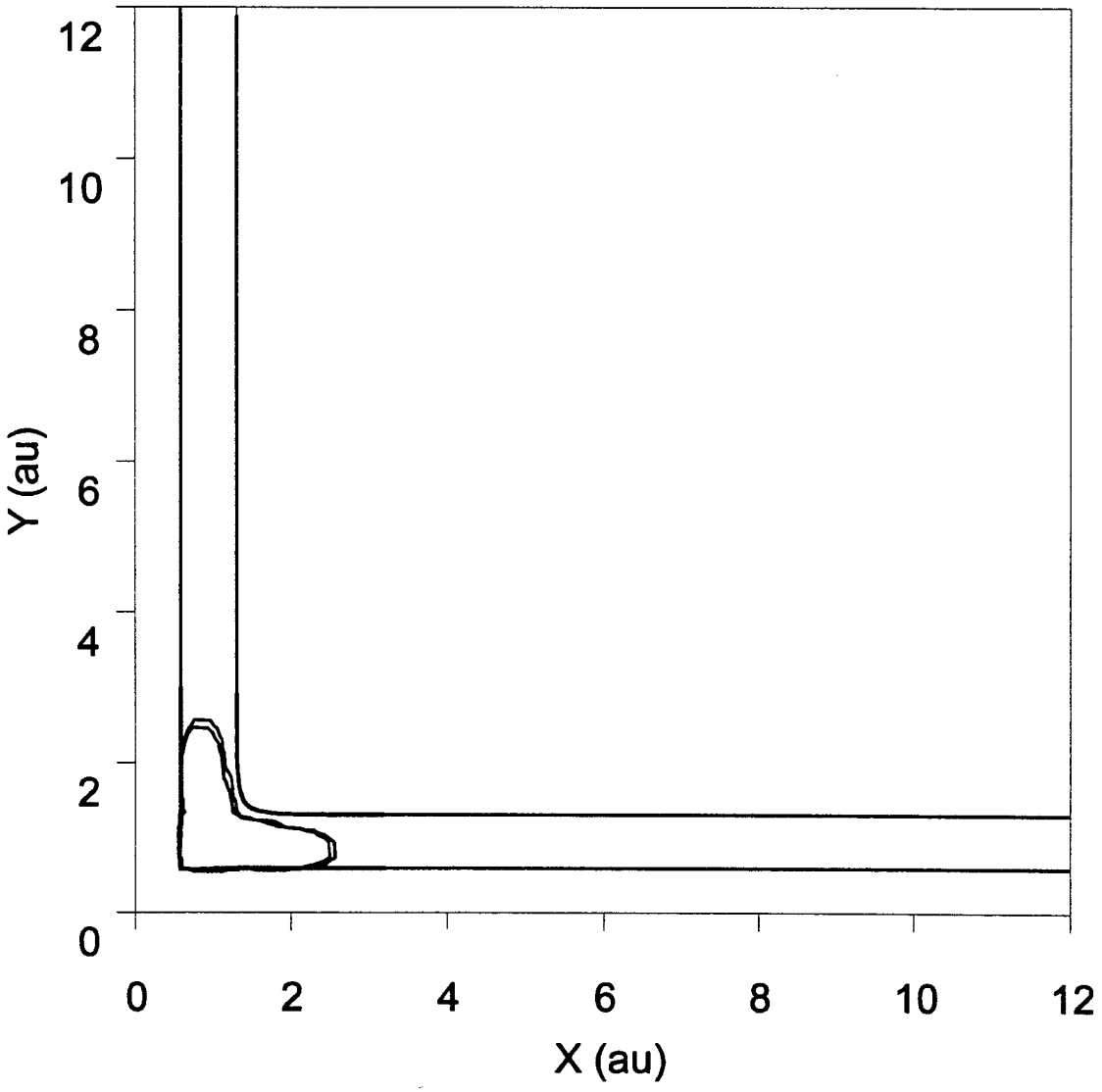

Figure 5.18 Compact Møller states and absorbing boundary condition placement for the two coupled Morse oscillator HLH mass configuration. The two parallel contours represent the 0.1 au contours of the potential energy surface. The dot represents the bottom of the well in the interaction region. The two closed contours are the 0.1 au contours of the absolute value of the Møller states. The shaded region represents the area in which the absorbing boundary conditions are non-zero.

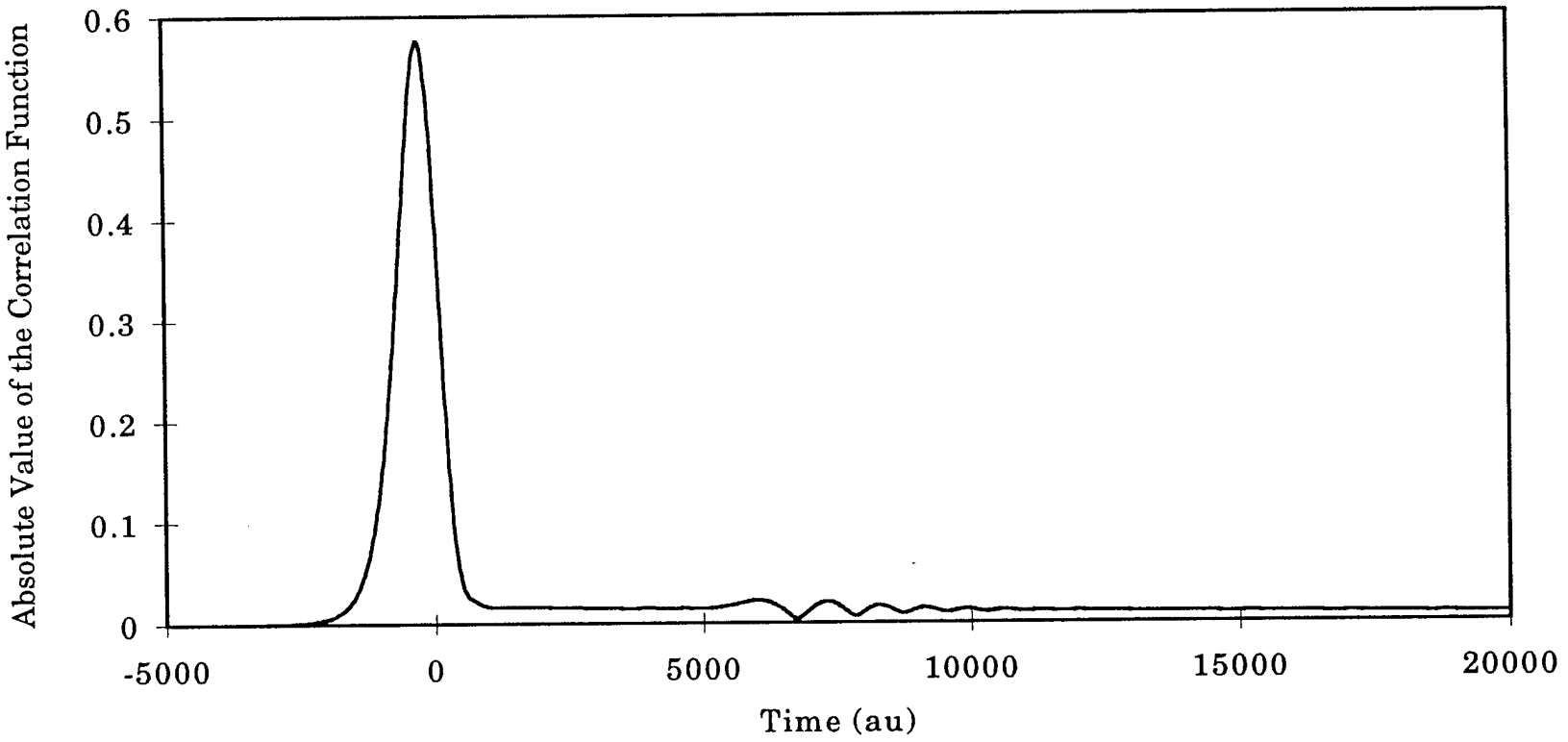

Figure 5.19 Absolute value of the correlation function for the two coupled Morse oscillator HLH mass configuration for the reaction $A + BC(v = 0) \rightarrow AB(v' = 0) + C$. A clear onset of ABC reflection error is evident at approximately t = 6000 au.

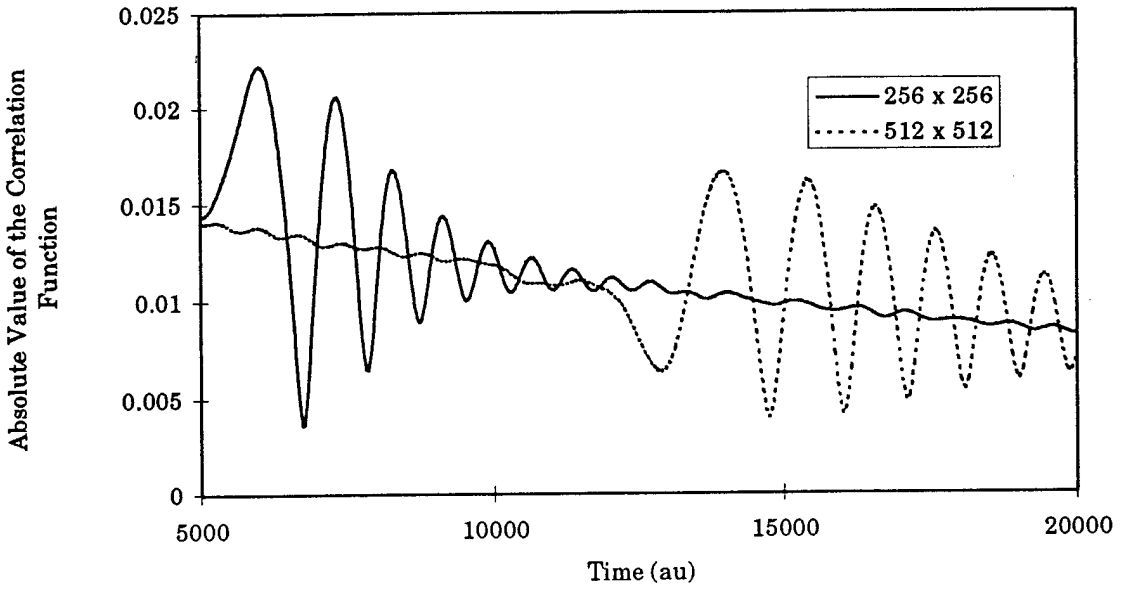

Figure 5.20 Absolute value of the correlation function for the two coupled Morse oscillator HLH mass configuration for the reaction $A + BC(v = 0) \rightarrow AB(v' = 0) + C$ on two different grid sizes.

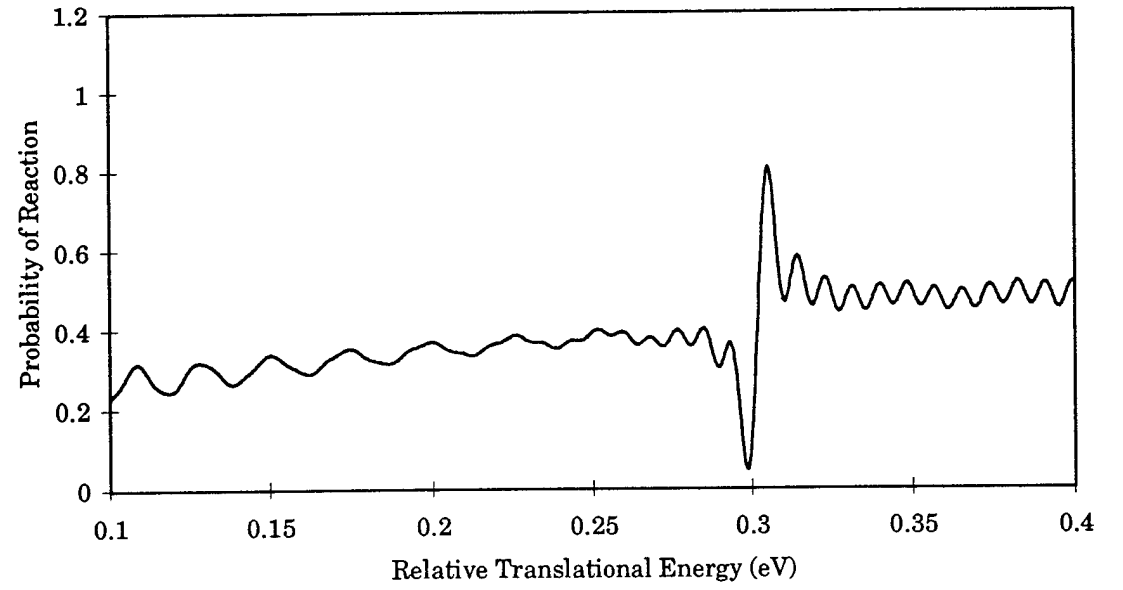

Figure 5.21 Probability of reaction for the two coupled Morse oscillator HLH mass configuration for the reaction $A + BC(v = 0) \rightarrow AB(v' = 0) + C$. The correlation function used to compute this probability is shown in Figure 5.19.

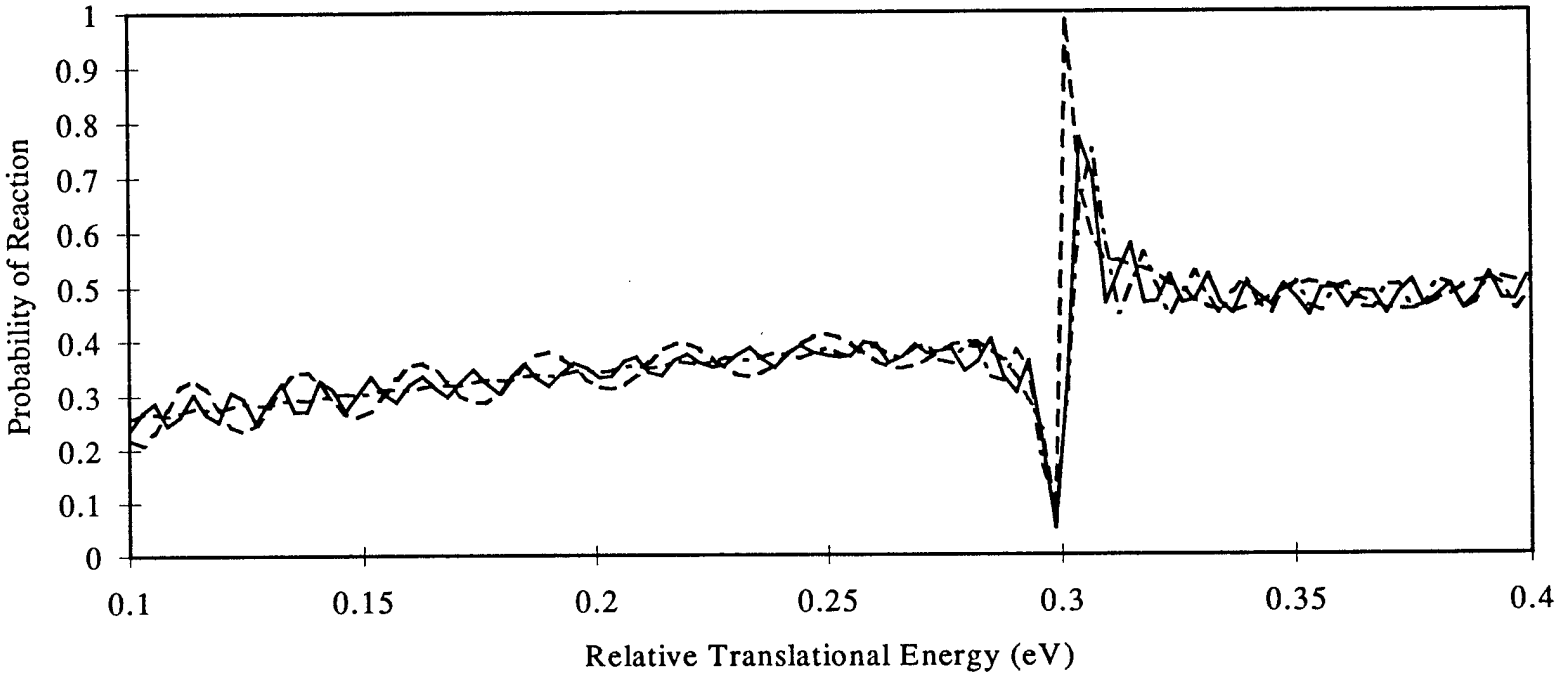

Figure 5.22 Probability of reaction for the two coupled Morse oscillator HLH mass configuration for the reaction $A+BC(v=0) \rightarrow AB(v'=0)+C$. Two of the calculations were performed using different absorbing boundary conditions were used (solid and dashed lines). One calculation (dash-dot line) did not use absorbing boundary conditions at all.

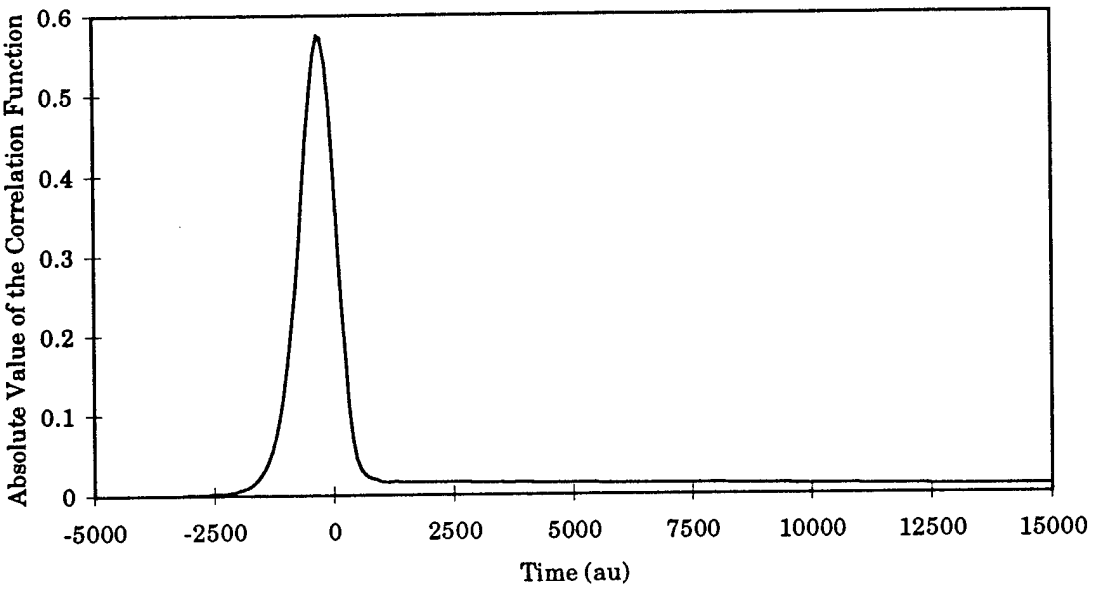

Figure 5.23 Absolute value of the correlation function for the two coupled Morse oscillator HLH mass configuration for the reaction $A + BC\,(\nu = 0) \rightarrow AB\,(\nu' = 0) + C$ where absorbing boundary conditions were not used.

and dashed lines) or premature termination of the correlation function calculation (dash-dot line).

5.3 S–matrix elements for absorbing boundary condition reflection

In order to more fully investigate the problem of absorbing boundary condition reflection error, S–matrix elements were computed for absorbing boundary condition reflection using a simple trough potential energy surface for the LLL, MLM, and HLH mass configurations.

5.3.1 Trough potential energy surface. The potential energy surface is simply a trough parallel to the X direction and a Morse oscillator in the Y direction given by

$$V_{trough}\,(X,Y) = D_e\left\{1 - \exp\left[-\alpha\,(Y - r_e)\right]\right\}^2, \tag{5.4}$$

where V_{trough} has the same form as the asymptotic limit of the channels in the full two dimensional calculation. In this calculation, the scattering potential (which defines

the interaction region) is chosen to be the absorbing boundary conditions used in the full two dimensional calculation. Because, in the channel packet method, we are free to choose the coordinate offset and zero of time, the initial wave packets and final Møller states can be the same by placing the coordinate offset far from the absorbing boundary conditions. Figure 5.24 illustrates these points. The shaded region represents the area in which the absorbing boundary conditions are non-zero. In this calculation, the absorbing boundary conditions are the scattering potential and thus also represent the interaction region. The two parallel lines represent the 0.1 au contours of the trough potential given in Equation 5.4. The closed contours at the right end of the potential represent both the initial wave packet and final Møller state. They are the same since the initial wave packet is placed in the asymptotic limit and under propagation by the Møller Operators given in Equation 2.10, the asymptotic and full scattering Hamiltonians are the same thus the effect of the Møller Operator is multiplication by 1.

5.3.2 S-matrix elements. Figures 5.25, 5.26 and 5.27 illustrate the probability of reflection for the reaction $A + BC(\nu = j) \rightarrow A + BC(\nu' = j)$, $j = 0, 1, 2$ for the LLL, MLM and HLH mass configurations. Comparison of the overall magnitudes of the probability of reflection for the three mass configurations and, within a given mass configuration, the three internal vibrational eigenstates, indicates that wave packets in the MLM mass configuration are less likely to undergo absorbing boundary condition reflection than the LLL and HLH mass configurations. For some energies, the HLH or LLL mass configurations may have a lower probability of reflection, overall, they are more likely to reflect than the MLM mass configuration. In the MLM and HLH mass configurations wave packets constructed from the $\nu = 0$ internal vibrational eigenstate are more likely to undergo absorbing boundary condition reflection than wave packets constructed from the $\nu = 1$ and $\nu = 2$ internal vibrational eigenstates. The probability of reflection for $\nu' \neq \nu$ is essentially zero.

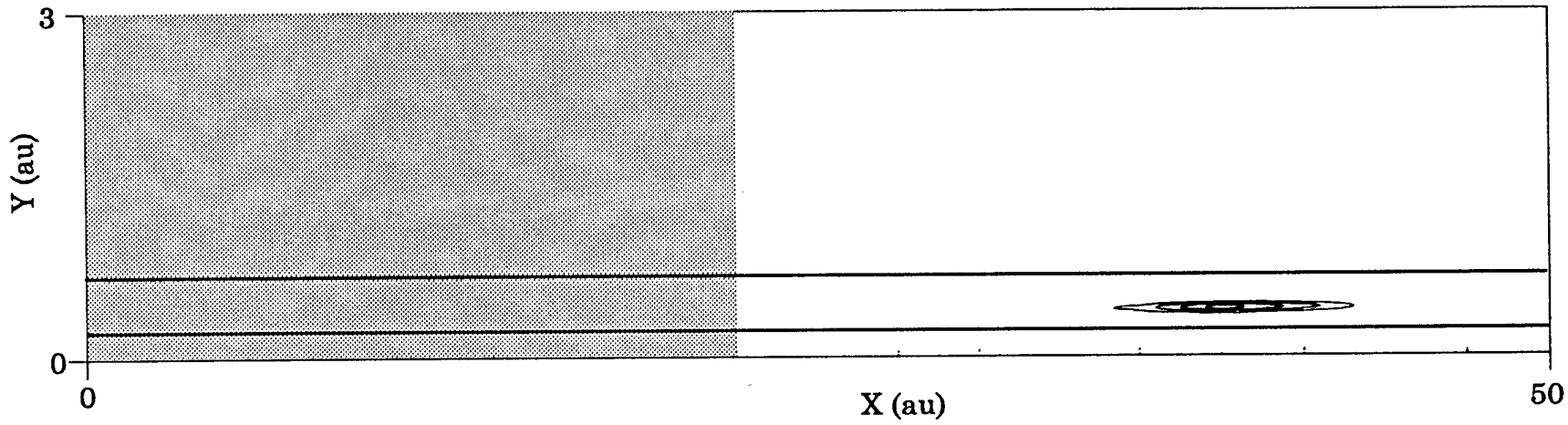

Figure 5.24 Contour plot of the trough potential used in obseriving and calculating S–matrix elements for absorbing boundary condition reflection. The two parallel lines represent the 0.1 au contours of the trough potential energy surface. The initial wave packet is represented by the closed contours. The shaded region represents the interaction region and the absorbing boundary condition scattering potential.

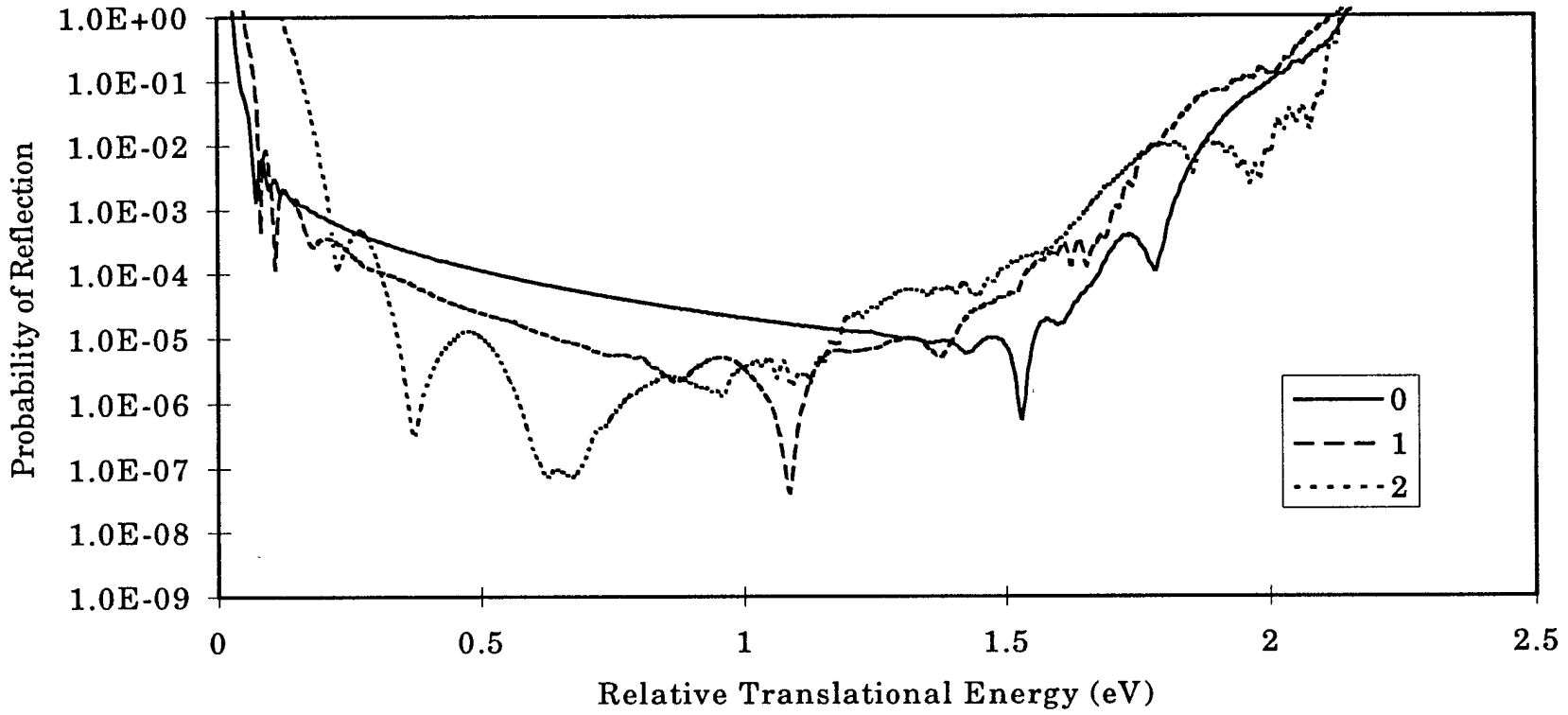

Figure 5.25 Probability of reflection for the reaction $A+BC(v=j) \rightarrow A+BC(v'=j)$, $j=0,1,2$ for the LLL mass configuration. The probability of reflection for $v \neq v'$ is essentially zero.

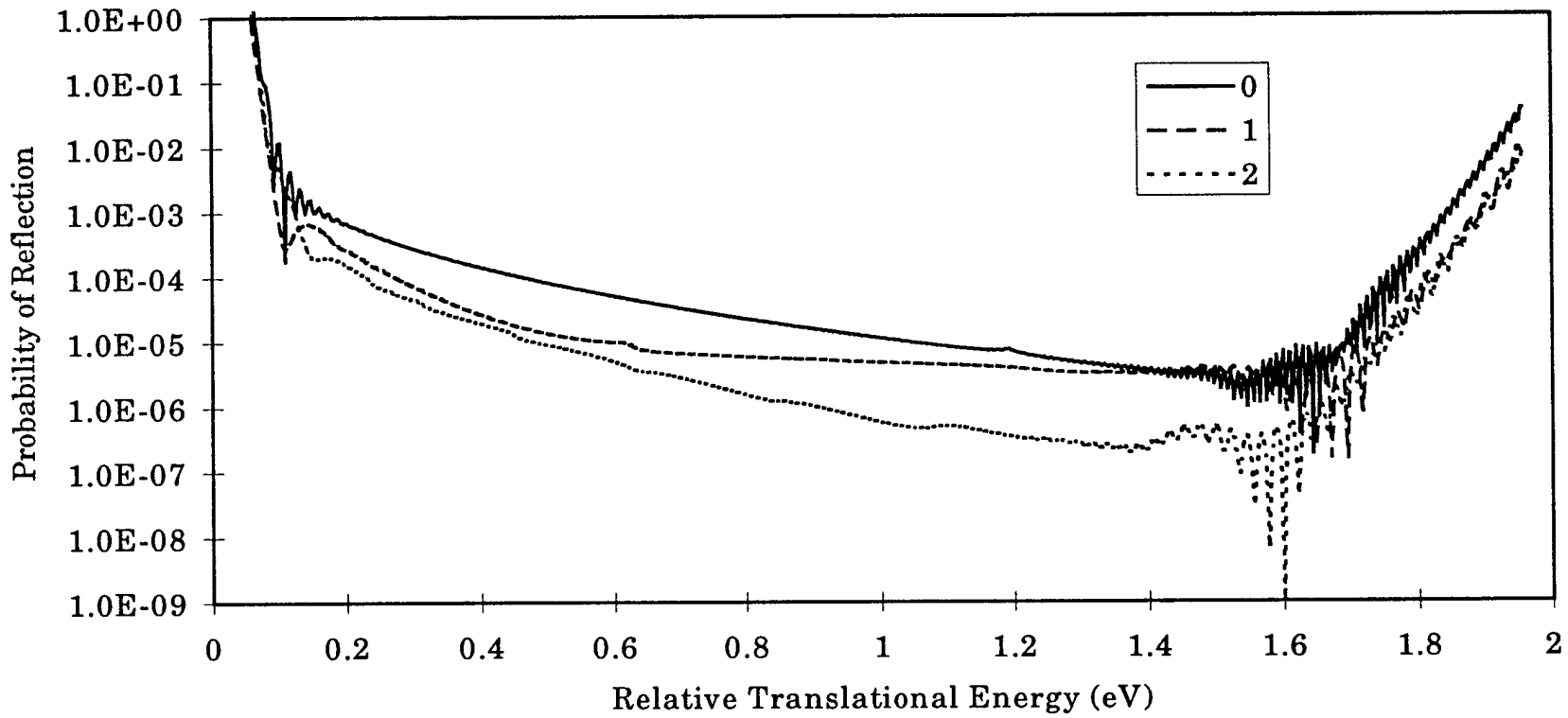

Figure 5.26 Probability of reflection for the reaction $A+BC(v=j)\rightarrow A+BC(v'=j)$, $j=0,1,2$ for the MLM mass configuration. The probability of reflection for $v\neq v'$ is essentially zero.

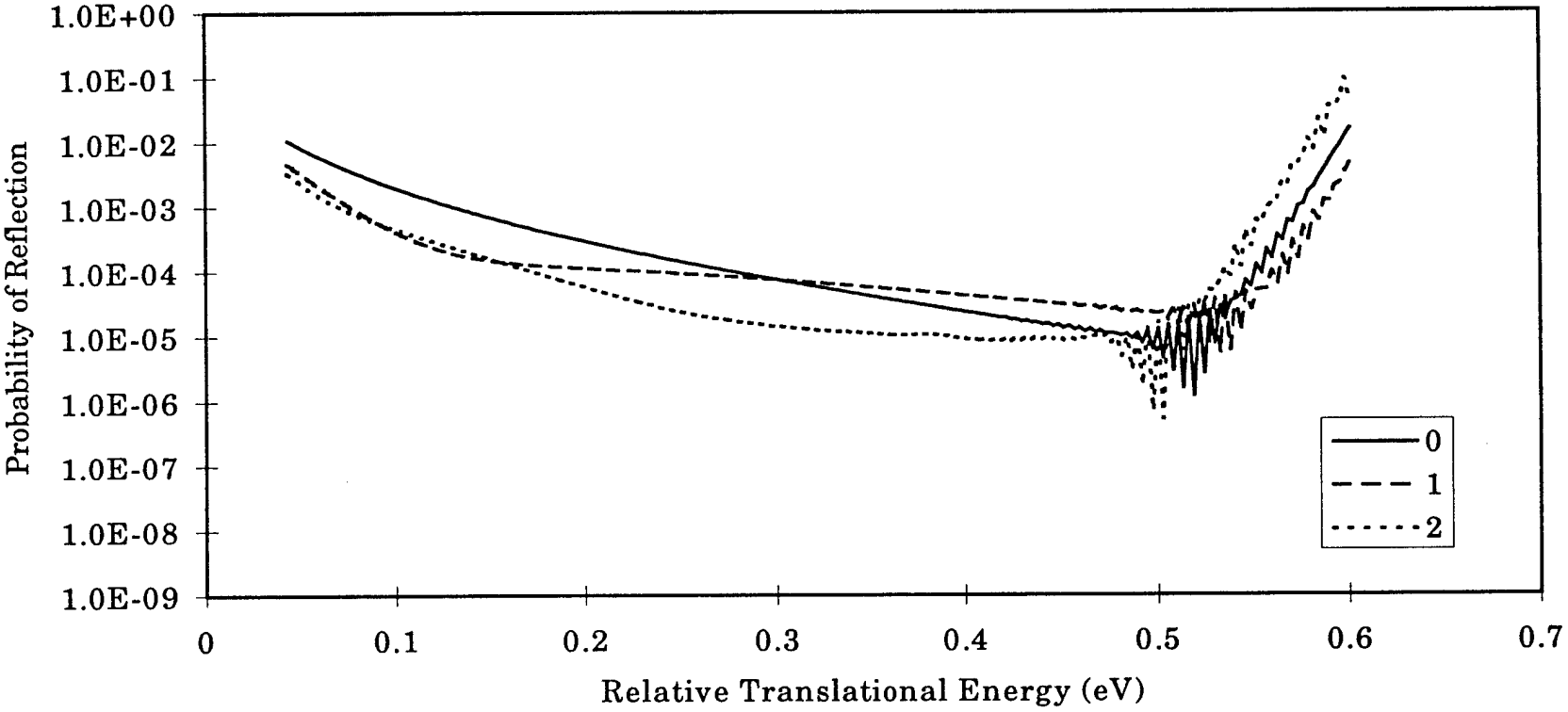

Figure 5.27 Probability of reflection for the reaction $A+BC(v=j) \rightarrow A+BC(v'=j)$, $j=0,1,2$ for the HLH mass configuration. The probability of reflection for $v \neq v'$ is essentially zero.

5.4 Summary

The initial purpose of this part of the study was to investigate, using the channel packet method with absorbing boundary conditions, the effects of potential energy surface wells on the probability of reaction. However, absorbing boundary condition reflections introduce non-trivial errors into the correlation function with resulting errors in the S–matrix elements. Currently, the unambiguous signatures of absorbing boundary condition reflection error are S–matrix elements that fail to converge, probabilities of reaction significantly greater than one or oscillations in the probability of reaction which change with changes in the absorbing boundary conditions. Some insight into which features in the probability of reaction are real and which are due to absorbing boundary condition reflections can by obtained by computing the correlation function without absorbing boundary conditions. However, these comparisons only yield insight into where there might be sharp resonances and the overall trends in the probability of reaction.

VI. Two dimensional reactive quantum scattering for a model system of two coupled Morse oscillators in a light-heavy-light configuration

Quantum reactive scattering results are presented for a model system of two coupled Morse oscillators in a light-heavy-light (LHL) mass configuration. The conclusions in this chapter are based on observed features of the S–matrix elements and are primarily qualitative in nature.

6.1 S–matrix elements

The possibility of significant absorbing boundary condition reflection error for the LHL mass configuration needs to be eliminated before the effects of well depth and kinetic coupling may be explored. For the LHL mass configuration, the light masses are 2000 au and the heavy mass is 10,000 au. Using the same model potential energy surface as in Equation 5.1 with $D_e = 0.1$ au and $\alpha = 5.0$, the asymptotic limit of the Morse oscillator has 4 bound states where the $\nu = 0, 1, 2$ vibrational eigenstate energies are the same as for the HLH mass configuration in Table 5.2. The energies are the same since for both the HLH and LHL mass configurations the diatom mass configuration consists of a light atom and a heavy atom. Parameters for the Møller state calculation are given in Table 6.1 and the procedure for calculating the Møller states is the same as in Section 5.2.1. The probability of reaction shown in Figure 6.1 exhibits three sharp resonances. However, in light of the results in Chapter V, where absorbing boundary condition reflection introduced non-trivial errors into the calculation, two further computations of the correlation function were performed in order to investigate the effects, if any, of absorbing boundary condition reflection error. The first computation involved a larger grid where the absorbing boundary conditions were moved further from the interaction region. Figure 6.2 illustrates the results compared to the correlation function computation on a smaller

Table 6.1 Initial Møller state calculation parameters for the LHL mass configuration.

Parameter	Value (au)	Notes
xmin1	0.2	minimum X grid boundary
xmin2	0.2	minimum Y grid boundary
ma	2000.0	mass of atom a
mb	10000.0	mass of atom b
mc	2000.0	mass of atom c
deltax1	0.05	X grid resolution
deltax2	0.05	Y grid resolution
nstep	1200	number of time steps
sftcnt	1200	number of time steps to stop the propagation at
deltat	1.0	time step
ioff1	1.4	initial X offset (0 for product wave packet)
ioff2	0.0	initial Y offset (1.4 for product wave packet)
imom1	-1.4	initial P_X offset (0 for product wave packet)
imom2	0.0	initial P_Y offset (-1.4 for product wave packet)
sprd1	0.3	initial relative wave packet spread in the X direction
sprd2	0.3	initial relative wave packet spread in the Y direction
tau1	-1200.0	temporal offset for channel 1 initial wave packet
tau2	-1200.0	temporal offset for channel 2 initial wave packet
evch	1	asymptotic eigenstate number

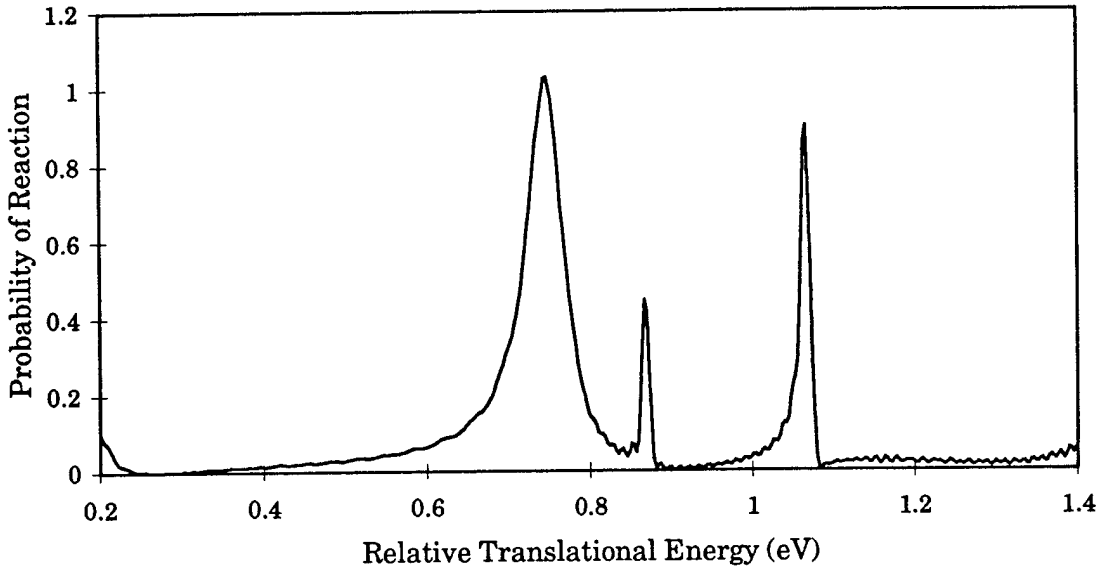

Figure 6.1 Probability of reaction for the two coupled Morse oscillator LHL mass configuration for the reaction $A + BC(v = 0) \rightarrow AB(v' = 0) + C$.

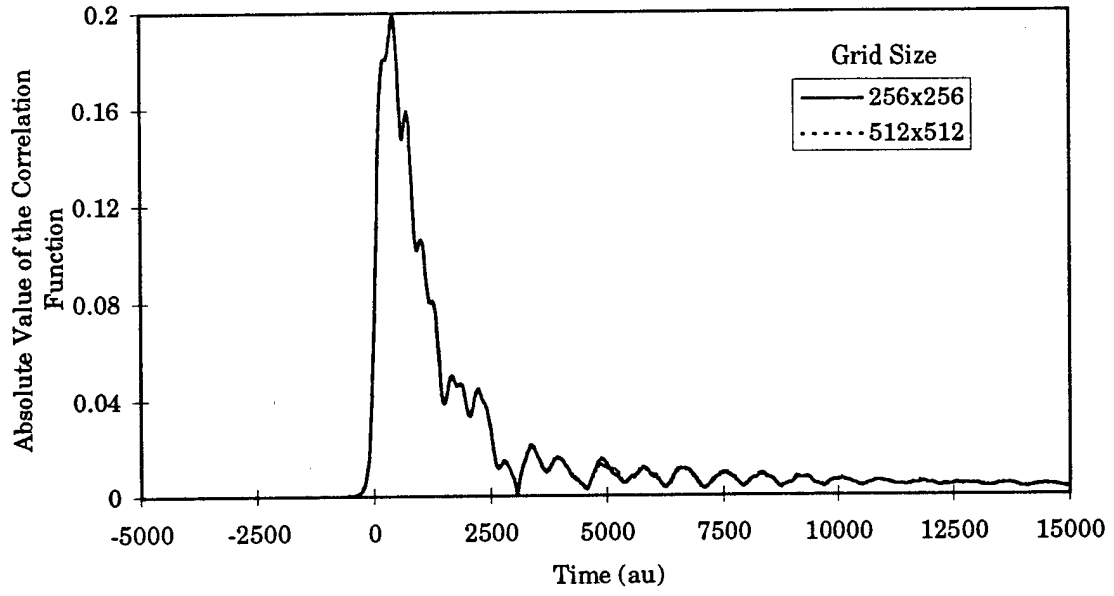

Figure 6.2 Absolute value of the correlation function for the two coupled Morse oscillator LHL mass configuration for the reaction $A + BC(v = 0) \rightarrow AB(v' = 0) + C$ for two different grid sizes. For the larger grid size, the absorbing boundary conditions are placed further away from the interaction region.

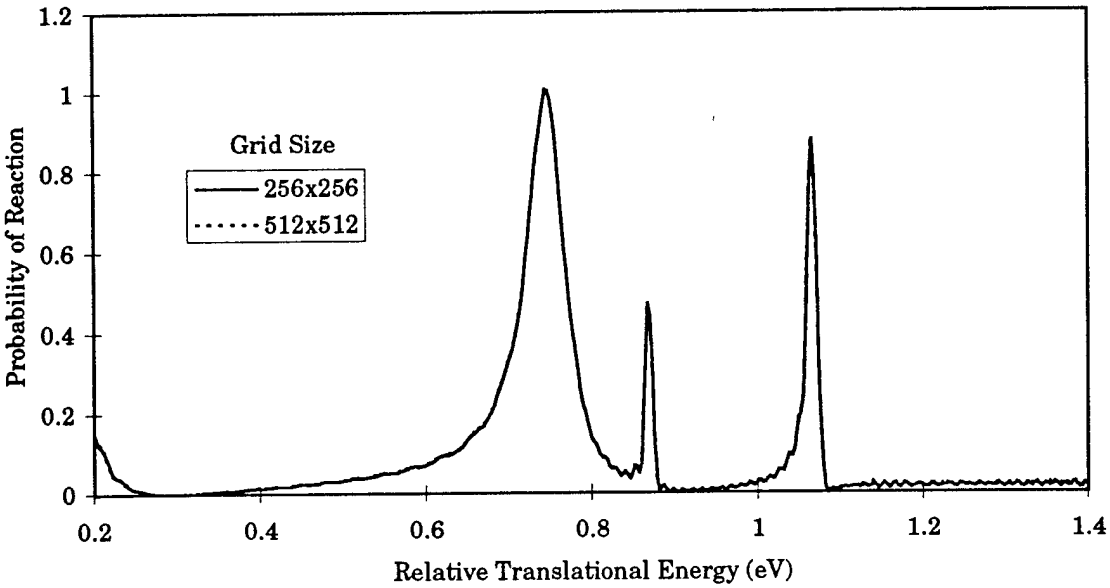

Figure 6.3 Probability of reaction for the two coupled Morse oscillator LHL mass configuration for the reaction $A+BC\,(0) \rightarrow AB\,(0)+C$ for two different grid sizes. For the larger grid size, the absorbing boundary conditions are placed further away from the interaction region.

grid. The differences between the two functions are small and the resulting S–matrix elements, shown in Figure 6.3, are essentially the same as in Figure 6.1. The second computation, shown in Figure 6.4, involved using the large grid without the application of absorbing boundary conditions. The computation of the correlation function without absorbing boundary conditions introduces oscillations into the S–matrix elements shown in Figure 6.5. These oscillations are due to terminating the correlation function calculation before the correlation function has reached zero in order to avoid the onset of edge of grid reflection. The comparison of all three computations demonstrates that absorbing boundary condition reflection introduces negligible error into the resulting S–matrix elements for the LHL mass configuration.

The original intent of combining absorbing boundary conditions with the channel packet method was to improve the efficiency of the computation of S–matrix elements. Figure 6.5, where the correlation function is computed without the use of absorbing boundary conditions, illustrates that on a 512×512 grid without absorbing

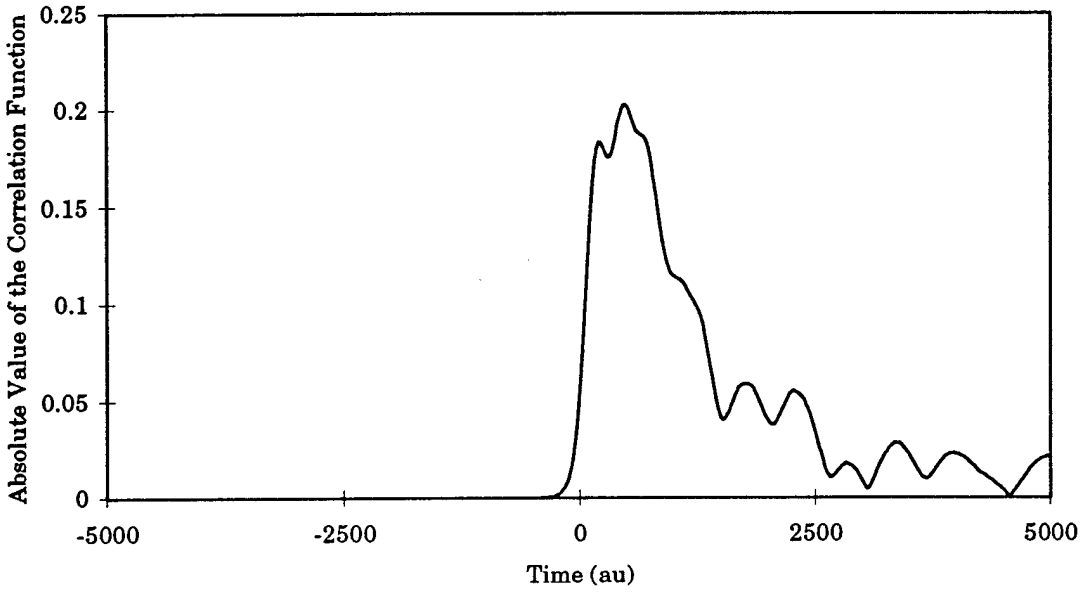

Figure 6.4 Absolute value of the correlation function for the two coupled Morse oscillator LHL mass configuration for the reaction $A + BC(v = 0) \rightarrow AB(v' = 0) + C$ without the use of absorbing boundary conditions.

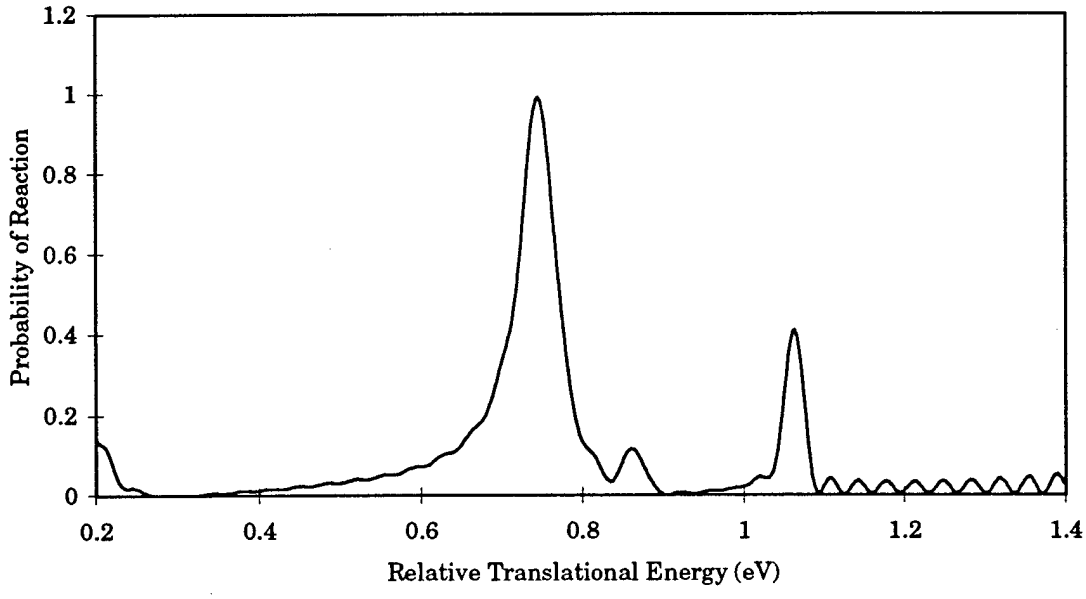

Figure 6.5 Probability of reaction for the two coupled Morse oscillator LHL mass configuration for the reaction $A + BC(v = 0) \rightarrow AB(v' = 0) + C$ without the use of absorbing boundary conditions.

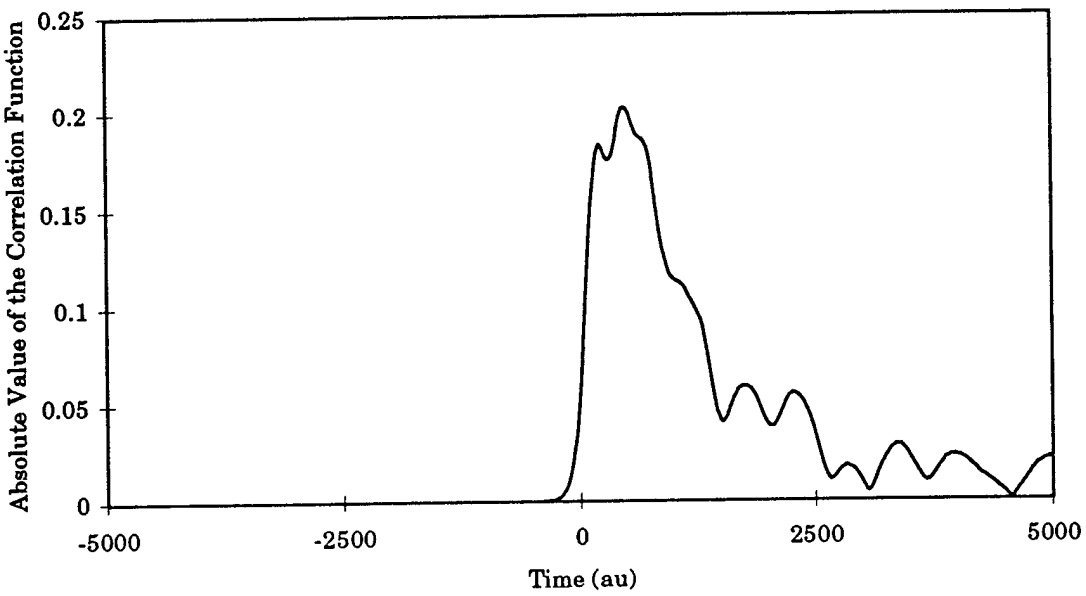

Figure 6.6 Absolute value of the correlation function for the two coupled Morse oscillator LHL mass configuration for the reaction $A + BC(0) \rightarrow AB(0) + C$ where the grid size has been reduced to 128×128 and the absorbing boundary conditions moved closer to the interaction region.

boundary conditions, good S–matrix elements can be obtained. The calculation of the correlation function in Figure 6.4, on a MIPS R10000 Silicon Graphics workstation took approximately 55,000 seconds of CPU time. However, using absorbing boundary conditions and a small 128×128 grid, the calculation of the correlation function, shown in Figure 6.6, took only 1900 seconds of CPU time for a factor of 29 savings in computation time. As shown in Figure 6.7, the resulting S–matrix elements computed from the correlation function in Figure 6.6 are in good agreement with Figures 6.1 and 6.3. Again, the combination of absorbing boundary conditions with the channel packet method results in significant time savings as opposed to the channel packet method alone.

6.2 Resonances and well depth

Since the LHL mass configuration is effectively free of absorbing boundary condition reflection error, the influence of well depth on S–matrix elements can be

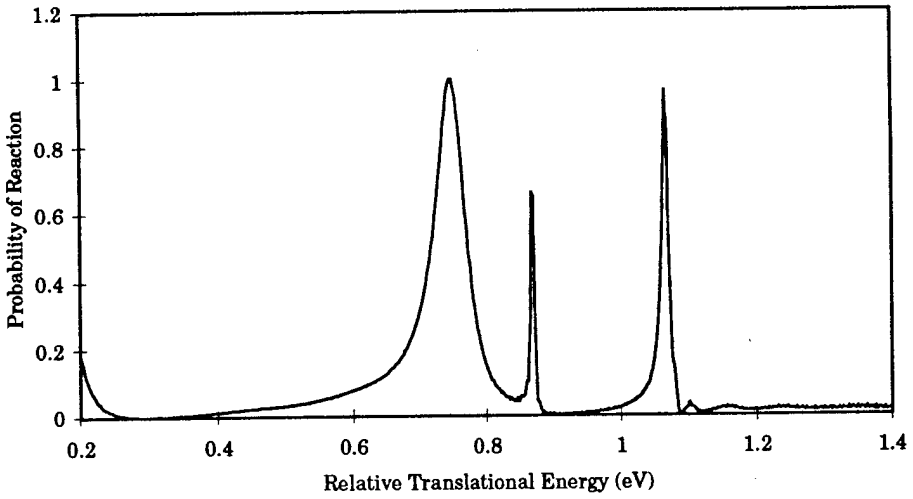

Figure 6.7 Probability of reaction for the two coupled Morse oscillator LHL mass configuration for the reaction $A + BC\,(0) \rightarrow AB\,(0) + C$ where the grid size has been reduced to 128×128 and the absorbing boundary conditions moved closer to the interaction region.

investigated. The well depth in the model potential energy surface is easily adjusted by changing the dissociation energy of the Morse oscillators, denoted by D_e in Equation 5.1. In this investigation, S–matrix elements are computed for values of D_e from 0.1 au to 0.26 au in steps of 0.01 au. The step size is purely arbitrary. For each value of D_e, the anharmonicity α was changed so that the spring constant of the harmonic limit of the Morse oscillator, given by $K = 2D_e\alpha^2$, remained the same. For each potential energy surface, the initial grid and wave packet parameters are the same as in Table 6.1. Figure 6.8 illustrates the probability of reaction for four values of D_e. Figures illustrating the probability of reaction for values of D_e from 0.1 au to 0.26 au in steps of 0.01 au are in Appendix D.

At first glance, a higher dissociation energy, i.e. a deeper well, leads to more resonances with doublets and then triplets appearing. By comparing S–matrix elements computed using different values of D_e, resonances that initially appear at high relative translational energy move to lower relative translation energy as the

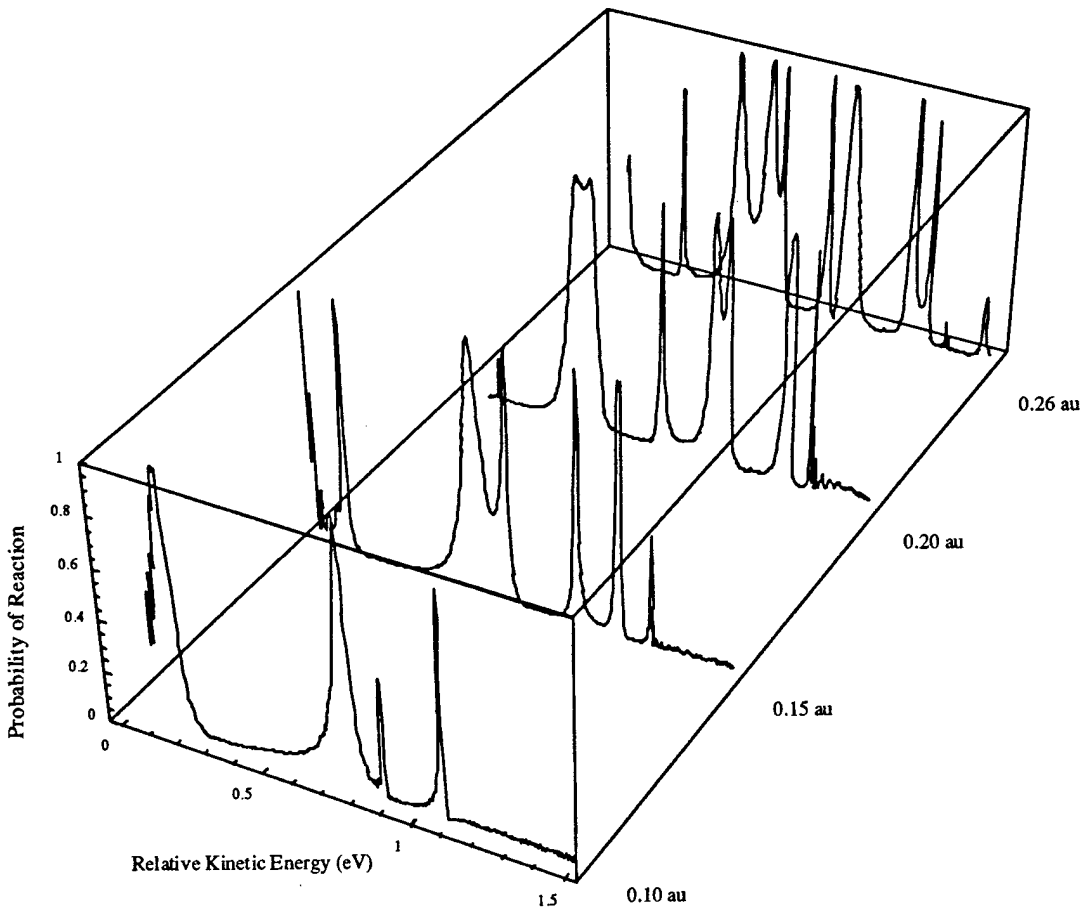

Figure 6.8 Probability of reaction as a function of dissociation energy for the two coupled Morse oscillator LHL mass configuration for the reaction $A + BC(0) \rightarrow AB(0) + C$. The dissociation energy is equal to 0.10 au, 0.15 au, 0.20 au and 0.26 au.

dissociation energy increases. The peak positions of several of the resonances with respect to potential energy surface dissociation energy is shown in Figure 6.9. The initial position appears, qualitatively, to be governed by an envelope. The form of the envelope can be fit by a function of the form

$$y = a + \frac{b}{x^2}, \tag{6.1}$$

where y is the resonance position and x is the dissociation energy. This envelope as well as the points used to derive it are shown in Figure 6.10.

In Figure 6.11, the position of a resonance with respect to dissociation energy is connected with a curve for a number of resonances. The connections between the points in Figure 6.9 which are not included in Figure 6.11 are more difficult to make due to the bifurcation and trifurcation of the underlying resonances. Each of the curves in Figure 6.11 has the same general shape, with the position of a resonance changing slowly at first and then more rapidly with increasing dissociation energy. Some resonances also appear to bifurcate with increasing well depth. In Figure 6.25, the resonance represented by the dashed line was chosen for further investigation due to the bifurcation at a dissociation energy of 0.19 au. S–matrix elements were computed for D_e = 0.18 to 0.20 au in steps of 0.002 au. Figure 6.12 illustrates the position of the bifurcating resonance as a function of dissociation energy. The bifurcation occurs between 0.184 and 0.186 au and the subsequent behavior of the resonance position rapidly approaches the general behavior of the other resonances as seen in Figure 6.9.

For the one dimensional square well, the resonances in the probability of transmission can be related to virtual states of the infinitely deep square well.[56,57] In order to investigate the possibility that such a relationship might exist for the two coupled Morse oscillators, the eigenstates of the harmonic limit need to be computed. This can be done analytically by constructing the force, **F**, and mass, **M**, matrices then

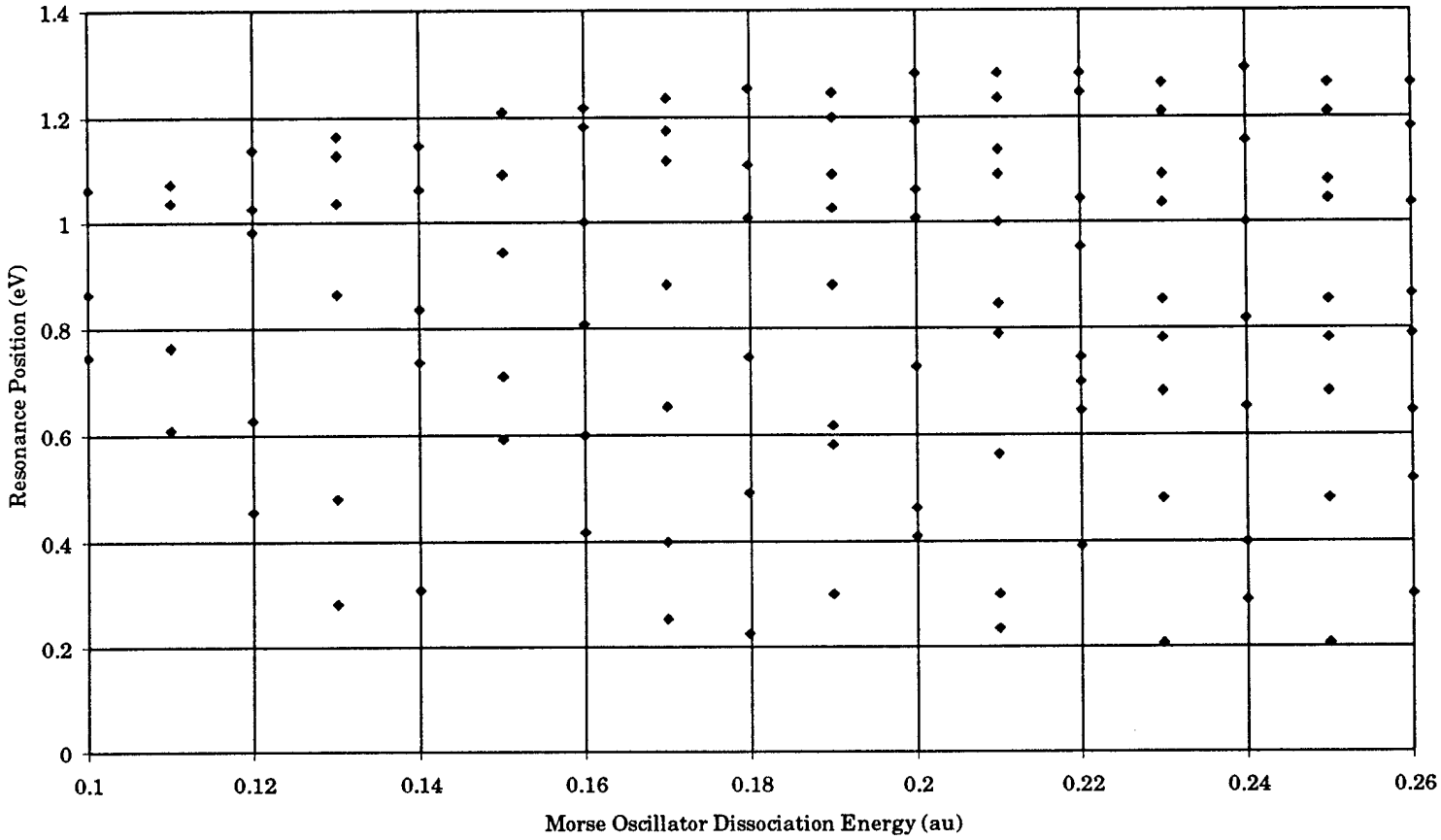

Figure 6.9 Position of S–matrix element resolances as a function of Morse oscillator dissociation energy.

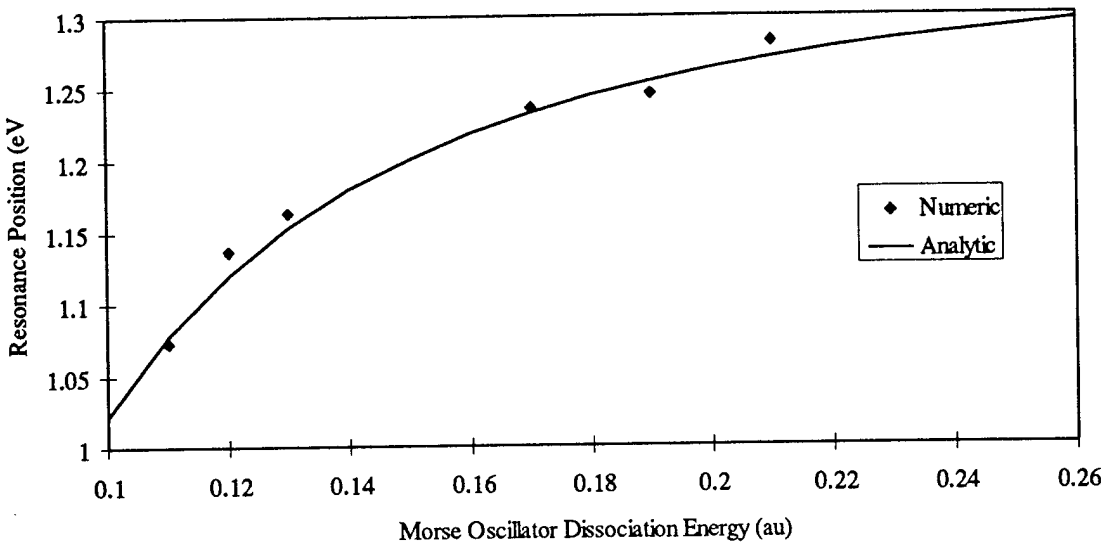

Figure 6.10 Qualitative envelope governing the initial position of a resonance in the probability of reaction.

diagonalizing the matrix $(\mathbf{M}^{-1}\mathbf{F})$.[62] The diagonal elements of the resulting matrix are the squares of the frequencies of the normal modes of the system. For the two coupled Morse oscillator potential, the force matrix is given by

$$\mathbf{F} = \begin{pmatrix} K & -K & 0 \\ -K & 2K & -K \\ 0 & -K & K \end{pmatrix}, \tag{6.2}$$

where K is the force constant of the harmonic limit of the Morse oscillator and the mass matrix is diagonal with $m_a = m_c$ and given by

$$\mathbf{M} = \begin{pmatrix} m_a & 0 & 0 \\ 0 & m_b & 0 \\ 0 & 0 & m_a \end{pmatrix}. \tag{6.3}$$

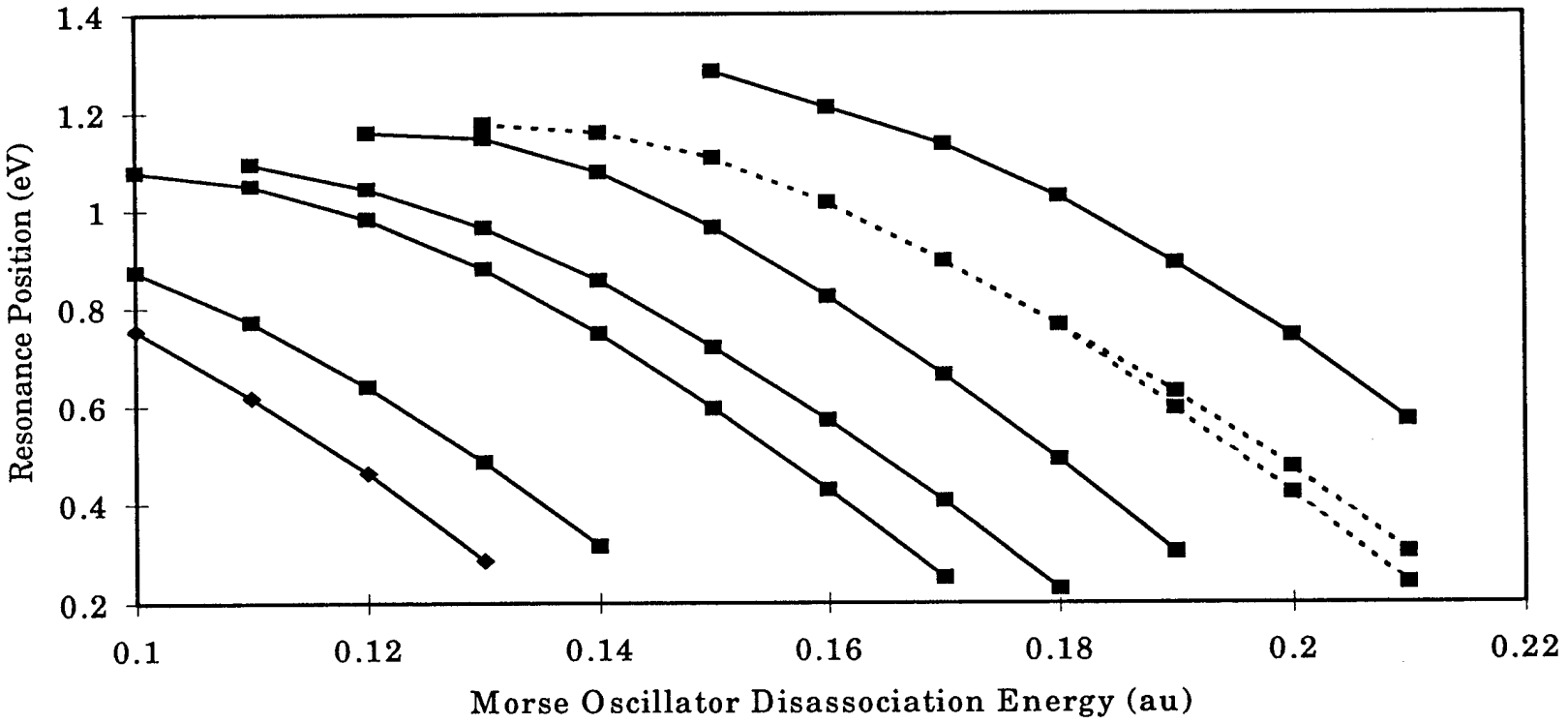

Figure 6.11 A sub-section of Figure 6.9 showing the position of S–matrix element resonances as a function of Morse oscillator disassociation energy. The curve represented with a dashed line is the bifurcation further analyzed in the text.

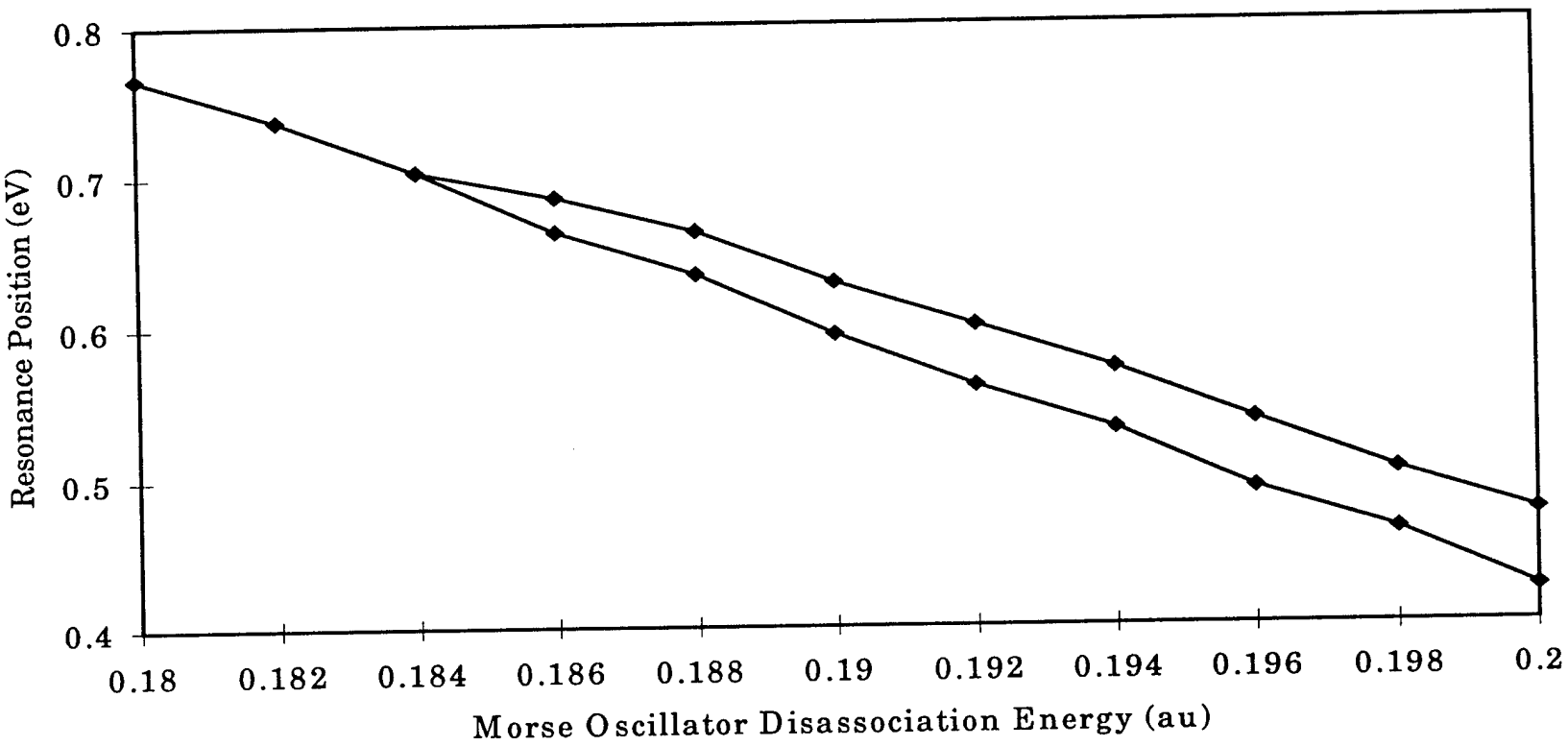

Figure 6.12 Position of a single S–matrix element resonance as a function of Morse oscillator disassociation energy. The resonance is initially degenerate with a bifurcation between 0.184 and 0.186 au breaking the degeneracy.

Diagonalizing the matrix $(\mathbf{M}^{-1}\mathbf{F})$ yields

$$\begin{pmatrix} \omega_0^2 & 0 & 0 \\ 0 & \omega_1^2 & 0 \\ 0 & 0 & \omega_2^2 \end{pmatrix} = \begin{pmatrix} 0 & 0 & 0 \\ 0 & \frac{K}{m_a} & 0 \\ 0 & 0 & K\frac{2m_a+m_b}{m_a m_b} \end{pmatrix}. \tag{6.4}$$

The normal mode associated with $\omega_0 = 0$ is translation. The normal mode associated with ω_1 is the symmetric stretch and the normal mode associated with ω_2 is the asymmetric stretch. The energy eigenvalues of the harmonic limit of the two coupled Morse oscillator potential are given by

$$E(n_1, n_2) = \hbar\omega_1\left(n_1 + \frac{1}{2}\right) + \hbar\omega_2\left(n_2 + \frac{1}{2}\right), \tag{6.5}$$

where n_1 and n_2 are the quantum numbers associated with the eigenstates (normal modes) whose frequencies are ω_1 and ω_2. n_1 and n_2 are integers and range from zero to infinity. For the LHL mass configuration, the energy eigenvalues associated with the frequencies are $\hbar\omega_1 = 1.36$ eV and $\hbar\omega_2 = 1.61$ eV. The 20 lowest energy eigenvalues are given in Table 6.2 with their associated quantum numbers. The spectrum of the energy eigenvalues is given in Figure 6.13. From the spectrum below 8 eV, the eigenstates of the harmonic limit can be grouped into singlets, doublets and triplets. However, the resonances in the S–matrix elements shown in Figures 6.1 and 6.8 do not line up with the spectrum shown in Figure 6.13, and there is no clear analytic connection between the resonances and the eigenstates of the harmonic limit. Graphically, at low values of dissociation energy, the resonances can be grouped as singlets and doublets. At higher dissociation energy, resonances can also be grouped into triplets. It is tempting to attribute the resonant multiplets to virtual states of the harmonic limit of the two coupled Morse oscillators. However, only qualitative similarities are observed and making such a connection between the virtual states of the harmonic limit and the resonances in Figures 6.1 and 6.8 is premature.

Table 6.2 Quantum numbers and energy eigenvalues of the 20 lowest eigenstates of the harmonic limit of the two coupled Morse oscillator potential for the LHL mass configuration.

n_1	n_2	Energy (eV)
0	0	1.485
1	0	2.845
0	1	3.095
2	0	4.205
1	1	4.455
0	2	4.705
3	0	5.565
2	1	5.815
1	2	6.065
0	3	6.315
4	0	6.925
3	1	7.175
2	2	7.425
1	3	7.675
0	4	7.925
5	0	8.285
4	1	8.535
3	2	8.785
2	3	9.035
1	4	9.285

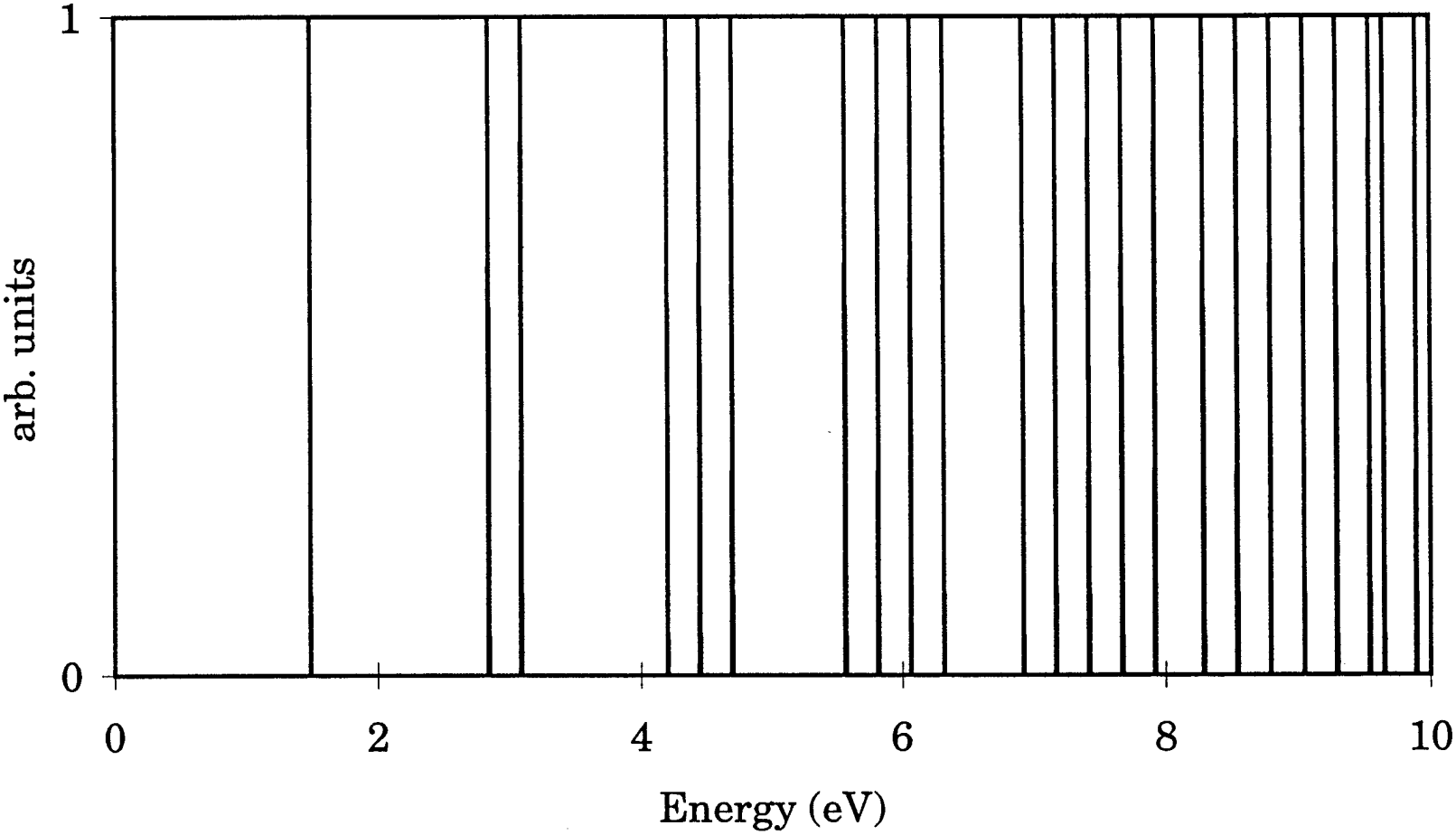

Figure 6.13 Energy of the eigenstates of the harmonic limit of the two coupled Morse oscillator potential for the LHL mass configuration.

6.3 *Resonances and kinetic coupling*

In the bond coordinate representation of the full scattering Hamiltonian, the kinetic energy operators in Equation 5.2 are coupled via

$$-\frac{\hat{P}_X \hat{P}_Y}{m_b}, \tag{6.6}$$

where $\hat{P}_j$ is the conjugate momentum operator in the j direction and m_b is the mass of atom B. In this analysis, the minus sign in front of the coupling term is replaced by a parameter which is varied from -1 to 0 in steps of 0.1 where the step size is arbitrary. The potential energy surface with a dissociation energy of 0.20 au was chosen for the analysis for the number of, and complex nature of, the resonances. Figures 6.14 and 6.15 illustrate the effect of kinetic coupling on S–matrix resonances. The complete set of S–matrix elements for kinetic energy coupling constants of –1 to 0 in steps of 0.1 are contained in Appendix D. As the kinetic coupling is reduced, the resonances labeled 1 in Figure 6.14, simply decrease in magnitude with decreasing coupling. The resonances labeled 2 both decrease in magnitude and coalesce into a single resonance. As expected, the probability of reaction where the two Morse oscillators are completely kinetically decoupled is zero as shown in Figure 6.15.[a]

6.4 *Absorbing boundary condition reflection S–matrix elements*

Similar to the analysis in Section 5.3, S–matrix elements were computed for absorbing boundary condition reflection for the reaction $A + BC\,(\nu = j) \rightarrow A + BC\,(\nu' = j)$, $j = 0, 1, 2$ for the LHL mass configuration and are shown in Figure 6.16. The probability of reflection for $\nu' \neq \nu$ is essentially zero. As seen in the MLM and HLH mass configurations, wave packets constructed from the $\nu = 0$ internal vibrational eigenstate are more likely to reflect than those constructed from the $\nu = 1$ and $\nu = 2$ eigenstates. However, the magnitude of the probability of reflection

[a]The labels 1 and 2 are purely arbitrary.

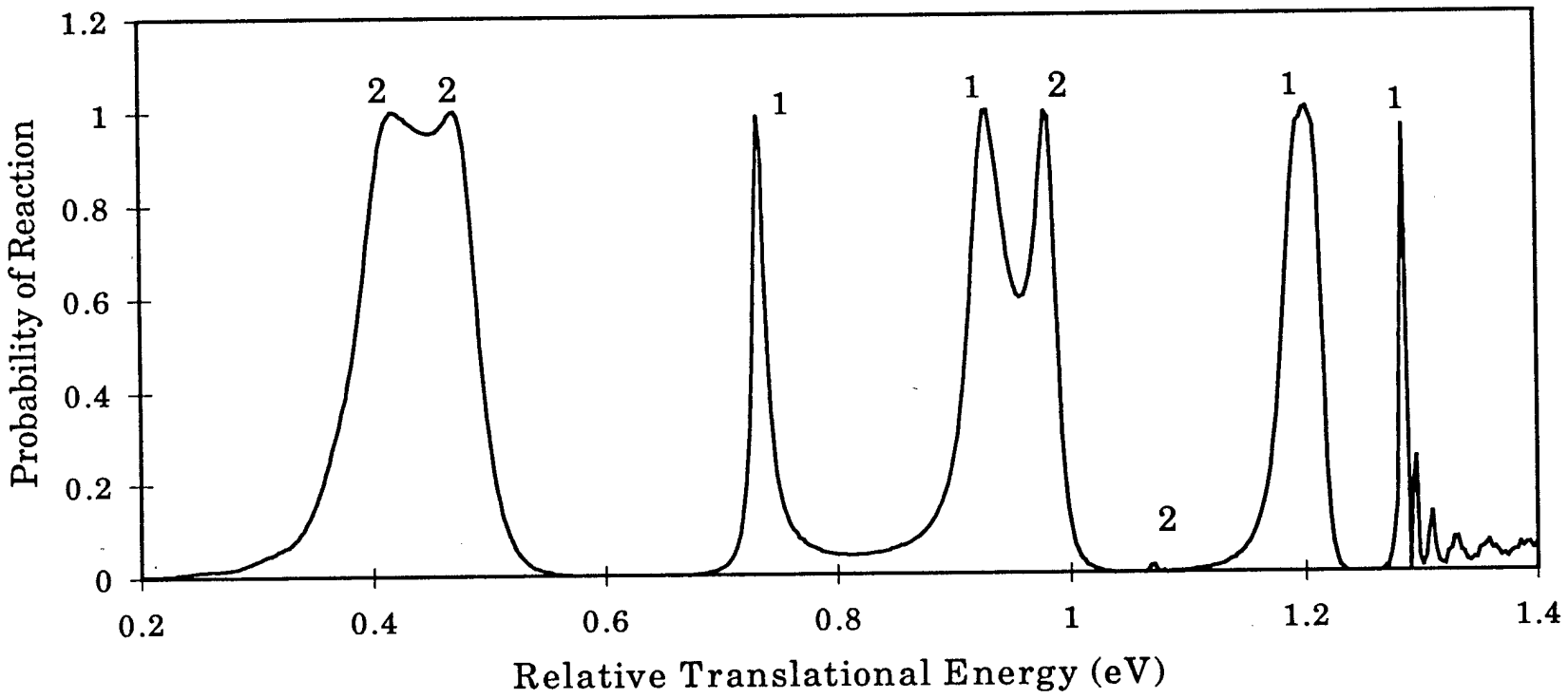

Figure 6.14 Probability of reaction for the two coupled Morse oscillator LHL mass configuration for the reaction $A+BC(v=0)\rightarrow AB(v'=0)+C$ where the dissociation energy is 0.20 au and the kinetic ernergy coupling constant is –1. The labels 1 and 2 are discussed in the text.

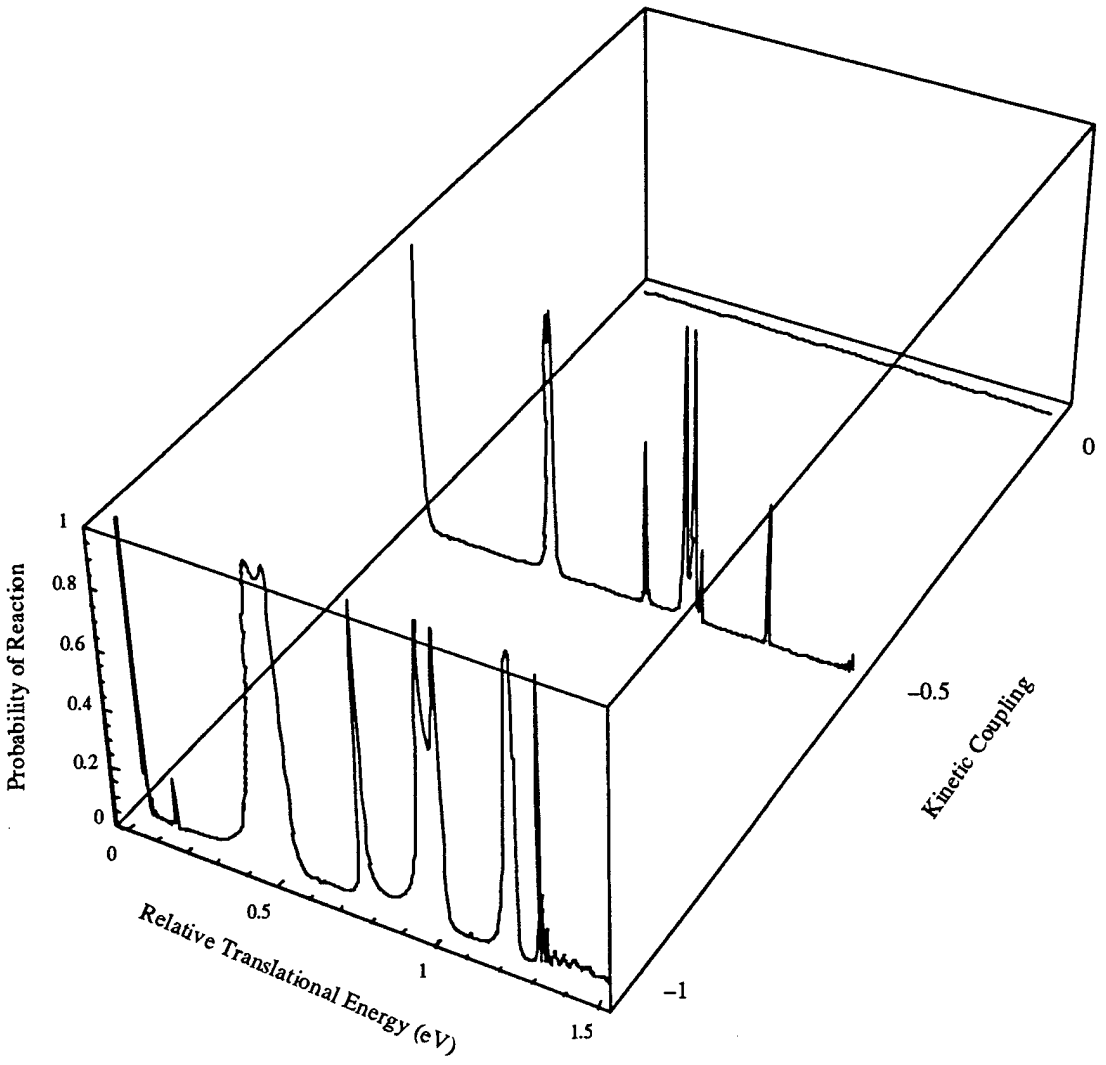

Figure 6.15 Probability of reaction for the two coupled Morse oscillator LHL mass configuration for the reaction $A + BC(0) \rightarrow AB(0) + C$ where the dissociation energy is 0.20 au. Probabilities are shown for kinetic energy coupling constants of –1, –0.5 and 0.

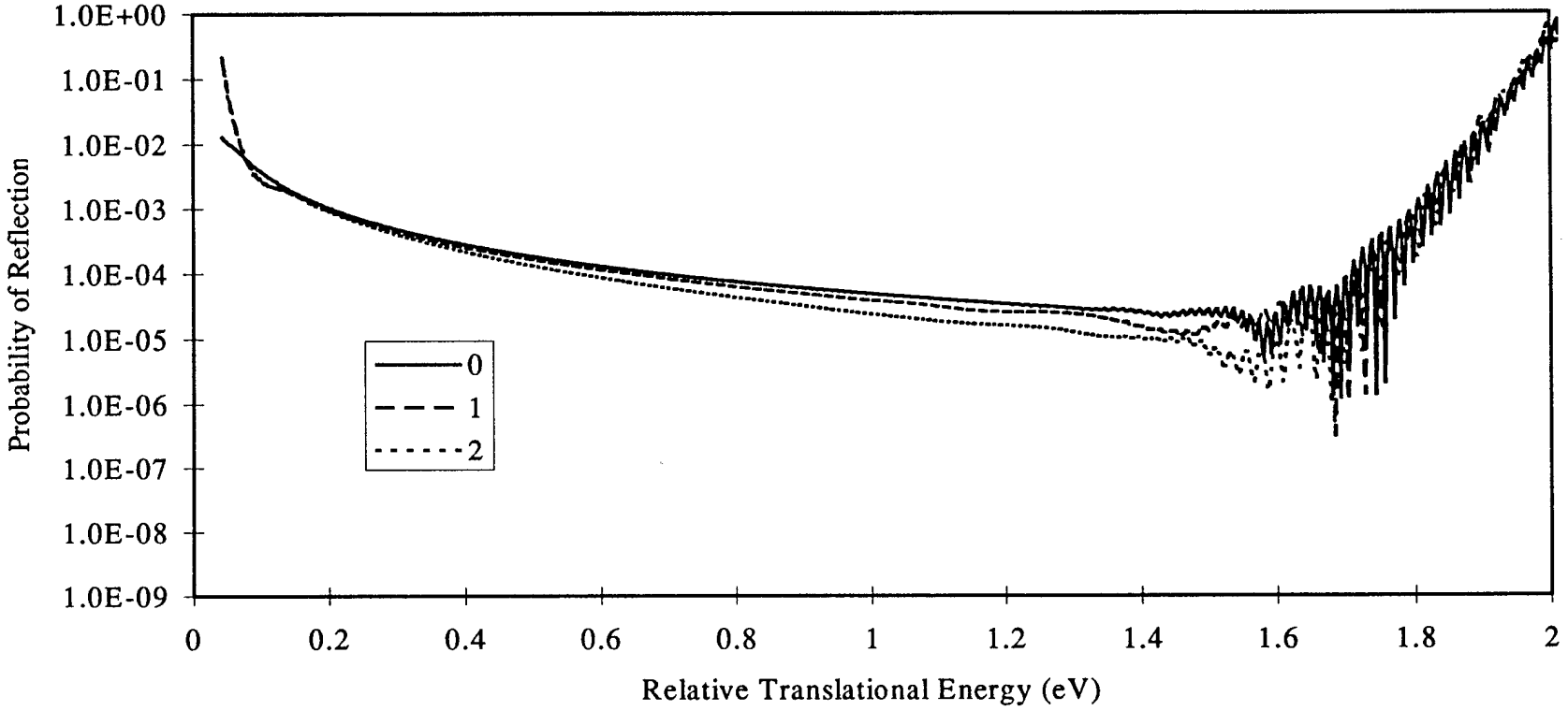

Figure 6.16 Probability of reflection for the reaction $A+BC(v=j) \rightarrow A+BC(v'=j)$, $j=0,1,2$ for the LHL mass configuration. The probability of reflection for $v \neq v'$ is essentially zero.

is not drastically reduced from the probability of reflection for the MLM or HLH cases.

The reason why the LHL mass configuration does not suffer from significant absorbing boundary condition reflection error is not attributable solely to the magnitude of absorbing boundary condition reflection. In order to investigate the reasons why absorbing boundary condition reflection error is significant in the LLL, MLM and HLH mass configurations and not the LHL mass configurations, consider the correlation function given by

$$C_{\gamma'\gamma}(t) = \langle \Psi_-^{\gamma'} | \exp\left(-i\frac{\hat{H}t}{\hbar}\right) | \Psi_+^{\gamma} \rangle. \tag{6.7}$$

The derivation of the formula for S-matrix elements in Appendix A and Chapter II uses a Hamiltonian that does not contain absorbing boundary conditions. With the application of absorbing boundary conditions, the formula for the correlation function changes,

$$C_{\gamma'\gamma}(t) = \langle \Psi_-^{\gamma'} | \exp\left\{\frac{-it}{\hbar}\left(\hat{H} - i\hat{V}_a\right)\right\} | \Psi_+^{\gamma} \rangle, \tag{6.8}$$

to include V_a the absorbing boundary condition potential. The wave packets $|\Psi\rangle$ can be expanded in terms of expansion coefficients and the eigenbasis of $\hat{H}$,

$$|\Psi_\pm^\xi\rangle = \int_{-\infty}^{+\infty} dk_\xi \eta_\pm(k_\xi) |k_\xi, \xi\pm\rangle. \tag{6.9}$$

Expanding the bra-ket in Equation 6.8 and using Equation 6.9, the result is

$$\begin{aligned} C_{\gamma'\gamma}(t) \;=\; & \int_{-\infty}^{+\infty} dk'_{\gamma'} \int_{-\infty}^{+\infty} dk_\gamma \eta_-^*\left(k'_{\gamma'}\right) \eta_+(k_\gamma) \\ & \times \langle k'_{\gamma'}, \gamma' - | \exp\left\{\frac{-it}{\hbar}\left(\hat{H} - i\hat{V}_a\right)\right\} | k_\gamma, \gamma + \rangle. \end{aligned} \tag{6.10}$$

We believe that the mixing of eigenstates of $\hat{H}$ by V_a in Equation 6.10 governs the absorbing boundary condition reflection error. However, the complex nature of the integrals in Equation 6.10 does not lend itself to deriving an absorbing potential which minimizes the error introduced by mixing the eigenstates of $\hat{H}$ and a solution to the problem of absorbing boundary condition reflection error is unknown at this point.

6.5 Summary

The light-heavy-light mass configuration of the two coupled Morse oscillators is qualitatively unaffected by absorbing boundary condition error. This can be seen in that changing the position of the absorbing boundary conditions does not affect the probability of reaction. This is in contrast to the results in Chapter V where the position of the absorbing boundary conditions greatly influence the resulting probability of reaction. One of the primary purposes of this study was to improve the efficiency of the computation of S–matrix elements. For the light-heavy-light mass configuration, the correlation function computation without absorbing boundary conditions, which yields good S–matrix elements, took approximately 55,000 seconds of CPU time. Applying absorbing boundary conditions, reduced the grid size by a factor of 16 yielding a factor of 29 reduction in the computation time for the correlation function. Again, the combination of absorbing boundary conditions with the channel packet method results in significant time savings as opposed to the channel packet method alone.

The effect of dissociation energy on the probability of reaction for the two coupled Morse oscillators can be investigated using the light-heavy-light mass configuration since it is not affected by absorbing boundary condition error. Qualitatively, the deeper the well in the interaction region, i.e. the higher the dissociation energy, the probability of reaction exhibits more resonances. The initial placement, energetically, of a resonance appears to be governed by an envelope shown in Figure 6.10.

Overall, the position of a resonance, as seen in Figure 6.11, as a function of dissociation energy exhibits the same overall shape. Figure 6.12 illustrates the breaking of a degenerate resonance between 0.184 and 0.186 au.

The virtual eigenstate of the harmonic limit of two coupled Morse oscillators can be determined. The energy spectrum of these states is shown in Figure 6.13. However, no clear analytic connection can be made between virtual eigenstates of the harmonic limit of the two coupled Morse oscillators and the resonances illustrated in Figures 6.1 and 6.8. The question of influence by the virtual states remains open.

The effect of kinetic coupling is also investigated using the light-heavy-light mass configuration. Figures 6.14 and 6.15 illustrate the effect of kinetic coupling on S–matrix resonances. As the kinetic coupling constant is reduced, so is the magnitude and number of S–matrix resonances. When the two Morse oscillators are completely uncoupled, the coupling constant is zero, the S–matrix elements are zero. This is expected since without any coupling there is no energy transfer between the two oscillators. For a tiny coupling constant, -0.1, there is only a slight possibility of reaction at a relative translation energy of approximately 0.5 eV. An analysis of S–matrix resonances divides the resonances into two types. One type simply decreases in magnitude with decreasing coupling. The other type concerns pairs of resonances that coalesce into a single degenerate resonance before their magnitude reaches zero with decreasing coupling.

VII. Conclusion

The calculation of S–matrix elements for quantum reactive scattering remains computationally intensive. We have developed a new method that dramatically improves efficiency for computing S–matrix elements by combining the channel packet method with absorbing boundary conditions. While absorbing boundary conditions have been used in the past for preventing edge of grid reflections, never before have they been used for the specific purpose of reducing the size of the grid used to perform the computations. The dramatic improvement in computational efficiency is achieved by exploiting the manner in which the channel packet method computes S–matrix elements. The channel packet method relies on computing two Møller states: one representing reactants and one representing products. The time dependent correlation function between the two Møller states is computed and used to calculate S–matrix elements. The formulation using two Møller states is exploited by individually propagating the Møller states on a small efficient grid by using absorbing boundary conditions to attenuate the evolving Møller states as they exit the interaction region of the potential. The attenuation of the evolving states prevents their reflecting from the edges of the much smaller grid. The Fourier transform of the correlation function is then used to compute S–matrix elements.

The one dimensional square well has an analytic solution for the S–matrix elements. S–matrix elements computed using the combination of the channel packet method with absorbing boundary conditions are in excellent agreement with the analytic solution. Two tests of convergence are used to demonstrate agreement with the analytic solution. First, it is important that a method not only converge but that it converge to the correct answer. In Figure 3.6, the solution computed using the channel packet method with absorbing boundary conditions is converging towards the analytic solution. Second, the order of convergence provides a test of efficiency for the channel packet method with absorbing boundary conditions. The order of

convergence can be computed by determining the slope of a line in a log-log plot where the changes in a given parameter, for example the spatial grid resolution, are plotted against the relative error. For changes in the spatial grid, the channel packet method with absorbing boundary conditions converges with an order of 3. For changes in the temporal grid, the order is 4. These orders of convergence are illustrated in Figures 3.8 and 3.9. These convergence tests validate the application of absorbing boundary conditions with the channel packet method to one dimensional quantum reactive scattering.

While absorbing boundary conditions are extensively used, very little information is available about their behavior and possible influence on S–matrix elements. Quantum scattering for a simple one dimensional potential consisting of a Gaussian well bounded by symmetric Gaussian barriers is used to investigate the behavior of absorbing boundary conditions when applied to the channel packet method. The efficiency of the combination is once again demonstrated when quasi-bound states are trapped by the barriers around the Gaussian well. Without absorbing boundary conditions, the grid would have to be large enough to support the evolving Møller state until the quasi-bound state has completely exited the interaction region. For example, when the barriers are 0.05 au high, without absorbing boundary conditions, the spatial grid would have to be 21 times larger in order to accommodate the evolving wave packet until the quasi-bound state has completely exited the interaction region. The resulting large grid is computationally prohibitive. The investigation into the effects of absorbing boundary conditions begins with conditions that are too steep. Absorbing boundary conditions that are too steep will reflect the evolving Møller state back into the interaction region thereby introducing error into the correlation function. The resulting S–matrix elements exhibit near periodic oscillations and probabilities of transmission greater than one. Similarly, absorbing boundary conditions which are too shallow will not fully attenuate the evolving Møller state and the periodic boundary conditions imposed by the fast Fourier transforms used

in the propagation allow the Møller state to wrap around the grid. This introduces errors into the correlation function and the resulting S–matrix elements again exhibit nearly periodic oscillations as well as probabilities of transmission greater than one. Finally, the sudden onset of the absorbing boundary conditions can introduce small errors into the correlation function. The resulting S–matrix elements exhibit only minor oscillations about the correct answer.

Quantum reactive scattering for the collinear $H + H_2$ reaction has been extensively studied using a variety of methods and provides an excellent benchmark for testing the combination of the channel packet method with absorbing boundary conditions. The results are in agreement with previous calculations with the L_2 norm error between the channel packet method without absorbing boundary conditions and the channel packet method with absorbing boundary conditions is on the order of 6×10^{-3}. This is a small error in comparison to the dramatic reduction in computational effort the combination of the channel packet method with absorbing boundary conditions produces. The grid for computing the correlation function was reduced by a factor of 16, from 256×256 to 64×64. Overall, the result of the grid reduction was a significant order of magnitude improvement in the time necessary to compute the correlation function.[41]

The collinear $H + H_2$ reaction was also used to demonstrate the convergence of the channel packet method with absorbing boundary conditions. Figure 4.11 illustrates the convergence of channel packet method with absorbing boundary conditions' solution to the accepted solution based on previous work.[25,31–35,39] Again, the order of convergence for the channel packet method with absorbing boundary conditions is tested for changes in the temporal resolution. As in the one dimensional case, the order of convergence is 4. This is illustrated in Figure 4.12.

A simple system of two coupled Morse oscillators is used to investigate the effects of potential well depth and reaction masses on quantum reactive scattering for two dimensional potentials where there is a barrierless well in the interaction

region. However, S–matrix elements for the light-light-light, medium-light-medium and heavy-light-heavy mass configurations suffer from non- trivial errors introduced by absorbing boundary condition reflection. While qualitative information about the S–matrix elements may be gleaned, the exact nature of the S–matrix elements remains obscured by the error introduced by absorbing boundary conditions reflection.

Unlike the previous three mass configurations, the light-heavy-light mass configuration of the model two coupled Morse oscillator potential does not suffer from significant absorbing boundary conditions reflection error. The exact relationship between the kinetic, potential, and absorbing boundary conditions terms in the Hamiltonian that leads to only negligible absorbing boundary condition reflection is not clear. However, the influence of well depth and kinetic coupling on quantum reactive scattering can be investigated using the light-heavy-light configuration since it does not suffer from absorbing boundary condition reflection error. Increasing well depth leads to a greater number of and more complex resonances in the S–matrix elements. However, there is no clear analytic connection between the virtual states of the harmonic limit of the two coupled Morse oscillators and the S–matrix element resonances.

7.1 Further research

There is a great deal of research on two dimensional quantum reactive scattering that remains to be done. The work presented here provides a firm foundation for further research. As we saw in the one dimensional case, potential wells with barriers tend to trap long-lived, quasi-bound states. These states may take quite some time to completely exit the interaction region. Methods that do not take advantage of absorbing boundary conditions would require excessively large grids to support the evolving wave packet until the quasi-bound state completely exits the interaction region. In one dimension, the application of absorbing boundary

conditions eliminated the need for such a large grid. However, this has yet to be demonstrated for two dimensions.

There is also the research into which potentials the channel packet method with absorbing boundary conditions is applicable. The combined method apparently fails to work for potential surfaces where there is a well in the interaction region and the scattering atoms are in anything other than a light-heavy-light mass configuration. It appears that reflection from the absorbing boundary conditions are the culprit though the mixing of eigenstates of the full Hamiltonian as in Equation 6.10.

Finally, there is the extension of the channel packet method with absorbing boundary conditions to scatter in three dimensions. Current research in three dimensional reactive scattering is limited to very simple reactions like $H + H_2$. While computational power continues to increase, the current methods used in three dimensional scattering again rely on large grids which are inefficient.

Appendix A. Derivation of the formula for scattering matrix elements

The formula in the channel packet method for scattering matrix elements given in Equation 2.30 is derived from the orthogonality relationship

$$\begin{aligned} \langle k'_{\gamma'}, \gamma' - | k_\gamma, \gamma \rangle &= \langle k'_{\gamma'}, \gamma' | \hat{\Omega}_-^{\gamma'\dagger} \hat{\Omega}_+^{\gamma} | k_\gamma, \gamma \rangle \\ &= \langle k'_{\gamma'}, \gamma' | \hat{S} | k_\gamma, \gamma \rangle \\ &= \frac{\hbar \sqrt{|k'_{\gamma'}||k_\gamma|}}{\sqrt{\mu_{\gamma'}\mu_\gamma}} \delta(E - E) S^{\gamma'\gamma}_{k'_{\gamma'} k_\gamma}, \end{aligned} \tag{A.1}$$

Inverting the final line in Equation A.2 shows that all that is necessary to compute S-matrix elements is to evaluate the scalar product

$$\langle k'_{\gamma'}, \gamma' - | k_\gamma, \gamma + \rangle. \tag{A.2}$$

Evaluating Equation A.2 begins by defining the state $|A_E^\gamma +\rangle$ as the Fourier transform of the time evolution of the reactant Møller state. The state $|A_E^\gamma +\rangle$ is given by

$$|A_E^\gamma +\rangle = \int_{-\infty}^{+\infty} dt \exp\left(i\frac{Et}{\hbar}\right) \exp\left(-i\frac{\hat{H}t}{\hbar}\right) |\Psi_+^\gamma\rangle \tag{A.3}$$

Substituting the expansion of $|\Psi_+^\gamma\rangle$ in terms of $|k_\gamma, \gamma\rangle$ given in Equation 2.22 and expanding $\hat{H}$ in terms of T and V gives

$$|A_E^\gamma +\rangle = \int_{-\infty}^{+\infty} dk_\gamma \eta^+(k_\gamma) |k_\gamma, \gamma\rangle \int_{-\infty}^{+\infty} dt \exp\left(-i\frac{T_\gamma + V_\gamma}{\hbar}\right) \exp\left(i\frac{Et}{\hbar}\right). \tag{A.4}$$

Now consider the second integral in Equation A.4. The integral of two complex exponentials yields a delta function given by

$$\int_{-\infty}^{+\infty} dt \exp\left(-i\frac{T_\gamma + V_\gamma}{\hbar}\right)\exp\left(i\frac{Et}{\hbar}\right) = 2\pi\delta\left(\frac{1}{\hbar}T_\gamma + \frac{1}{\hbar}E_\gamma - \frac{1}{\hbar}T'_\gamma - \frac{1}{\hbar}E_\gamma\right)$$
$$= 2\pi\delta\left\{\frac{\hbar}{2\mu_\gamma}\left(k_\gamma^2 - k_\gamma'^{\,2}\right)\right\}, \qquad \text{(A.5)}$$

where the substitution

$$T_\gamma = \frac{\hbar^2 k_\gamma^2}{2\mu_\gamma} \qquad \text{(A.6)}$$

has been used.

Two more properties of delta functions are used to simplify Equation A.5.

$$\delta\left(\frac{1}{\xi}n\right) = \xi\delta(n) \qquad \text{(A.7)}$$

and

$$\delta\left(a^2 - b^2\right) = \frac{1}{2|b|}[\delta(a-b) + \delta(a+b)] \qquad \text{(A.8)}$$

reduce the complexities in Equation A.5 to

$$\int_{-\infty}^{+\infty} dt \exp\left(-i\frac{T_\gamma + V_\gamma}{\hbar}\right)\exp\left(i\frac{Et}{\hbar}\right) = \frac{2\pi\mu_\gamma}{\hbar|k_\gamma|}[\delta\left(k'_\gamma - k_\gamma\right) + \delta\left(k'_\gamma + k_\gamma\right)]. \qquad \text{(A.9)}$$

The two delta functions in Equation A.9 reduce the integral over dk_γ in Equation A.4 to a simple sum given by

$$|A_E^\gamma +\rangle = \left(\frac{2\pi\mu_\gamma}{\hbar|k_\gamma|}\right)[\eta_+(+k_\gamma)\,|+k_\gamma, \gamma+\rangle + \eta_+(-k_\gamma)\,|-k_\gamma, \gamma+\rangle], \qquad \text{(A.10)}$$

where the $\pm$ in front of the k_γ explicitly labels positive $(+)$ and negative $(-)$ momenta.

Evaluating the scalar product $\langle \Psi_-^{\gamma'} | A_E^{\gamma} + \rangle$ where Equation 2.22 is used to expand $|\Psi_-^{\gamma'}\rangle$ in terms of $|k'_{\gamma'}, \gamma'\rangle$ to obtain S–matrix elements leads to

$$\begin{aligned}\langle \Psi_-^{\gamma'} | A_E^{\gamma} + \rangle &= \frac{2\pi\mu_\gamma}{\hbar|k_\gamma|} \int_{-\infty}^{+\infty} dk'_{\gamma'} [\eta_-^* \left(k'_{\gamma'}\right) \eta_+ \left(+k_\gamma\right) \langle k'_{\gamma'}, \gamma' - | + k_\gamma, \gamma + \rangle \\ &\quad + \eta_-^* \left(k'_{\gamma'}\right) \eta_+ \left(-k_\gamma\right) \langle k'_{\gamma'}, \gamma' - | - k_\gamma, \gamma + \rangle]. \end{aligned} \tag{A.11}$$

The orthogonality relationship in Equation 2.24 reduces the integral in Equation A.11 to

$$\begin{aligned}\langle \Psi_-^{\gamma'} | A_+^{\gamma} (E) \rangle &= \frac{2\pi\sqrt{\mu_\gamma \mu_{\gamma'}}}{\hbar\sqrt{|k'_{\gamma'}||k_\gamma|}} [\eta_-^* \left(+k'_{\gamma'}\right) \eta_+ \left(+k_\gamma\right) S^{\gamma'\gamma}_{+k'_{\gamma'}+k_\gamma} \\ &\quad + \eta_-^* \left(+k'_{\gamma'}\right) \eta_+ \left(-k_\gamma\right) S^{\gamma'\gamma}_{+k'_{\gamma'}-k_\gamma} \\ &\quad + \eta_-^* \left(-k'_{\gamma'}\right) \eta_+ \left(+k_\gamma\right) S^{\gamma'\gamma}_{-k'_{\gamma'}+k_\gamma} \\ &\quad + \eta_-^* \left(-k'_{\gamma'}\right) \eta_+ \left(-k_\gamma\right) S^{\gamma'\gamma}_{-k'_{\gamma'}-k_\gamma}]. \end{aligned} \tag{A.12}$$

The remaining derivation follows Equation 2.28 on page 2–10.

Appendix B. Jacobi-to-bond transformation for momentum

In the transformation from the Jacobi representation to the bond representation, the momenta are no longer separable. The transformation from Jacobi coordinates to bond coordinates is given by

$$\begin{pmatrix} r_\alpha \\ R_\alpha \end{pmatrix} = \begin{pmatrix} 1 & \phi \\ 0 & 1 \end{pmatrix} \begin{pmatrix} X \\ Y \end{pmatrix}, \tag{B.1}$$

where ϕ is the mass related factor given by

$$\phi = \frac{m_c}{m_b + m_c}. \tag{B.2}$$

This transformation is for the $A + BC$ channel where r_α is the distance between the masses in the diatom BC and R_α is the distance between the atom A and the center-of-mass of the diatom. The derivation of the momentum transformation is also for the $A + BC$ channel. For the $AB + C$ channel, the derivations and transformations are similar.

For calculating the momentum transformation, the starting point is the Lagrangian formulation

$$L = T - V, \tag{B.3}$$

where L is the Lagrangian, T is the kinetic energy and V is the potential energy. For the quantum reactive scattering studied in this research project, the potential V is independent of the velocity and it is omitted from the rest of the discussion of the transformation. The conjugate momenta P_i is derived from the Lagrangian via

$$P_i = \frac{\partial L}{\partial q_i}, \tag{B.4}$$

where q_i is the time derivative of the coordinate q. In Jacobi coordinates, the Lagrangian for a free particle

$$L = \frac{1}{2m_a} P_R^2 + \frac{1}{2\mu_r} P_r^2, \tag{B.5}$$

where m_a is the mass of atom a, μ_r is the reduced mass given by

$$\mu_r = \frac{m_b m_c}{m_b + m_c}, \tag{B.6}$$

and P_R and P_r are the non-relativistic momenta given by

$$P_R = m_a R \text{ and } P_r = \mu_r r. \tag{B.7}$$

Combining together equations B.5 and B.7 gives

$$L = \frac{1}{2} m_a R^2 + \frac{1}{2} \mu_r r^2. \tag{B.8}$$

Now, using the coordinate transformations from equation B.2 together with equation B.8, yields

$$L = \frac{1}{2} m_a \left(X + \phi Y\right)^2 + \frac{1}{2} \mu_r Y^2. \tag{B.9}$$

Using the relationship in equation B.4, the conjugate momenta P_X and P_Y are given by

$$P_X = \frac{\partial L}{\partial X} = \frac{1}{2} m_a \left(2X + 2\phi Y\right) \tag{B.10}$$

$$P_Y = \frac{\partial L}{\partial Y} = \frac{1}{2} m_a \left(2\phi X + 2Y\right) + \mu_r Y. \tag{B.11}$$

Combining terms together with the transformation in equation B.2 yields the final transformation,

$$P_X = m_a R \tag{B.12}$$

$$P_Y = m_a \phi R + r\left(m_a + \mu_r - m_a \phi^2\right). \tag{B.13}$$

In the $A + BC$ channel, P_X may be interpreted as the relative momentum. However, the interpretation of P_Y is clouded by mixing between relative and internal momenta.

Appendix C. Code overview

The code implementing the application of the channel packet method together with absorbing boundary conditions to quantum scattering in one and two dimensions is briefly overviewed here. The code is written in FORTRAN77 with extensions made available by the Silicon Graphics compiler.

The fast Fourier transform (FFT) used throughout this code is the Temperton FFT written by the CECAM group.[55] The two dimensional front end to the FFT was written by the author. The original two–dimensional code was written by Dr. David Weeks during a post-doctoral fellowship at Notre Dame University under the direction of Dr. David Tannor and was altered to include the application of absorbing boundary conditions by the author. Both the one and two dimensional codes rely upon the use of individual modules of code compiled into a single executable using the Unix **make** command. The initialization of the code variables is done using a header file and all variables are common. No screen input is required as the input data is contained in a data file read into the program at the start.

C.1 One dimensional code

The code implementing the application of the channel packet method together with absorbing boundary conditions to quantum scattering in one dimension was written by the author. The module titles are in **boldface** with a brief explanation of its function.

1DFFT.f: This module contains the Temperton FFT and the initialization modules for the FFT.

1DScatter.h: Header file containing all the variables used in the program. All the variable are common.

1DScatter.f: Main program file which calls each of the modules in turn.

1DVariables.f: This module reads in the input data file containing the grid and wave packet initialization data.

1DGrid.f: This module creates the coordinate and momentum representation grids.

1DWave.f: This module computes the initial wave packets.

1DPotential.f: This module creates the potential array based on the coordinate grid.

1DMatrix.f: This module implements the split-operator array representation of the full scattering Hamiltonian using the coordinate and momentum grids together with the potential array. It is here that absorbing boundary conditions are introduced into the Hamiltonian.

1DNuscreen.f and **1DGraphs.f**: The first module initializes the graphics screen and the second module draws to the screen using the OpenGL libraries on a Silicon Graphics workstation. The modules are specific to the Silicon Graphics operating system and are not for use on any other platform.

1DReactant.f: This module computes the reactant Møller state in the manner outlined in section 3.1.2. On a Silicon Graphics workstation, the evolving wave packet can be displayed on the screen through the **1DGraphs.f** module.

1DProduct.f: This module computes the product Møller state in the manner outlined in section 3.1.2. On a Silicon Graphics workstation, the evolving wave packet can be displayed on the screen through the **1DGraphs.f** module.

1DNuWay.f: This module propagates the product Møller state forwards and backwards in time calculating the correlation function at every step. On a Silicon Graphics workstation, the evolving wave packet can be displayed on the screen through the **1DGraphs.f** module.

1DSmatrix.f: This module computes the S–matrix elements according to equation 2.29. The module **1DFTCR.f** actually computes the discrete Fourier trans-

form of the correlation function. The resulting S–matrix elements are written to a file and the program terminates.

C.2 Two dimensional code

The calculation of S–matrix elements for two dimensional reactive quantum scattering is actually done using three separate codes: Møller state calculation, correlation function calculation and S–matrix calculation. The code computing the Møller states remains unaltered from Dr. Weeks' original work. The code computing the correlation function is based on Dr. Weeks' original work but altered to include absorbing boundary conditions. The code computing S–matrix elements was written by the author for this project.

C.2.1 Møller state calculation code. The module titles are in **boldface** with a brief explanation of its function.

TemptFFT.f: This module contains the Temperton FFT and the initialization modules for the FFT.

2DScatter.h: Header file containing all the variables used in the program. All the variable are common.

2DScatter.f: Main program file which calls each of the modules in turn.

2DInitVar.f: This module reads in the input data file containing the grid and wave packet initialization data.

2DInitGrid.f: This module creates the coordinate and momentum representation grids.

2DPotential.f: This module creates the potential array based on the coordinate grid. This module calls another module that contains the code for the potential energy surface. The collinear $H + H_2$ potential energy surface is contained in the

module **hh2pot.f** and the two coupled Morse oscillator potential energy surface is contained in the module **morsepot.f**.

2DInitWave.f: This module computes the initial wave packets which is more complicated in the 2D case. At each grid point, depending on the channel, the coordinates are transformed into the appropriate set of Jacobi coordinates. The Jacobi coordinates are then passed to a module which computes the internal vibrational eigenstate. For the collinear $H + H_2$ potential energy surface, the internal vibrational eigenstates are not analytic. The internal Hamiltonian is represented in a basis of Morse oscillator functions and then diagonalized. The internal vibrational eigenstate is computed from a linear combination of Morse oscillator functions according to the transformation matrix which diagonalized the internal Hamiltonian. For the two coupled Morse oscillator potential energy surface, the internal vibrational eigenstates are known analytically and the matrix representation and diagonalization are omitted. In either case, it is important to note that the code numbers the internal eigenstates starting at 1 and not 0. The initial wave packet is constructed from a direct product of the internal vibrational eigenstate and a linear combination of eigenstates of the relative Hamiltonian in Jacobi coordinates. It is then propagated analytically to $\pm\tau$ and then transformed into bond coordinates.

2DMatrix.f: This module implements the split-operator array representation of the full scattering Hamiltonian using the coordinate and momentum grids together with the potential energy surface.

2DSplitOp.f: This module computes the Møller state from the initial wave packet using the split operator approach. At the end of the propagation, the Møller state is written to a file and the program terminates.

C.2.2 Correlation function calculation code. The module titles are in **boldface** with a brief explanation of its function. The overviews of the mod-

ules **TemptFFT.f 2DScatter.h, 2DScatter.f, 2DInitVar.f, 2DInitGrid.f** and **2DPotential.f** remain unchanged from the previous section.

2DInitWave.f: This module simply reads in the reactant and product Møller states.

2DMatrix.f: This module implements the split-operator array representation of the full scattering Hamiltonian using the coordinate and momentum grids together with the potential energy surface. This code has been altered to include absorbing boundary conditions.

2DSplitOp.f: This module propagates the reactant Møller state forwards and backwards in time using the split operator approach. At each time step, the correlation function is computed and stored. At the end of the propagations, the correlation function is written to file and the program terminates.

C.2.3 S-matrix calculation code. The module titles are in **boldface** with a brief explanation of its function.

2DScatter.h: Header file containing all the variables used in the program. All the variable are common.

2DSmatrix.f: This is the main module. It first calls **2DInitVar.f** to input all the necessary information. The main body of code computes the expansion coefficients necessary to normalize the S-matrix elements, computes the discrete Fourier transform of the correlation function and calculates and writes to a file the S-matrix elements.

2DInitVar.f: This module not only reads in the initial grid and wave packet conditions, it also reads in the correlation function.

Appendix D S–matrix elements for two coupled Morse oscillators in a light-heavy-light mass configuration

The following 16 plots illustrate the probability of reaction for two coupled Morse oscillators in a light-heavy-light mass configuration where the well depth, i.e. dissociation energy, is changed from 0.11 au to 0.26 au in steps of 0.01 au.

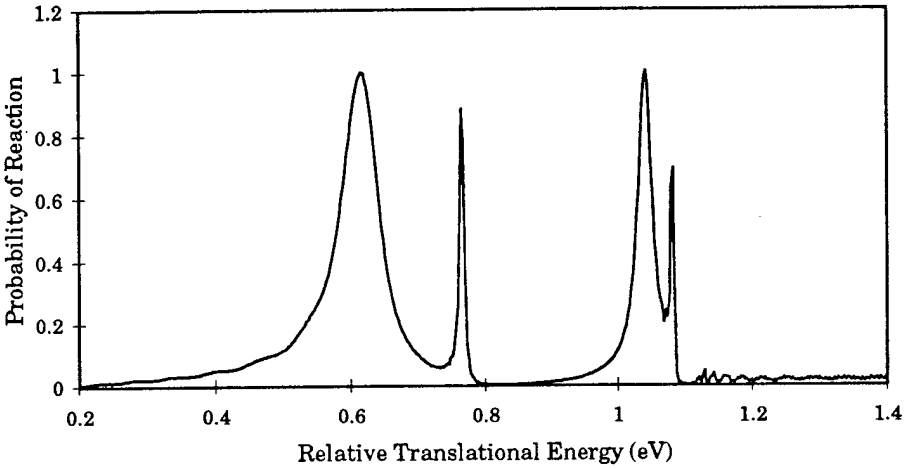

Figure D.1 Absolute value of the correlation function for the two coupled Morse oscillator LHL mass configuration for the reaction $A + BC(v = 0) \rightarrow AB(v' = 0) + C$ where the disassociation energy is 0.11 au.

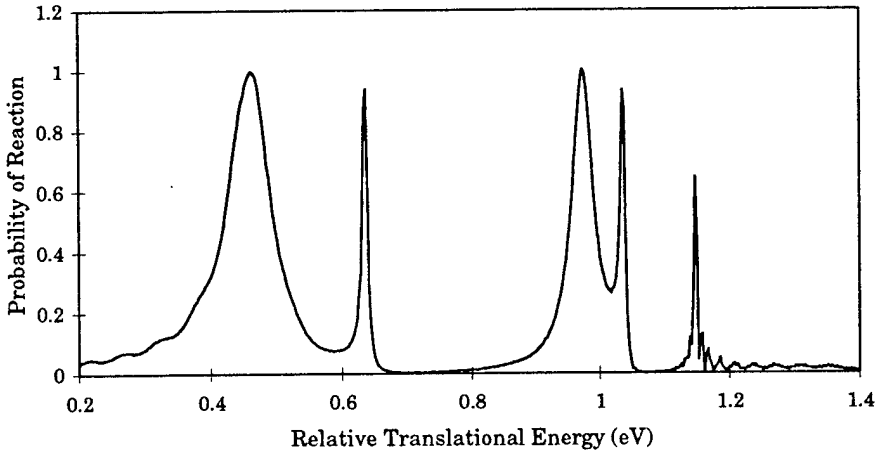

Figure D.2 Absolute value of the correlation function for the two coupled Morse oscillator LHL mass configuration for the reaction $A + BC(v = 0) \rightarrow AB(v' = 0) + C$ where the disassociation energy is 0.12 au.

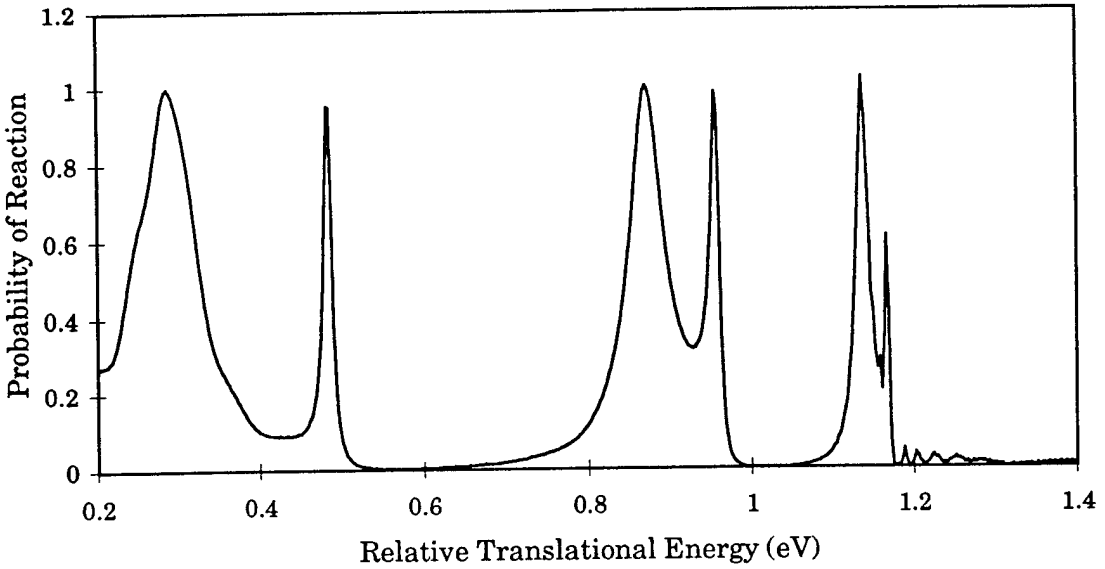

Figure D.3 Probability of reaction for the two coupled Morse oscillator LHL mass configuration for the reaction $A + BC(v = 0) \rightarrow AB(v' = 0) + C$ where the disassociation energy is 0.13 au.

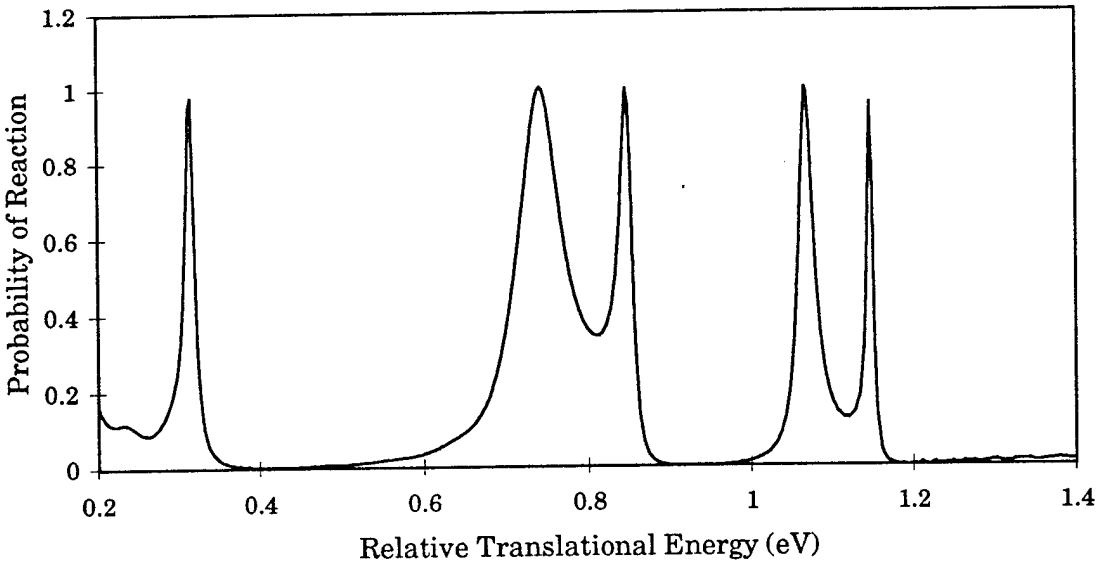

Figure D.4 Probability of reaction for the two coupled Morse oscillator LHL mass configuration for the reaction $A + BC(v = 0) \rightarrow AB(v' = 0) + C$ where the disassociation energy is 0.14 au.

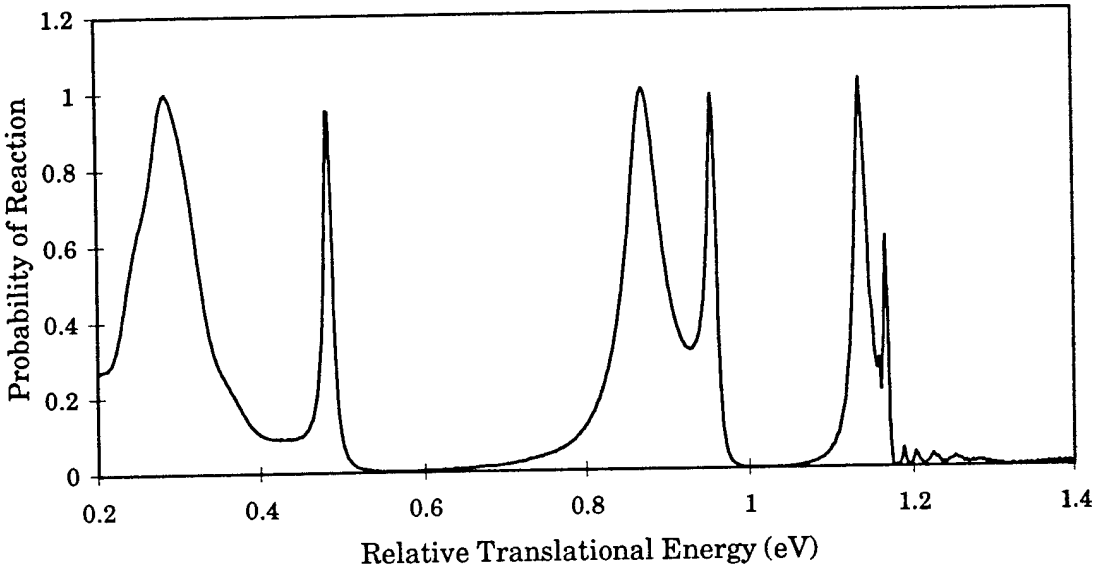

Figure D.5 Probability of reaction for the two coupled Morse oscillator LHL mass configuration for the reaction $A + BC(v = 0) \rightarrow AB(v' = 0) + C$ where the disassociation energy is 0.15 au.

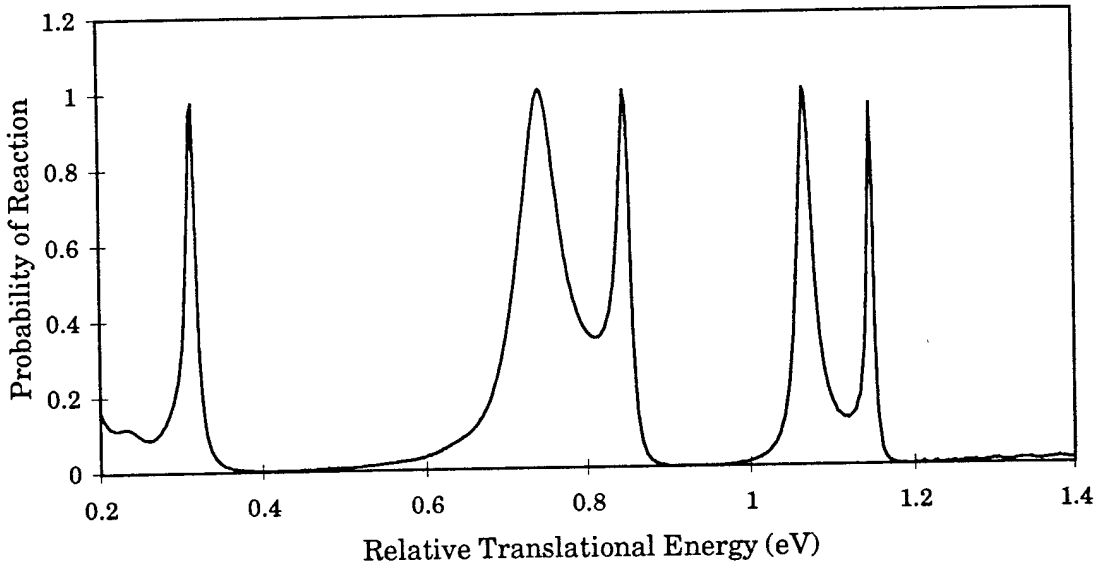

Figure D.6 Probability of reaction for the two coupled Morse oscillator LHL mass configuration for the reaction $A + BC(v = 0) \rightarrow AB(v' = 0) + C$ where the disassociation energy is 0.16 au.

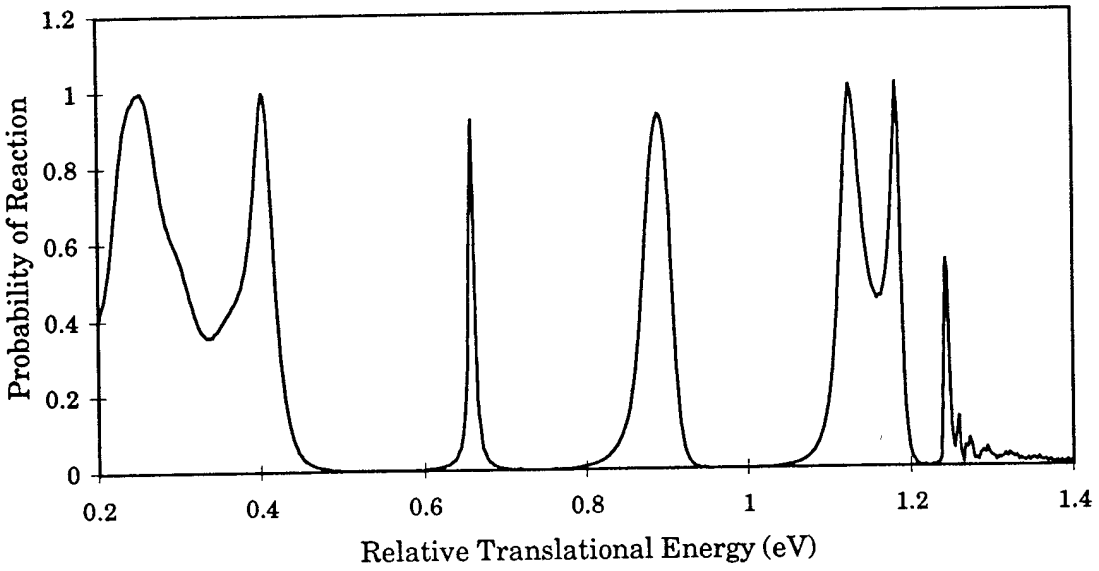

Figure D.7 Probability of reaction for the two coupled Morse oscillator LHL mass configuration for the reaction $A + BC(v = 0) \rightarrow AB(v' = 0) + C$ where the disassociation energy is 0.17 au.

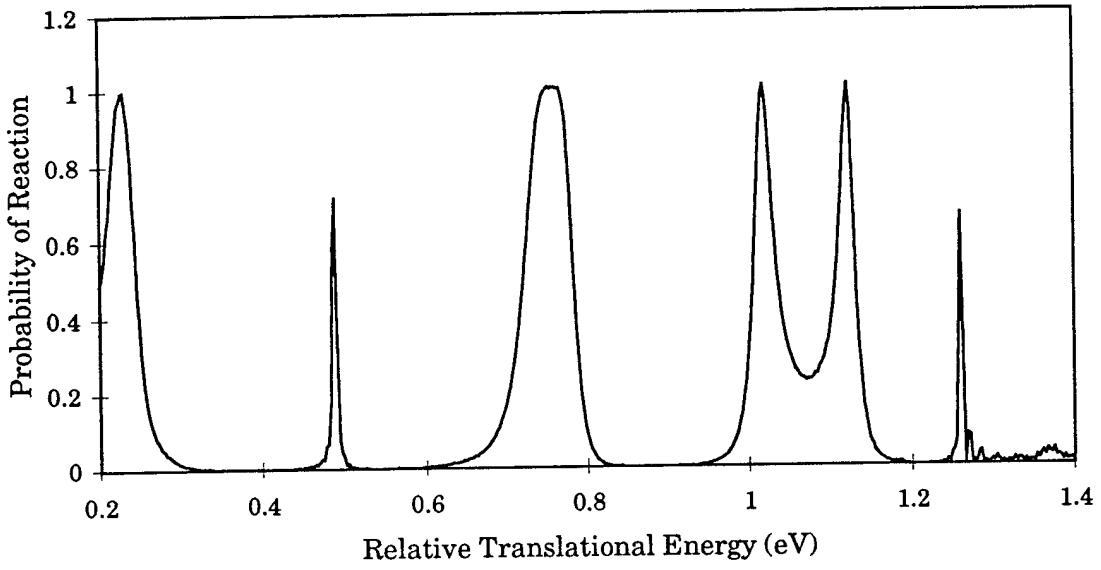

Figure D.8 Probability of reaction for the two coupled Morse oscillator LHL mass configuration for the reaction $A + BC(v = 0) \rightarrow AB(v' = 0) + C$ where the disassociation energy is 0.18 au.

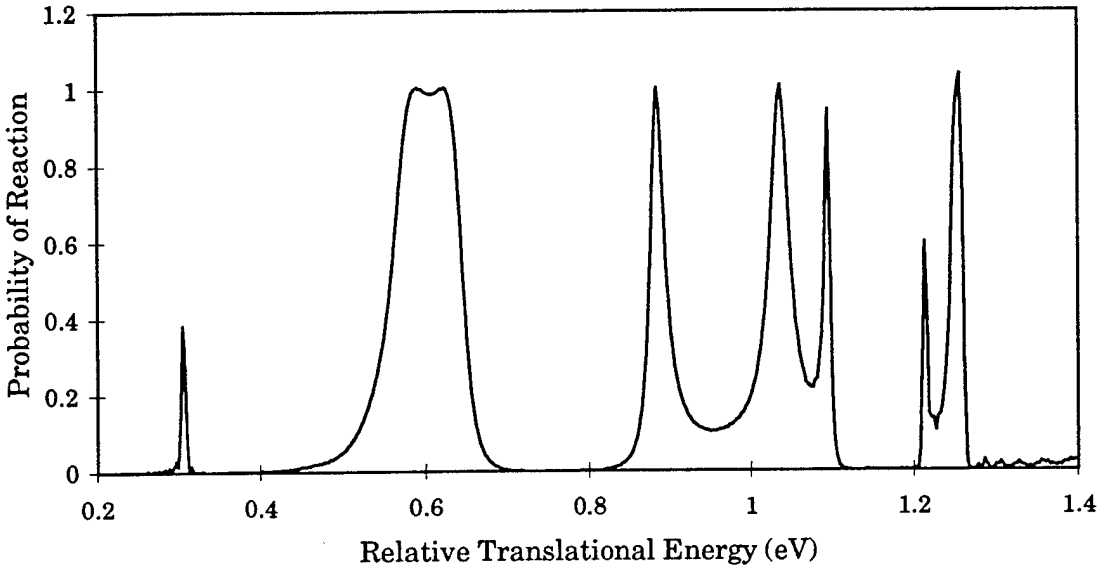

Figure D.9 Probability of reaction for the two coupled Morse oscillator LHL mass configuration for the reaction $A + BC(v = 0) \rightarrow AB(v' = 0) + C$ where the disassociation energy is 0.19 au.

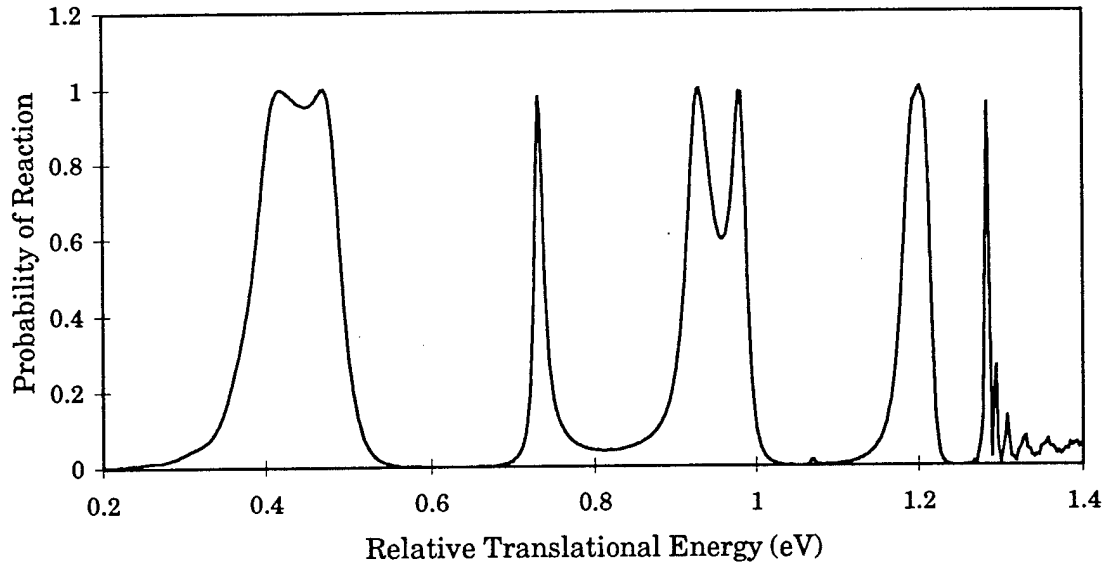

Figure D.10 Probability of reaction for the two coupled Morse oscillator LHL mass configuration for the reaction $A + BC(v = 0) \rightarrow AB(v' = 0) + C$ where the disassociation energy is 0.20 au.

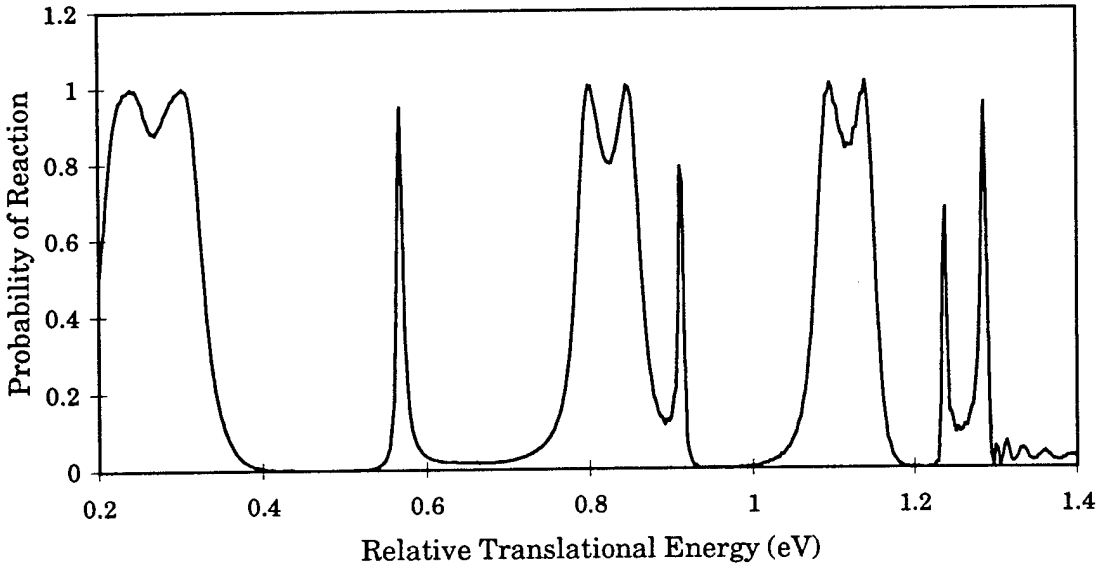

Figure D.11 Probability of reaction for the two coupled Morse oscillator LHL mass configuration for the reaction $A + BC(v = 0) \rightarrow AB(v' = 0) + C$ where the disassociation energy is 0.21 au.

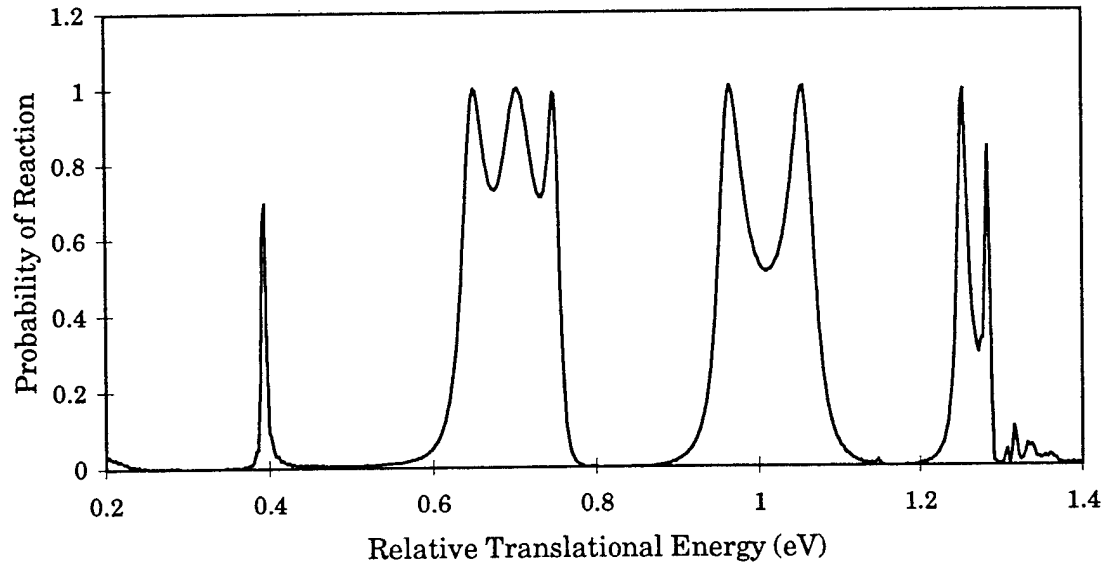

Figure D.12 Probability of reaction for the two coupled Morse oscillator LHL mass configuration for the reaction $A + BC(v = 0) \rightarrow AB(v' = 0) + C$ where the disassociation energy is 0.22 au.

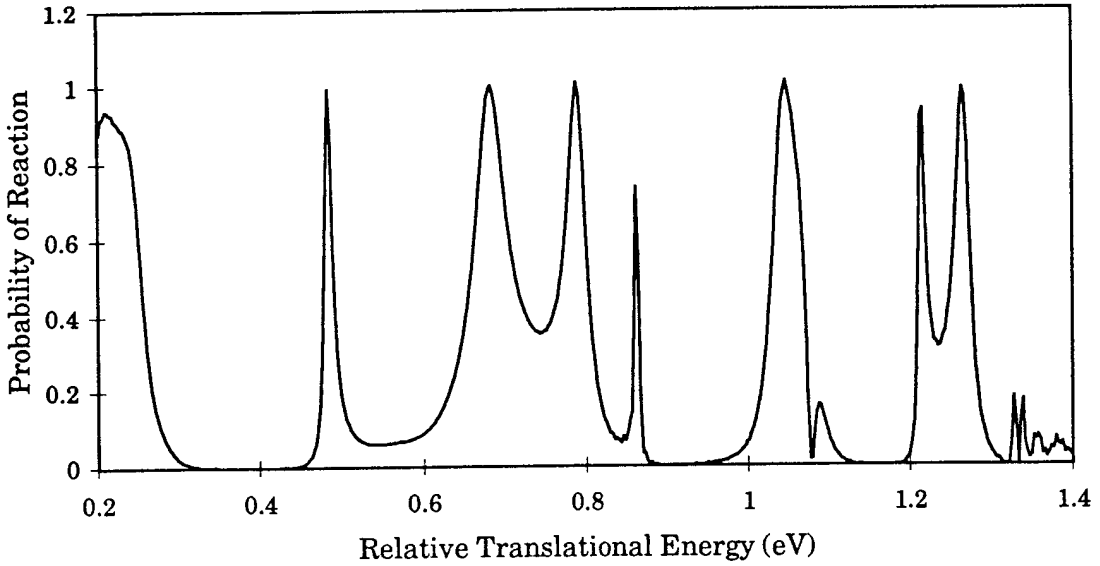

Figure D.13 Probability of reaction for the two coupled Morse oscillator LHL mass configuration for the reaction $A + BC(v = 0) \rightarrow AB(v' = 0) + C$ where the disassociation energy is 0.23 au.

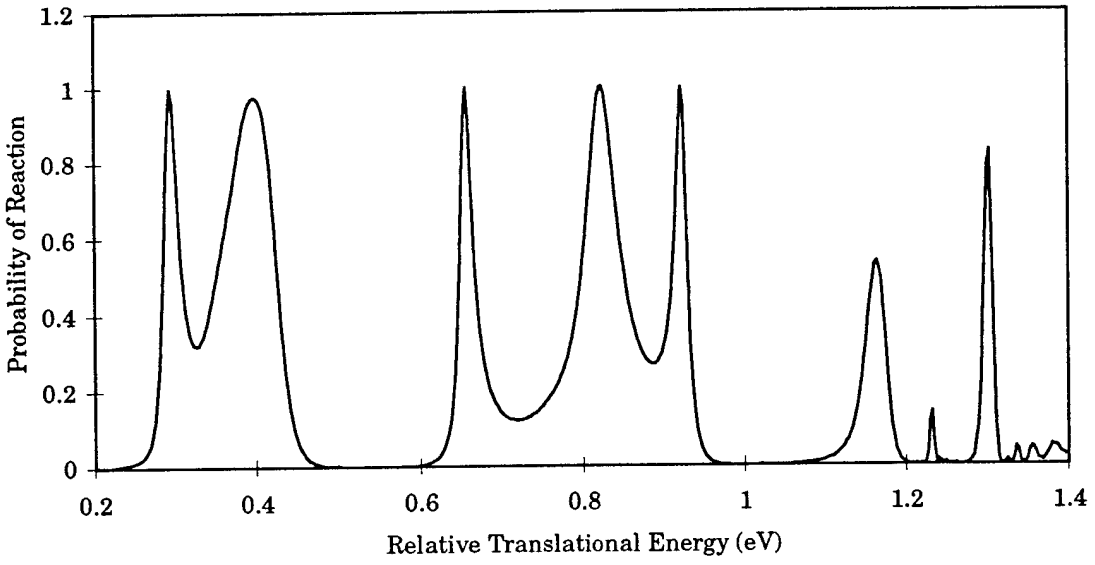

Figure D.14 Probability of reaction for the two coupled Morse oscillator LHL mass configuration for the reaction $A + BC(v = 0) \rightarrow AB(v' = 0) + C$ where the disassociation energy is 0.24 au.

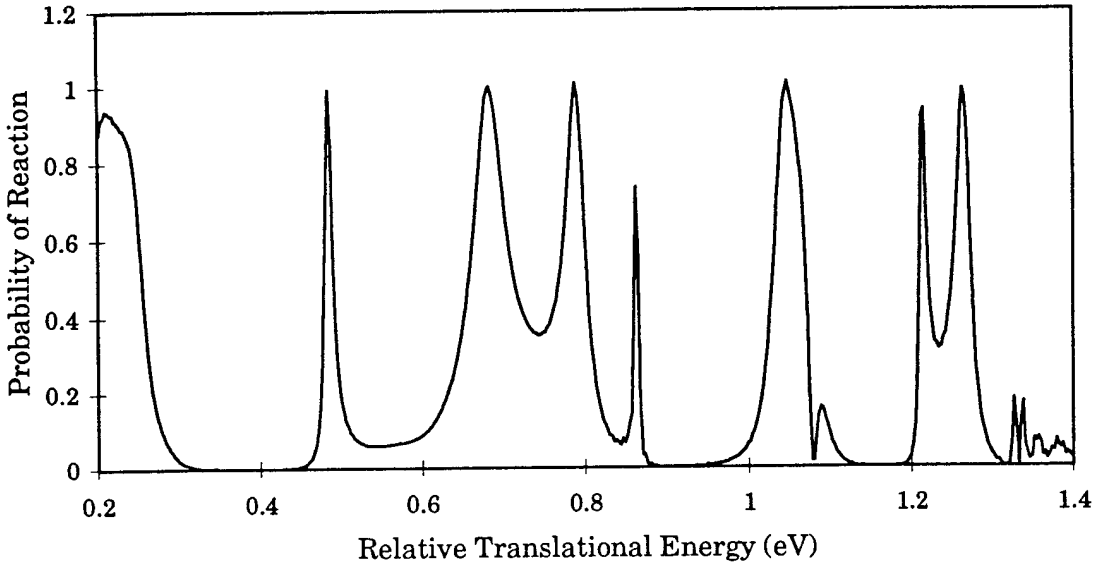

Figure D.15 Probability of reaction for the two coupled Morse oscillator LHL mass configuration for the reaction $A + BC(v = 0) \rightarrow AB(v' = 0) + C$ where the disassociation energy is 0.25 au.

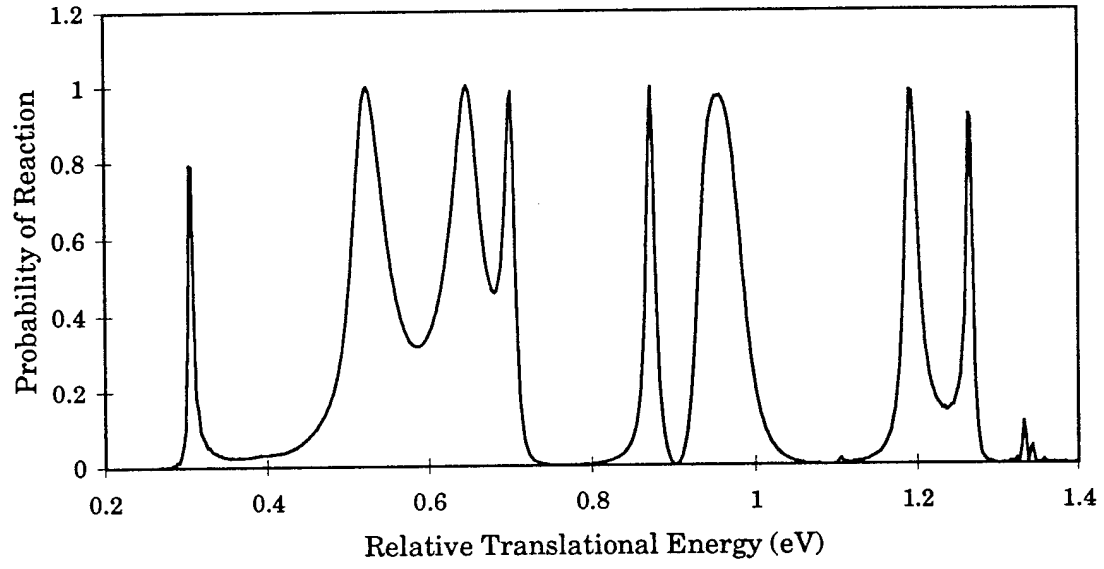

Figure D.16 Probability of reaction for the two coupled Morse oscillator LHL mass configuration for the reaction $A + BC(v = 0) \rightarrow AB(v' = 0) + C$ where the disassociation energy is 0.26 au.

The following 11 plots illustrate the probability of reaction for two coupled Morse oscillators in a light-heavy-light mass configuration where the kinetic energy coupling constant is changed from –1 (fully coupled) to 0 (uncoupled) in steps of 0.1.

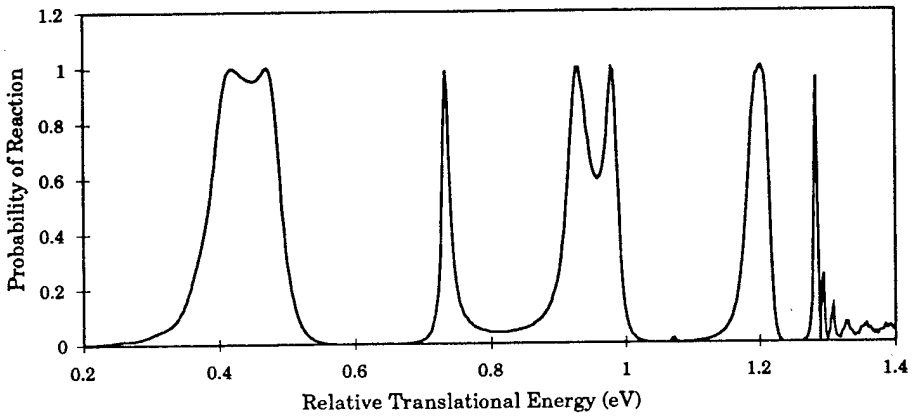

Figure D.17 Probability of reaction for the two coupled Morse oscillator LHL mass configuration for the reaction $A + BC(v = 0) \rightarrow AB(v' = 0) + C$ where the disassociation energy is 0.20 au and the kinetic energy coupling constant is –1.

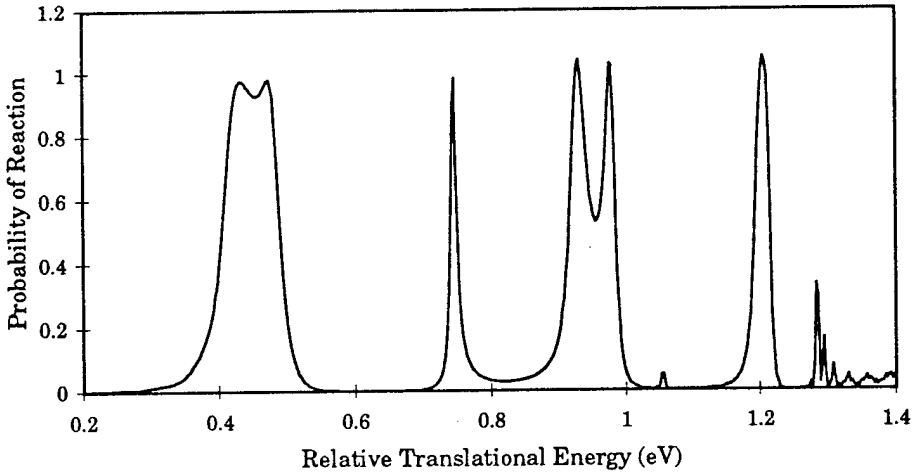

Figure D.18 Probability of reaction for the two coupled Morse oscillator LHL mass configuration for the reaction $A + BC(v = 0) \rightarrow AB(v' = 0) + C$ where the disassociation energy is 0.20 au and the kinetic energy coupling constant is –0.9.

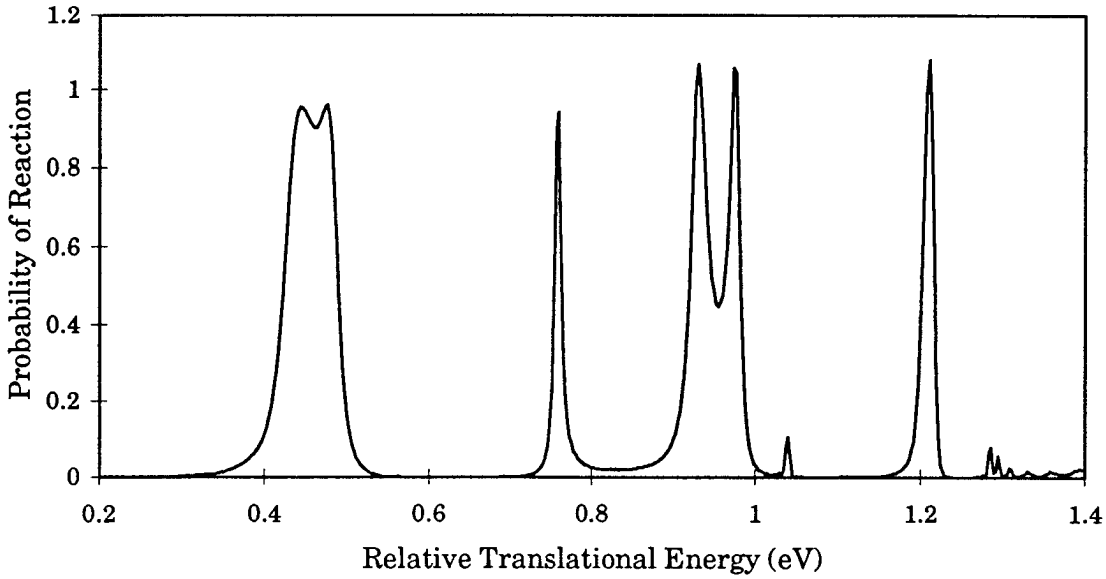

Figure D.19 Probability of reaction for the two coupled Morse oscillator LHL mass configuration for the reaction $A + BC(v = 0) \rightarrow AB(v' = 0) + C$ where the disassociation energy is 0.20 au and the kinetic energy coupling constant is –0.8.

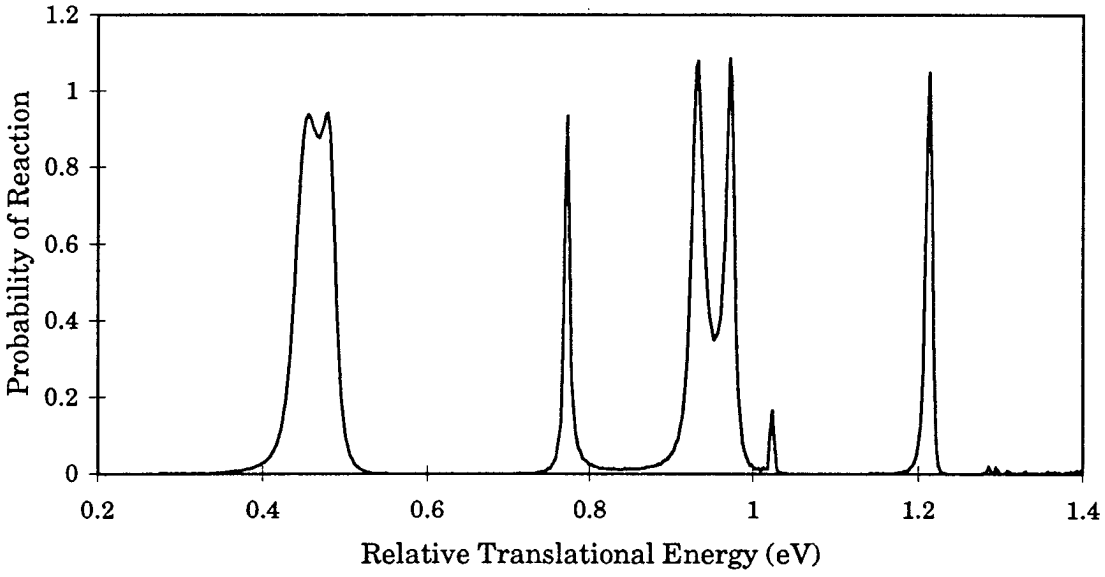

Figure D.20 Probability of reaction for the two coupled Morse oscillator LHL mass configuration for the reaction $A + BC(v = 0) \rightarrow AB(v' = 0) + C$ where the disassociation energy is 0.20 au and the kinetic energy coupling constant is –0.7

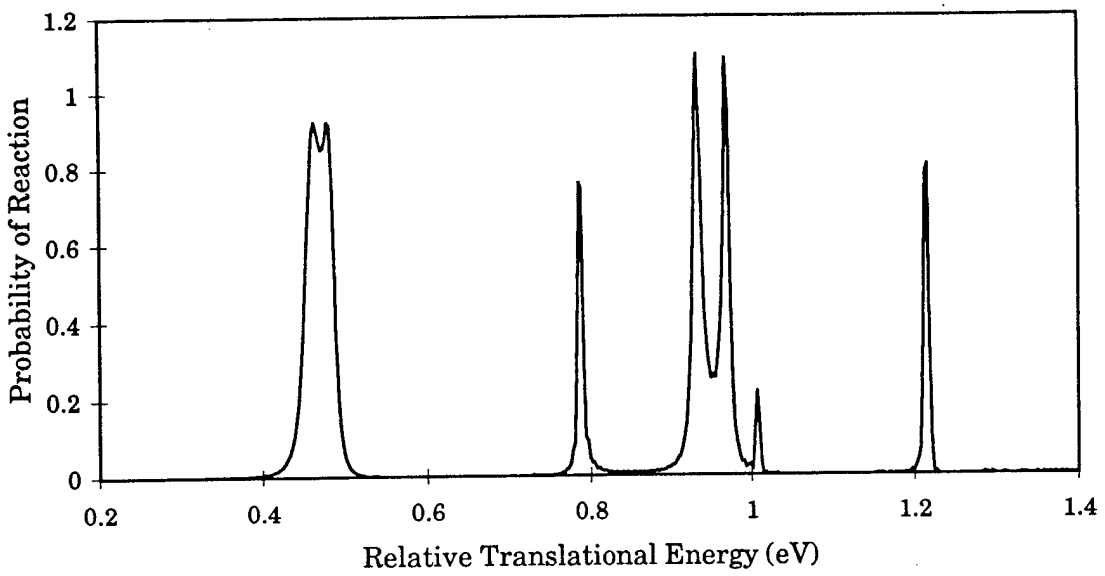

Figure D.21 Probability of reaction for the two coupled Morse oscillator LHL mass configuration for the reaction $A + BC(v = 0) \rightarrow AB(v' = 0) + C$ where the disassociation energy is 0.20 au and the kinetic energy coupling constant is –0.6.

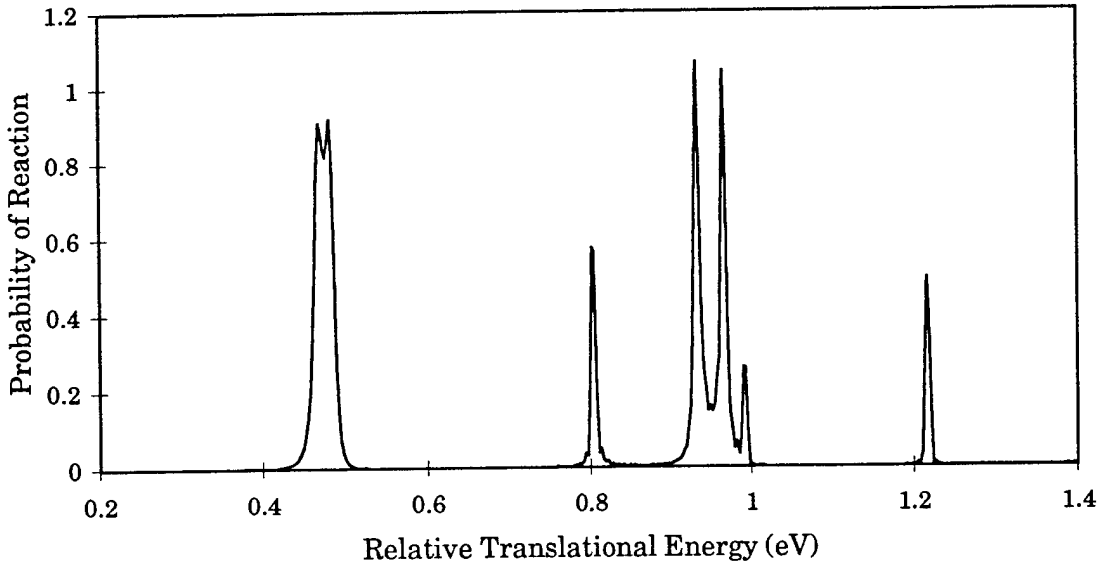

Figure D.22 Probability of reaction for the two coupled Morse oscillator LHL mass configuration for the reaction $A + BC(v = 0) \rightarrow AB(v' = 0) + C$ where the disassociation energy is 0.20 au and the kinetic energy coupling constant is –0.5.

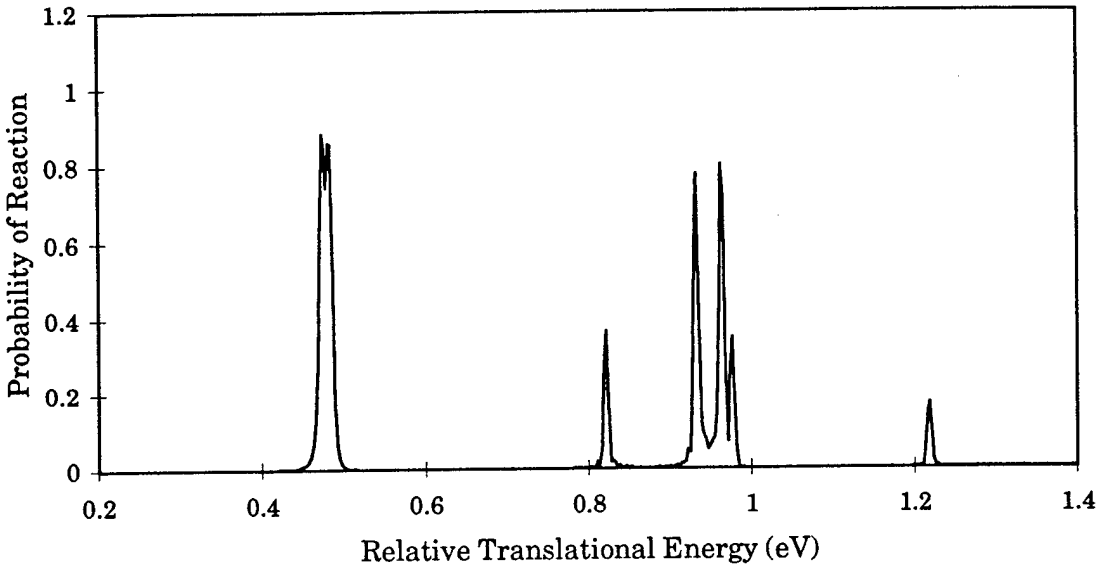

Figure D.23 Probability of reaction for the two coupled Morse oscillator LHL mass configuration for the reaction $A + BC(v = 0) \rightarrow AB(v' = 0) + C$ where the disassociation energy is 0.20 au and the kinetic energy coupling constant is –0.4.

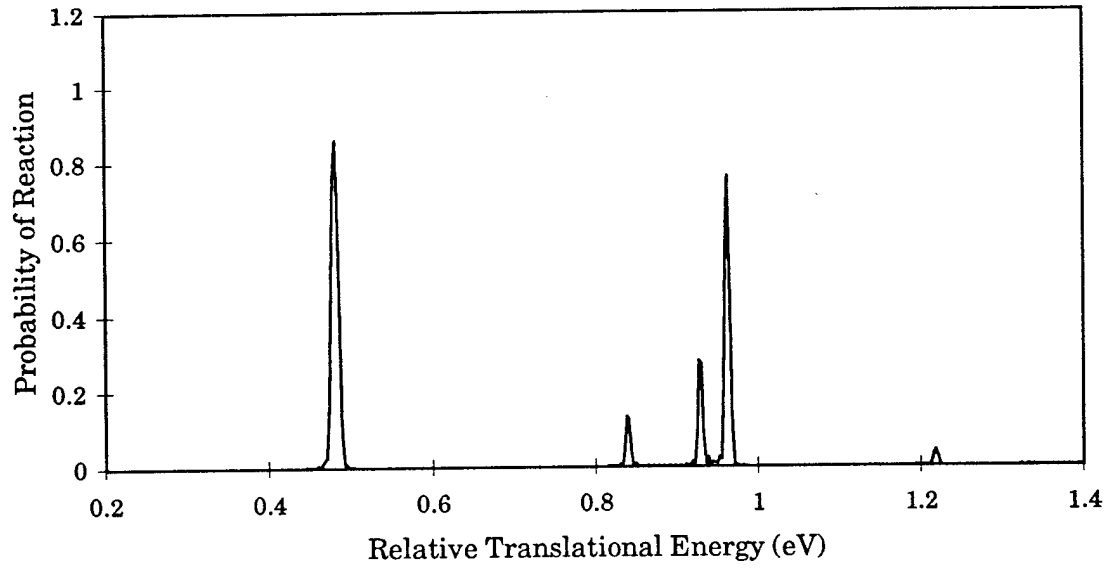

Figure D.24 Probability of reaction for the two coupled Morse oscillator LHL mass configuration for the reaction $A + BC(v = 0) \rightarrow AB(v' = 0) + C$ where the disassociation energy is 0.20 au and the kinetic energy coupling constant is –0.3.

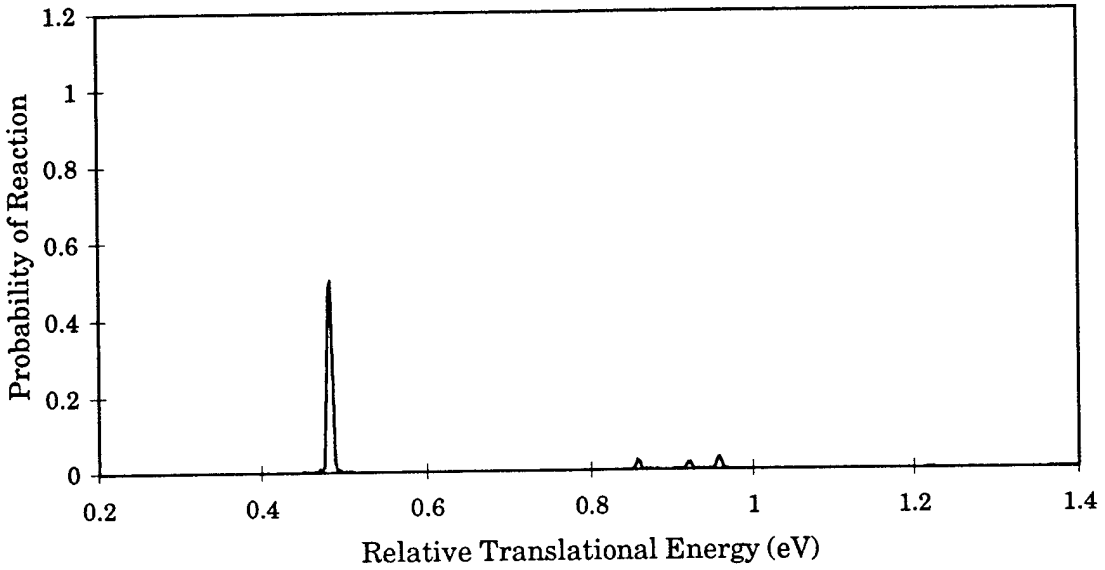

Figure D.25 Probability of reaction for the two coupled Morse oscillator LHL mass configuration for the reaction $A + BC(v = 0) \rightarrow AB(v' = 0) + C$ where the disassociation energy is 0.20 au and the kinetic energy coupling constant is –0.2.

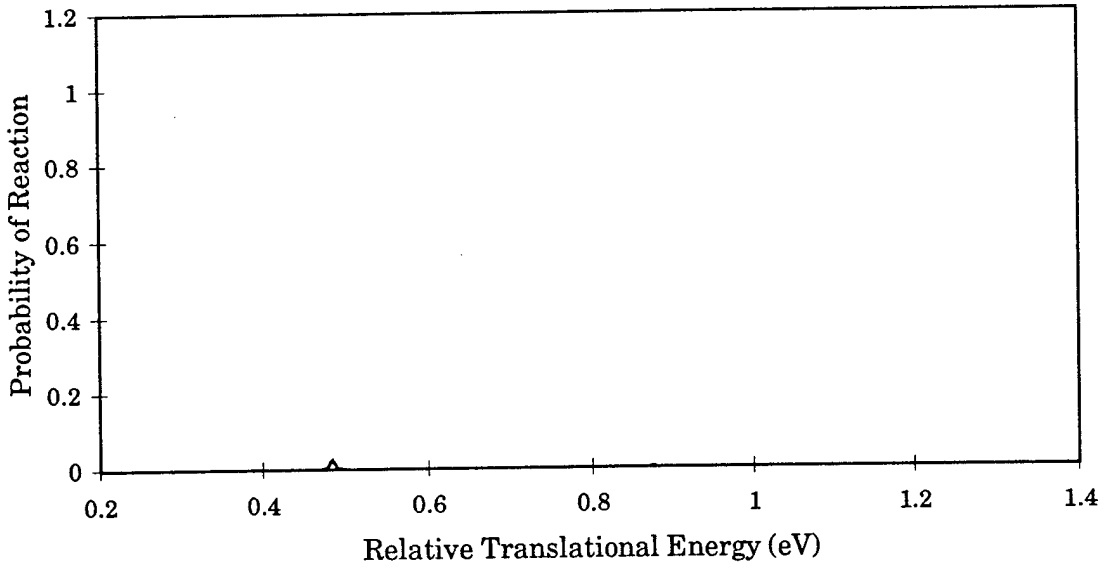

Figure D.26 Probability of reaction for the two coupled Morse oscillator LHL mass configuration for the reaction $A + BC(v = 0) \rightarrow AB(v' = 0) + C$ where the disassociation energy is 0.20 au and the kinetic energy coupling constant is –0.1.

Bibliography

1. J. A. Boatz, M. E. Fuhardo, and J. A. Sheehy. Monte carlo simulations of the structures and optical absorption spectra of $NaAr$ clusters and solids: An application of spectral theory of chemical binding. High Energy Density Matter Contractor's Review, Air Force Office of Scientific Research, 1996.
2. E. J. Wucherer and J. A. Boatz. Quantum mechanical study of the energetics of C_8H_8 hydrocarbons. High Energy Density Matter Contractor's Review, Air Force Office of Scientific Research, 1996.
3. G. P. Perram. *International J. of Chem. Kinetics*, 27:817, 1995.
4. T. L. Henshaw, S. D. Herrera, G. W. Haggquist, and L. A. Schlie. Photodissociation kinetics of ClN_3 – implications for an $NCl\left(a^1\Delta\right) - I^*\left(^2P_{1/2}\right)$ chemical laser. Molecular Dynamics Contractor's Review, Air Force Office of Scientific Research, 1996.
5. H. Miller, J. Choy, and G. Hager. Pulse injection of a photolytic iodine laser. Molecular Dynamics Contractor's Review, Air Force Office of Scientific Research, 1996.
6. J. W. Nicholson, W. Rudolph, and G. Hager. Collision dynamics and ultrafast modulation in photolytic iodine lasers. Molecular Dynamics Contractor's Review, Air Force Office of Scientific Research, 1996.
7. United States Government Accouting Office. Theater missle defense: Significant technical challenges face the airborne laser program. GAO/NSAID-98-37, 1997.
8. J. W. Duff, R. D. Sharma, A. Dalgarno, and J. L. Fox. Quasiclassical trajectory study of the $N\left(^4S\right) + NO\left(X^2\Pi\right) \rightarrow N_2\left(X^1\Sigma_g^+\right) + O\left(^3P\right)$ reaction rate constant: Implications for thermospheric NO formation. Molecular Dynamics Contractor's Review, Air Force Office of Scientific Research, 1996.
9. J. A. Dodd, S. M. Singleton, S. M. Miller, P. S. Armstrong, and W. A. M. Blumberg. Vibrational relaxation of $NO\left(\nu = 2, 3\right)$ by atomic oxygen. Molecular Dynamics Contractor's Review, Air Force Office of Scientific Research, 1996.
10. M. J. Bastian, R. A. Dressler, D. J. Levandier, and E. Murad. Guided-ion beam studies of collision and photo-induced dissassociation of the $[N_2O{\cdot}H_2O]^+$ cluster. Molecular Dynamics Contractor's Review, Air Force Office of Scientific Research, 1996.
11. F. London. *Z. Elektrochem.*, 35:552, 1929.
12. H. Eyring and M. Polanyi. *Z. Physik. Chemie B*, 12:279, 1931.
13. S. Sato. *J. Chem. Phys.*, 23:2465, 1955.
14. F. J. Aoiz, L. Bañares, M. J. D'Mello, V. J. Herrero, V. Sáez Rábanos, L. Schneider, and R. E. Wyatt. *J. Chem. Phys.*, 101:5781, 1994.

15. R. Kosloff and D. Kosloff. *J. Chem. Phys.*, 79:1823, 1983.

16. K. Yamashita and W. H. Miller. *J. Chem. Phys.*, 82:5475, 1985.

17. D. Neuhauser, R. S. Judson, D. J. Kouri, D. E. Adelman, N.E. Shafer, D. A. V. Kliner, and R. N. Zare. *Science*, 257:519, 82.

18. D. J. Diestler. *J. Chem. Phys.*, 50:4746, 1969.

19. D. J. Diestler. *J. Chem. Phys.*, 54:4547, 1971.

20. B. Gazdy and J. M. Bowman. In J. M. Bowman and M. A. Ratner, editors, *Advances in Molecular Vibrations and Collision Dynamics*, volume 1B, pages 105–137. JAI Press Greenwich, 1991.

21. J. Z. H. Zhang and W. H. Miller. *Chem. Phys. Letters*, 153:465, 1988.

22. J. Z. H. Zhang and W. H. Miller. *J. Chem. Phys.*, 91:1528, 1989.

23. D. E. Manolopoulos and R. E. Wyatt. *Chem. Phys. Letters*, 159:123, 1989.

24. J. M. Launay and M. L. Dourneuf. *Chem. Phys. Letters*, 163:178, 1989.

25. D. E. Weeks and D. J. Tannor. *Chem. Phys. Letters*, 224:451, 1994.

26. N. C. Blais, M. Zhao, D. G. Truhlar, D. W. Schwenke, and D. J. Kouri. *Chem. Phys. Letters*, 169:11, 1990.

27. J. V. Michael, J. R. Fisher, J. M. Bowman, and Q. Sun. *Science*, 249:269, 1990.

28. M. D'Mello, D. E. Manolopoulos, and R. E. Wyatt. *J. Chem. Phys.*, 94:5985, 1991.

29. S. L. Mielke, R. S. Friedman, D. G. Truhlar, and D. W. Schwenke. *Chem. Phys. Letters*, 188:359, 1992.

30. M. Zhao, D. G. Truhlar, D. W. Schwenke, and D. J. Kouri. *J. Chem. Phys.*, 94:7074, 1990.

31. R. B. Walker, E. B. Stechel, and J. C. Light. *J. Chem. Phys.*, 69:2922, 1978.

32. J. Manz and J. Römelt. *Chem. Phys. Letters*, 76:337, 1980.

33. J. Römelt. *Chem. Phys. Letters*, 74:263, 1980.

34. A. Kuppermann, J. A. Kaye, and J. P. Dwyer. *Chem. Phys. Letters*, 74:257, 1980.

35. D. K. Bondi, D. C. Clary, N. L. Connor, B. C. Garrett, and D. G. Truhlar. *J. Chem. Phys.*, 76:4986, 1982.

36. J. Dai and J. Z. H. Zhang. *J. Phys. Chem.*, 100:6898, 1996.

37. D. J. Tannor and D. E. Weeks. *J. Chem. Phys.*, 98:3884, 1993.

38. D. E. Weeks and D. J. Tannor. *Chem. Phys. Letters*, 207:301, 1993.

39. D. Neuhauser and M. Baer. *J. Chem. Phys.*, 90:4351, 1989.

40. D. Neuhauser, M. Baer, R. S. Judson, and D. J. Kouri. *Computer Phys. Comm.*, 63:460, 1991.

41. R. S. Calfas and D. E. Weeks. *Chem. Phys. Letters*, accepted for publication.

42. M. Baer. In I. Prigogine and S. A. Rice, editors, *Advances in Chemical Physics*, volume XLIX, pages 191–309. John Wiley & Sons, New York, 1982.

43. R. Kosloff and C. Cerjan. *J. Chem. Phys.*, 81:3722, 1984.

44. D. J. Tannor, A. Besprozvannaya, and C. J. Williams. *J. Chem. Phys.*, 96:2998, 1992.

45. J. Z. H. Zhang. *Chem. Phys. Letters*, 160:417, 1989.

46. A. Jäckle and H. D. Meyer. *J. Chem. Phys.*, 102:5650, 1995.

47. K. F. Lim and J. I. Brauman. *J. Chem. Phys.*, 94:7164, 1991.

48. U. V. Riss and H. D. Meyer. *J. Chem. Phys.*, 105:1409, 1996.

49. T. Seideman and W. H. Miller. *J. Chem. Phys.*, 96:4412, 1992.

50. T. Seideman and W. H. Miller. *J. Chem. Phys.*, 97:2499, 1992.

51. U. Peskin, W. H. Miller, and A. Edlund. *J. Chem. Phys.*, 103:10030, 1995.

52. J. R. Taylor. *Scattering Theory: The Quantum Theory of Nonrelativistic Collisions.* Krieger, New York, 1987.

53. E. Merzbacher. *Quantum Mechanics.* Wiley, New York, 1970.

54. W. Magnus, A. Karrass, and D. Solitar. *Combinatorial Group Theory: Presentations fo Groups in Terms of Generators and Relations.* Wiley, New York, 1966.

55. C. Leforestier, R. H. Bisseling, C. Cerjan, M. D. Feit, R. Friesner, A. Guldberg, A. Hammerisch, G. Jolicard, W. Karrlein, H. D. Meyer, N. Lipkin, O Roncero, and R. Kosloff. *J. Comput. Phys.*, 94:59, 1991.

56. E. E. Anderson. *Modern Physics and Quantum Mechanics.* W. B. Saunders Co., Philadelphia, 1971.

57. C. Cohen-Tannoudji, B. Diu, and F. Laloë. *Quantum Mechanics.* Wiley, New York, 1977.

58. R. Kosloff. *J. Phys. Chem.*, 92:2087, 1988.

59. P. Siegbahn and B. Liu. *J. Chem. Phys.*, 68:2457, 1978.

60. D. G. Truhlar and C. J. Horowitz. *J. Chem. Phys.*, 68:2466, 1978.

61. R. J. Hinde and G. S. Ezra. *Chem. Phys. Letters*, 228:333, 1994.

62. W. G. Harter. *Principles of Symmetry, Dynamics, and Spectroscopy.* Wiley-Interscience, New York, 1993.

Vita

Captain Roy Calfas began his service in the United States Air Force in 1988 at the Air Force Officer Training School, Medina Annex, Lackland AFB, TX. He received his commission on 17 March 1989 after which he served various positions within the 81st Tactical Fighter Wing, Royal Air Force Bentwaters, United Kingdom of Great Britain and Northern Ireland from July 1989 to April 1992. During that time, he served as part of the 4401st Composite Wing (Provisional), King Abdul Aziz Air Base, Dahran, Saudi Arabia from June 1991 to September 1991. He entered the Master's degree program at the Air Force Institute of Technology in May 1992 and graduated in December 1993. He then extended into the Doctoral program.

Permanent address: [redacted]

REPORT DOCUMENTATION PAGE	Form Approved OMB No. 0704-0188

1. AGENCY USE ONLY *(Leave blank)*	2. REPORT DATE	3. REPORT TYPE AND DATES COVERED
	4 Nov 97	Doctoral Dissertation

4. TITLE AND SUBTITLE
Quantum Reactive Scattering in Two Dimensions

5. FUNDING NUMBERS

6. AUTHOR(S)
ROY S. CALFAS, CAPTAIN, USAF

7. PERFORMING ORGANIZATION NAME(S) AND ADDRESS(ES)
Air Force Institute of Technology
Department of Engineering Physics
2750 P Street
Wright-Patterson AFB, OH 45433-6583

8. PERFORMING ORGANIZATION REPORT NUMBER
AFIT/DSP/ENP/97-02

9. SPONSORING/MONITORING AGENCY NAME(S) AND ADDRESS(ES)
Dr. Jerry Boatz
AFRL/PRSP
10 E. Saturn BLVD.
Edwards AFB, CA 93524-7680

10. SPONSORING/MONITORING AGENCY REPORT NUMBER

11. SUPPLEMENTARY NOTES

12a. DISTRIBUTION AVAILABILITY STATEMENT
APPROVED FOR PUBLIC RELEASE; DISTRIBUTION UNLIMITED

12b. DISTRIBUTION CODE

13. ABSTRACT *(Maximum 200 words)*

In an effort to develop a more efficient time dependent approach for calculating scattering matrix elements, absorbing boundary conditions are combined together with the channel packet method. As an introduction to scattering, scattering matrix elements are presented for a one--dimensional square well and a one--dimensional potential consisting of a Gaussian well with symmetric Gaussian barriers. Next, the combination of the channel packet method together with absorbing boundary conditions yields an order of magnitude savings in the time necessary to compute the correlation function for the collinear H+H\sub{2} reaction. The computed scattering matrix elements are in good agreement with previous calculations. A model system consisting of two coupled collinear Morse oscillators is used to investigate the effects of kinetic energy coupling and potential well depth on scattering matrix elements. For light-light-light, medium-light-medium and heavy-light-heavy mass configurations, absorbing boundary condition reflection introduces significant error into the scattering matrix elements. As an initial analysis of absorbing boundary condition reflection error, scattering matrix elements are presented for reflection from absorbing boundary conditions using a simplified Morse oscillator potential. Scattering matrix elements for the light-heavy-light mass configuration do not suffer from significant absorbing boundary condition reflection error. For this mass configuration, the effects of kinetic energy coupling and well depth on scattering matrix elements are presented for a variety of two collinear coupled Morse oscillator potentials.

14. SUBJECT TERMS	15. NUMBER OF PAGES
CHEMISTRY, SCATTERING, NUMERICAL METHODS, QUANTUM PHYSICS	179
	16. PRICE CODE

17. SECURITY CLASSIFICATION OF REPORT	18. SECURITY CLASSIFICATION OF THIS PAGE	19. SECURITY CLASSIFICATION OF ABSTRACT	20. LIMITATION OF ABSTRACT
UNCLASSIFIED	UNCLASSIFIED	UNCLASSIFIED	UL